ABSTRACT

Title of Document: PYROLYSIS OF REINFORCED POLYMER
COMPOSITES: PARAMETERIZING A
MODEL FOR MULTIPLE COMPOSITIONS

Geraldine E. Martin, Master of Science, 2015

Directed By: Professor Stanislav Stoliarov
Department of Fire Protection Engineering

A single set of material properties was developed to describe the pyrolysis of fiberglass reinforced polyester composites at multiple composition ratios. Milligram-scale testing was performed on the unsaturated polyester (UP) resin using thermogravimetric analysis (TGA) coupled with differential scanning calorimetry (DSC) to establish and characterize an effective semi-global reaction mechanism, of three consecutive first-order reactions. Radiation-driven gasification experiments were conducted on UP resin and the fiberglass composites at compositions ranging from 41 to 54 wt% resin at external heat fluxes from 30 to 70 kW m^{-2}. The back surface temperature was recorded with an infrared camera and used as the target for inverse analysis to determine the thermal conductivity of the systematically isolated constituent species. Manual iterations were performed in a comprehensive pyrolysis model, ThermaKin. The complete set of properties was validated for the ability to reproduce the mass loss rate during gasification testing.

PYROLYSIS OF REINFORCED POLYMER COMPOSITES: PARAMETERIZING A MODEL FOR MULTIPLE COMPOSITIONS

By

Geraldine E. Martin

Thesis submitted to the Faculty of the Graduate School of the
University of Maryland, College Park, in partial fulfillment
of the requirements for the degree of
Master of Science
2015

Advisory Committee:
Assistant Professor Stanislav Stoliarov, Chair
Associate Professor Andre Marshall
Adjunct Professor Richard Roby

Acknowledgements

I would like to thank those whose efforts contributed to the completion of this work. This project was made possible through the support and instruction from my colleagues at the University of Maryland, most notably Mark McKinnon, my advisor Dr. Stoliarov, and my supervisors at Combustion Science & Engineering. Each has my utmost respect and appreciation for their individual influence throughout this process.

Table of Contents

Acknowledgements ii
Table of Contents iii
List of Tables iv
List of Figures v
1. Introduction 1
  1.1 Background 3
    1.1.1 Fabrication of Composites 7
    1.1.2 Existing Models 9
  1.2 Objectives 21
2. Methods and Materials 24
  2.1 Sample Material 24
  2.2 Milligram Scale Experiments 29
  2.3 Bench-Scale Experiments 32
    2.3.1 Radiation Absorption 32
    2.3.2 Gasification Experiments 34
  2.4 ThermaKin 39
    2.4.1 Milligram-Scale Modeling 44
    2.4.2 Modeling Gasification Experiments 46
3. Results and Discussion 49
  3.1 Milligram Scale 49
    3.1.1 Thermogravimetric Analysis 49
      3.1.1.1 Experimental Results 49
      3.1.1.2 Global Reaction Mechanism 52
    3.1.2 Differential Scanning Calorimetry 57
      3.1.2.1 Glass Transition Temperature 57
      3.1.2.2 Polyester Resin Experimental Data 58
      3.1.2.3 Specific Heat Capacity 60
      3.1.2.4 Heats of Degradation 66
  3.2 Radiative Properties 69
    3.2.1 Absorption Coefficient 70
    3.2.2 Emissivity 71
  3.3 Gasification Experiments 72
    3.3.1 Back Surface Temperature 73
    3.3.2 Density 80
    3.3.3 Thermal Conductivity 84
    3.3.4 Mass Loss Rate 93
    3.3.5 Validation 97
4. Conclusion 103
Appendix I: Gasification experiments with and without aluminum foil backing 106
Appendix II: Milligram-scale experiments with char samples 108
Works Cited 111

List of Tables

Table 1. Material properties characterized by Lattimer et al. [15]. 15
Table 2. Material properties characterized by Zhou and Yu for fiberglass reinforced polyester composite [16]. 18
Table 3. Composition ration calculated based on average sample measurements for each individual configuration (wt% resin). 48
Table 4. Average thickness based on measurements for each configuration (mm).... 48
Table 5. Effective reaction mechanism for degradation of polyester resin. 54
Table 6. Effective degradation reaction mechanism with piece-wise subroutine....... 61
Table 7. Specific heat capacity of constituent species. 65
Table 8. Heat of decompositions for each reaction in the mechanism. 68
Table 9. Absorption coefficients of evolved species. 71
Table 10. Emissivity of evolved species. 72
Table 11. Density of constituent species for composite samples. 83
Table 12. Density of the pure UP resin and decomposition species. 84
Table 13. Thermal conductivity of UP resin and decomposition species. 85
Table 14. Complete set of material properties. 98

List of Figures

Figure 1. Phthalic Anhydride $C_8H_4O_3$ 4
Figure 2. Maleic Anhydride $C_2H_2(CO)_2O$, unsaturated acid 4
Figure 3. Propylene glycol $C_3H_8O_2$, glycol 4
Figure 4. Styrene C_3H_8, unsaturated monomer 4
Figure 5. Repeating unit for the crosslinking in the cured resin system. 5
Figure 6. 10 oz fiberglass fabric [19]. 24
Figure 7. UP resin sample, the glossy surface (left) was exposed during fabrication and the matte surface (right) was against the mold. 25
Figure 8. Fiberglass sample fabricated using a hand lay-up method with woven fabric and unsaturated polyester resin (top/side/bottom). 26
Figure 9. Nezsch F3 Jupiter. 29
Figure 10. Experimental configuration for absorption coefficient measurement [8]. 32
Figure 11. Schematic of the experimental apparatus used during radiation-driven gasification experiments. The truncated cone heater, CAPA, and infrared camera are shown. 34
Figure 12. A closer cross-sectional (left) and top (right) view of the CAPA, used to purge the sample surface with nitrogen during radiation-driven gasification experiments. 35
Figure 13. Sample holder with aluminum mesh and Kaowool. 36
Figure 14. Sample secured in the holder to prevent deformation away from the wire mesh backing. 37
Figure 15. Areas defined for evaluation of the surface temperature and spatial variations across the sample [8]. 38
Figure 16. True heating rate measured from TGA/DSC testing. 44
Figure 17. Agreement between the true heating rate and the fit for modeling the variable heating rate. 45
Figure 18. Average normalized mass of the resin measured from TGA. 50
Figure 19. Average normalized mass loss rate calculated from TGA. 50
Figure 20. Agreement between the normalized mass from the simulation and the experimental results. 55
Figure 21. Normalized mass loss rate from simulation showing contribution of individual reactions with data. 56
Figure 22. DSC measurement of heat flow rate to the resin sample to determine the oven post-cure temperature. 57
Figure 23. DSC measurement of the heat flow rate as a function of time for the oven-cured polyester resin. 58
Figure 24. Temperature dependent heat of gasification calculated from the heat flow rate measurement. 59
Figure 25. Apparent specific heat capacity calculated from DSC measurements. 60

Figure 26. Second order polynomial fit for the initial rise in heat capacity of the virgin UP resin. 62
Figure 27. Apparent specific heat capacity of the char as a function of temperature. 63
Figure 28. Specific heat capacity of individual species over the temperature range each is present. 65
Figure 29. Baseline for the energy required to heat the sample through the specified heat profile as a function of temperature. 66
Figure 30. Energy evaluated for the heats of decomposition for the kinetic model. 67
Figure 31. Agreement between the heat flow rate from the model simulation and experimental data. 68
Figure 32. Total heat flow to the sample as a function of sample temperature for the model simulation and experimental data. 69
Figure 33. Thermal images from IR camera testing of fiberglass 41 wt% resin at 30kW m^{-2}. 73
Figure 34. Thermal images from IR camera testing of fiberglass 48 wt% resin at 70 kW m^{-2}. The gaseous species are highlighted in the frame at 589 seconds. 74
Figure 35. Back surface temperature measurements for UP resin samples during gasification experiments at external heat fluxes of – (a) 30 kW m^{-2}; (b) 50 kW m^{-2}. The top surface of the samples at 30 kW m^{-2} were coated with a layer of the emissive paint that was applied to the back surface of all of the samples. 76
Figure 36. Back surface temperature measurements for fiberglass samples, 41 wt% resin, tested at an external heat flux of – (a) 30 kW m^{-2}; (b) 50 kW m^{-2}; (c) 70 kW m^{-2}. 78
Figure 37. Back surface temperature measurements of fiberglass samples, 48 wt% resin, tested at an external heat flux of – (a) 30 kW m^{-2}; (b) 50 kW m^{-2}; (c) 70 kW m^{-2}. 79
Figure 38. Back surface temperature measurements of fiberglass samples, 54 wt% resin, tested at an external heat flux of – (a) 30 kW m^{-2}; (b) 50 kW m^{-2}; (c) 70 kW m^{-2}. 80
Figure 39. Agreement between UP resin back surface temperature profiles from experimental measurement and model prediction. 86
Figure 40. Agreement of bottom surface temperature profiles for UP resin from experimental measurements and model predictions at 50 kW m^{-2}. 86
Figure 41. Agreement of temperature profiles for the fiberglass composite, nominally 48 wt% resin, from experimental measurements and the model prediction. 88
Figure 42. Back surface temperature profiles from experimental data and model predictions for fiberglass samples composed of 41 wt% resin and tested at an external heat flux of – (a) 30 kW m^{-2}; (b) 50 kW m^{-2}; (c) 70 kW m^{-2}. 89
Figure 43. Back surface temperature profiles from experimental data and model predictions for fiberglass samples composed of 48 wt% resin and tested at an external heat flux of – (a) 30 kW m^{-2}; (b) 50 kW m^{-2}; (c) 70 kW m^{-2}. 90

Figure 44. Back surface temperature profiles from experimental data and model predictions for fiberglass samples composed of 54 wt% resin and tested at an external heat flux of – (a) 30 kW m^{-2}; (b) 50 kW m^{-2}; (c) 70 kW m^{-2}. 91
Figure 45. Thermal conductivity of individual species over the temperature range the species was present. 92
Figure 46. Mass loss rate from gasification experiments for UP resin, with a foil backing, at external heat fluxes of – (a) 30 kW m^{-2}; and (b) 50 kW m^{-2}. 93
Figure 47. Mass loss rate measured during gasification experiments for fiberglass samples composed of 41 wt% resin and tested at an external heat flux of – (a) 30 kW m^{-2}; (b) 50 kW m^{-2}; (c) 70 kW m^{-2}. 94
Figure 48. Mass loss rate measured during gasification experiments for fiberglass samples composed of 48 wt% resin and tested at an external heat flux of – (a) 30 kW m^{-2}; (b) 50 kW m^{-2}; (c) 70 kW m^{-2}. 95
Figure 49. Mass loss rate measured during gasification experiments for fiberglass samples composed of 54 wt% resin and tested at an external heat flux of – (a) 30 kW m^{-2}; (b) 50 kW m^{-2}; (c) 70 kW m^{-2}. 96
Figure 50. Mass loss rate profiles from experimental data and model simulations for UP resin at an external heat fluxes of – (a) 30; and (b) 50 kW m^{-2}. 99
Figure 51. Mass loss rate from experimental data and model simulations for 41 wt% composite samples tested at an external heat flux of – (a) 30 kW m^{-2}; (b) 50 kW m^{-2}; (c) 70 kW m^{-2}. 100
Figure 52. Mass loss rate from experimental data and model simulations for 48 wt% composite samples tested at an external heat flux of – (a) 30 kW m^{-2}; (b) 50 kW m^{-2}; (c) 70 kW m^{-2}. 101
Figure 53. Mass loss rate from experimental data and model simulations for 54 wt% composite samples tested at an external heat flux of – (a) 30 kW m^{-2}; (b) 50 kW m^{-2}; (c) 70 kW m^{-2}. 102
Figure 54. Back surface temperature and mass loss rate for 41 wt% resin fiberglass samples tested at 30 kW m^{-2} with and without an aluminum foil backing. 107
Figure 55. Back surface temperature and mass loss rate for 41 wt% resin fiberglass sample tested at 50 kW m^{-2} with and without an aluminum foil backing................ 107
Figure 56. Back surface temperature and mass loss rate for 48 wt% resin fiberglass samples tested at 30 kW m^{-2} with and without an aluminum foil backing. 107
Figure 57. Normalized mass loss during TGA/DSC testing of the char................... 108
Figure 58. DSC measurement of heat flow to the char. 109
Figure 59. Apparent specific heat capacity of the char as a function of temperature. 110

1. Introduction

One of the remaining questions in the field of fire science centers on pyrolysis in the condensed phase. This complex process is essential to the description of material flammability and how fire models simulate fire growth and flame spread. Many investigators have contributed to advancements in the area, but there are a significant number of issues that remain to be addressed. Recent work has focused on developing models with the ability to predict the rate of production of gaseous fuel species from the condensed phase, such as ThermaKin [1], Gpyro [2], Pyropolis [3], and the condensed phase sub model in Fire Dynamics Simulator (FDS) [4]. These pyrolysis models describe fundamental chemical, heat, and mass transfer processes using simplified, semi-empirical formulae, which require a set of well-defined material properties.

This sophisticated approach requires the development of experimental procedures and analysis methods to characterize the material properties within the model. Many of the current methods rely on inverse analyses to optimize a set of properties to reproduce the selected target data. However, it has been shown [5] that some material properties may have a compensating effect that can result in significant variations in the characterized properties. In order to describe material behavior for a range of fire conditions, it is desirable to parameterize a robust model, evaluated for the predicative capability for a variety of thermal exposures that are representative of fire conditions.

Our group at the University of Maryland has worked to develop a set of experimental procedures and analyses that rely on milligram-scale and bench-scale testing to determine a set of material properties to predict the time history of production of gaseous volatiles from the condensed phase [6]. The properties determined through this method are validated against independent experimental data. Previous studies have demonstrated the successful application to cellulosic, non-charring polymeric, as well as charring polymeric materials [7] [8] [9].

The previous parameterization work on reinforced polymer composites was performed on pure materials or composites of a single composition with no real attempt to predict changes in the burning behavior with change in the composition. The intent of this work is to demonstrate that it is possible and to present a methodology to develop such models. The application will describe the behavior of a polymer reinforced composite, specifically fiberglass reinforced unsaturated polyester (UP) resin, using one set of material properties and extrapolating to various composition ratios and thermal exposures.

The characterized material properties include density, stoichiometric coefficients, Arrhenius rate reaction parameters (i.e., pre-exponential factor and activation energy), heats of decomposition, specific heat capacity, thermal conductivity, emissivity, and absorption coefficient.

1.1 Background

Reinforced polymer composites have become commonplace in the built environment over the last 60 years [10]. Typical applications include structural members within infrastructure, maritime, and aircrafts. These composites are fabricated through the polymerization of a liquid resin in the presence of a chemical initiator within an interpenetrating fiber network. There are a number of options available for the resin system and the reinforcement, and these options allow the user to select the combination that will produce a composite with favorable properties for a specific application. The commonly used resins include polyester, epoxy, and vinyl ester. Methyl ethyl ketone peroxide (MEKP) is a widely used standard initiator. Typical fiber reinforcement materials are fiberglass, carbon fiber, and KEVLAR.

A representative composite, unsaturated polyester resin reinforced with woven E-glass fibers, was identified as the most common combination [10] and selected as the focus for this study. The chemical processes of interest to this investigation were polymerization of the unsaturated polyester resin and thermal degradation of the individual resin and the composite as a whole. An understanding of the chemical processes occurring during the formation of the material provides for a greater understanding of the processes that occur during thermal degradation.

The unsaturated polyester is a solvent monomer resin system consisting of unsaturated pre-polymer chains and an unsaturated monomer. The unsaturated polyester is a co-polymer containing a mixture of saturated and unsaturated acids [10]. The saturated acid is often a phthalic acid isomer. Orthophthalic is commonly chosen because the anhydride may be used as a substitute. In this system phthalic anhydride was selected. This composition is often referred to as general purpose resin and is shown in Figure 1.

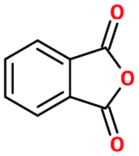

Figure 1. Phthalic Anhydride $C_8H_4O_3$

Maleic anhydride, shown in Figure 2, is the unsaturated acid in this resin system. It is preferential to other acid formulations because it is available as an anhydride.

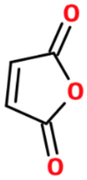

Figure 2. Maleic Anhydride $C_2H_2(CO)_2O$, unsaturated acid

Polyesters are formed through condensation polymerization of a di-carboxylic acid (e.g., di-acid) and a di-ol (e.g., glycol), which produces excess water. Propylene glycol, shown in Figure 3, was the di-ol in this system.

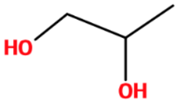

Figure 3. Propylene glycol $C_3H_8O_2$, glycol

Styrene, shown in Figure 4, is the unsaturated monomer in the system.

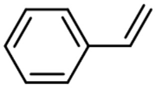

Figure 4. Styrene C_3H_8, unsaturated monomer

To activate the polymerization process, a free radical initiator, methyl ethyl ketone peroxide (MEKP), is introduced to the system, where it will decompose. The MEKP was often incorrectly identified as the catalyst. The true “catalyst” for the reaction is an accelerator (e.g., cobalt naphthenate), added to the resin system to initiate the decomposition mechanism. The polymerization process produces a thermosetting polymer containing polyester chains with polystyrene crosslinks, as shown in Figure 5.

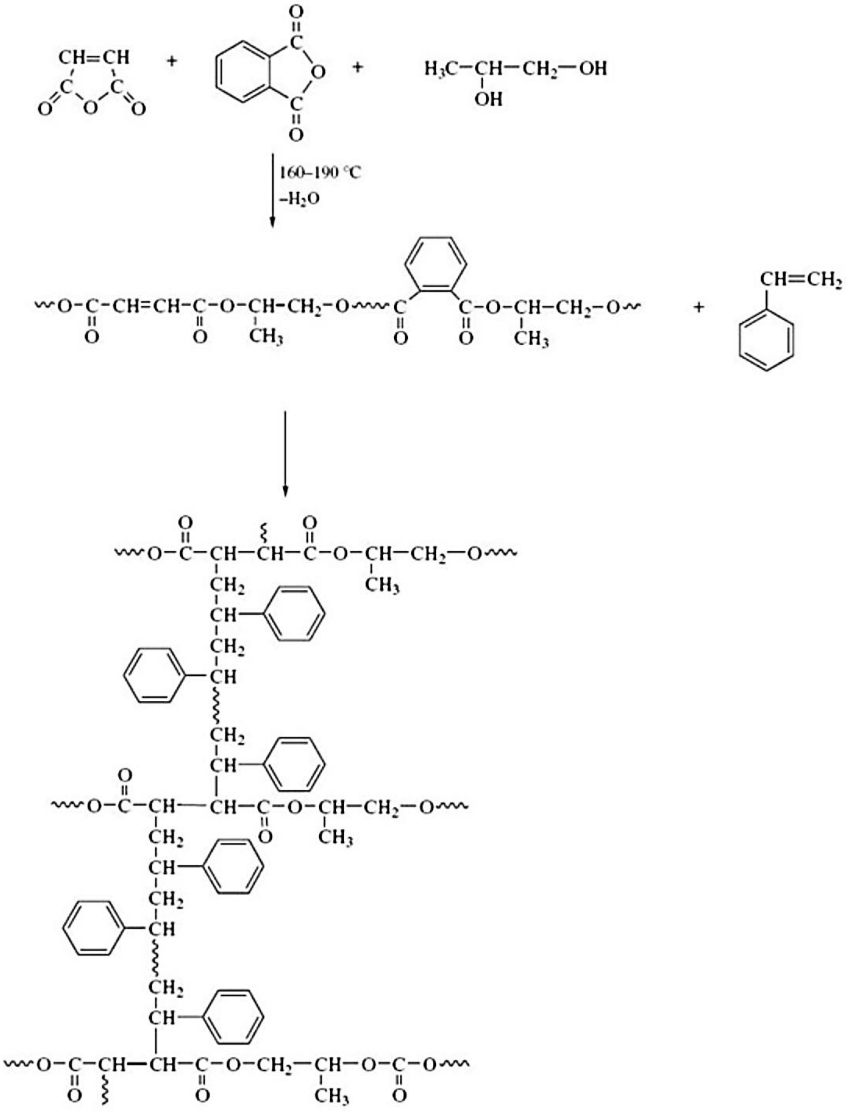

Figure 5. Repeating unit for the crosslinking in the cured resin system.

The fabrication process rarely results in a full cure because the polymerization reaction causes the system to become more rigid and immobile as curing proceeds. The mobility of the radicals is continually reduced until they are rendered immobile, unable to move to the reaction site to continue the polymerization process. The presence of water, produced during the condensation of the di-acid and di-ol, is one factor that influences the degree of polymerization achieved during the cure [10]. As long as the water remains in the system, there is a chance that hydrolysis (i.e., the reverse reaction) will occur. The other factors that influence the degree of cure are the length and temperature of the cure. If a full cure is desirable, a post-cure in an oven or at ambient conditions for an extended period of time is often included at the end of the fabrication process.

A number of reinforcements are available for fiberglass including E-glass ("E" for electrical grade), S-glass ("S" for stiff, high tensile strength), R-glass ("R" for reinforcement with high mechanical strength), D-glass ("D" for high dielectric performance), etc. Each type has a slightly varied composition to produce a composite with favorable material properties. Further variations exist for the type of production technique, style (weave and fill), and finish, which will be addressed in a later section. E-glass was selected for this investigation because it is one of the most common fabrics selected as the reinforcement for polymer reinforced composites.

E-glass (i.e., electrical grade glass) was originally developed as an insulation for electrical wiring and was later applied to other applications for its favorable material properties, including low cost, high strength, high stiffness, heat resistance, non-flammability, chemical resistance, water resistance, and prominence in manufacturing

[10]. E-glass is typically composed of 53-57 wt% Silica (SiO_2); 12-15 wt% Alumina (Al_2O_3); 22-26 wt% Calcium oxide (CaO) and Magnesium oxide (MgO); 5-8 wt% Boron oxide (B_2O_3); 0-0.6 wt% Flourine (F_2); less than 1 wt% Sodium oxide (Na_2O) and Potassium oxide (K_2O); and approximately 0.5 wt% Iron (III) oxide (Fe_2O_3). The glass fibers will begin to soften at approximately 1103 K and will melt at temperature in excess of 1343 K [10]. The fabric is composed of inorganic materials that are noncombustible and will not undergo decomposition when exposed to the external heat fluxes prescribed in this procedure.

1.1.1 Fabrication of Composites

Composites are fabricated by initiating the polymerization reaction in the resin and permeating the solution through the reinforcing fiber. There are a number of manufacturing processes available in industry for fabrication, including pultrusion, gun roving, filament winding with the use of a mold, etc. Pultrusion is a slow process where the strands of reinforcement are coated with resin and pulled through a preformer that presses the strands into the desired shape. In the gun roving process a strand of fiberglass is mechanically cut into small segments and mixed into a stream of resin to be sprayed over a mold. Pressure must be applied to compress the mixture over a mold. Filament winding is a process where the strands of fiberglass are coated with resin and wound around a rotating circular mold to form hollow, cylindrical products. When a standard mold is used, layers of fiberglass fabric are pressed into the mold and the resin is applied by hand or by using a vacuum to pressurize the mold.

For the individual interested in fabricating a composite, the most cost-effective and efficient processes include either a hand layup or a vacuum bagging procedure within a mold. In the vacuum bagging method, all of the reinforcement layers are placed in an airtight mold and the resin is evenly poured across the surface. The mold is sealed and a vacuum pump is applied to create a pressure differential large enough to infuse the resin evenly through the reinforcement layers. The resulting composite is typically of a higher quality than a composite fabricated by hand. Vacuum bagging is common in applications where the process will be repeated numerous times and the final product is too large to feasibly lay by hand.

The hand layup method requires the resin to be manually applied to each individual layer of reinforcement using tools such as paintbrushes, squeegees, and plastic rollers. One challenge with this process is the limited time window available for the resin to completely wet the reinforcement before polymerization, typically about 20-40 minutes after the initiator is mixed into the resin. This process quickly becomes time-consuming, requiring multiple batches of resin to be mixed for even small composites. This method often produces a ‘wet’ composite, which indicates that excess resin was introduced to the system resulting composite that will have, relatively, unfavorable structural properties. The resulting composite will often contain inconsistencies in the thickness of the composite sample and the thickness of individual layers of resin, and imperfections including air bubbles. An experienced practitioner will have the knowledge and skill necessary to mitigate these sources of aberration to a considerable degree.

The hand layup method was considered preferential for the fabrication small composites and for applications where the structural integrity was not a consideration. The bench-scale testing performed in this investigation required samples with a small surface area and the mechanics of the composite were not of primary importance. After considering the cost and benefits of the available methods, the hand layup process was selected to fabricate the samples for this investigation. A considerable amount of time was spent by the researcher fabricating practice samples using different materials, techniques, and compositions to become conversant with the process and ensure the quality of the finished product.

1.1.2 Existing Models

The pyrolysis of a polymer composite is a complex phenomenon featuring a number of controlling processes. Mouritz and Gibson [10] presented a description of the fundamental events they believed to occur when a composite is exposed to an external heat flux. The onset of the thermal insult produces a temperature gradient at the surface of the composite. The temperature gradient progresses along the fibers of the highly conductive reinforcement with less resistance than the polymer matrix producing anisotropic temperature profiles through the composite. Carbon and organic fiber reinforcements have a relatively high thermal conductivity compared to glass fibers. Fiberglass will exhibit the converse of this behavior, producing nearly isotropic temperature gradients. Non-uniform heating through the condensed phase will cause disproportionate expansion across the isotherms within the sample. The rising temperature of the material will initiate the thermal decomposition of the resin and production of volatiles within the expanding reaction zone. The hot gaseous products of decomposition will dissipate away from the reaction zone, through the condensed phase matrix, to the sample to the surface where they are released into the ambient atmosphere. This outward flow of hot gases is balanced by the inward flow of ambient gases to the composite. Pressure will build within the sample if the flow rates are not equal. The non-uniform expansion and possible pressure gradients may lead to thermally-induced strains within the condensed phase, which may result in delamination and formation of matrix cracks in extreme circumstances [10]**.**

A number of distinctive behaviors are cited in this description of the composite, many of which are attributed to the microstructure and relative properties of the constituents. The majority of these processes are not represented in the pyrolysis models currently available for composites. Most of the previously developed models describe the composite using a single component and perform analysis for only one composition. However, these models are fundamental to the development of a robust and dynamic model that can be applied to an expansive range of conditions. The historical progression and individual advancements in model development for composites were analyzed to gain a comprehensive knowledge of the current state of pyrolysis modeling for reinforced polymer composites. Consideration was given to the specific objectives of each researcher, their unique process for experimental testing and model parametrization, and the limitations of their methodology. These predecessors provided the foundation for the current investigation and the unique contribution presented within this investigation.

Das and Baijal [11] presented one of the earliest works in 1982 when they analyzed a “styrene-polyester copolymer” using TGA, DTA, IR spectroscopy, pyrolysis gas chromatography, and gas chromatography-mass spectrometry (GCMS). The material they tested has developed into what is currently known as unsaturated polyester resin and is typically purchased as a premixed solution. Their objectives were to determine the impact on the degradation process resulting from of an oxidative environment and the degree of crosslinking within the system.

The thermal decomposition process was characterized in TGA experiments conducted in an inert atmosphere as well as an oxidative atmosphere at various purge flow rates [11]. The pyrolysis gas chromatography identified the volatiles as carbon dioxide, propylene, methane, styrene, benzaldehyde, propylene glycol, phthalic anhydride, phthalic acid, and long-chain ester molecules. Results from the TGA were analyzed using an isothermal method.

This method was employed for the experiments performed in an inert atmosphere and two distinct reaction were identified. The first feature was determined to be an individual reaction and the seconds was resolved further using two separate reactions. The refinement from the two reaction model to the three reaction model was possible because of the precision of the instrument and test. Arrhenius rate equations were employed to characterize each reaction using a direct solution method. The results indicated that there was no definitive trend between the activation energy and the level of crosslinking.

Within the reaction mechanism, the first reaction was identified as the formation of unstable hydroperoxide. The second step was identified as the scission of cross links and weak links in the linear chains. The third step was determined to be the random scission of free linear chains formed during the second reaction. During oxidative degradation there was a single, first-order reaction. It was proposed that the presence of oxygen causes a change in the rate of scission of cross/weak links and the random scission of free linear chains such that both mechanisms are described by a single rate constant [11].

This investigation provided a basis for the degradation mechanism in the UP resin system. Unfortunately, there was little practical application to employ these results. The milligram-scale analysis was only appropriate for one dimensional analysis. The thermodynamic processes were not yet characterized and the thermally-thin assumption was a significant limitation. The next step in model development would require a methodology to parameterize the heat transfer processes occurring within the decomposing polymer network.

In 1985, Henderson et al. [12] was one of the first investigations to expand modeling from the degradation kinetics to include the thermodynamic properties and performance of the composite. Henderson used an nth-order finite-rate reaction mechanism with two competitive reactions to describe the thermal degradation of a phenolic-formaldehyde reinforced with glass resin and the carbon-silica reactions. Temperature- and mass- dependent thermal and mass transport properties were characterized. The model assumed thermal equilibrium between decomposition gases and the condensed phase and included terms to account for the diffusion of decomposition gases through the structure, but neglected the accumulation of gases in the solid and thermochemical expansion. The temperature-dependent specific heat capacity of the resin and char developed by Henderson is still commonly referenced in literature today [12]. Many researchers have based their models on this analysis method.

The reaction kinetics were parameterized from TGA using a variation of Freidman’s multiple heating rate technique for the carbon-silica reaction. It was proposed that in an ablative material the carbon from the char would react with the oxygen in the silica to form carbon dioxide and a residual silicon [13]. The pyrolysis reaction was characterized using a similar method with a variation where the process was divided into two regimes based on a critical normalized mass loss. One reaction mechanism was specified for m/m_0 greater than 0.91 and another for m/m_0 less than 0.91 [12].

The specific heat capacity and heat of decomposition were parameterized from a standard method using DSC. A linear temperature dependency was assumed for the specific heat capacity of the virgin material and the char. The heat of decomposition was quantified as the difference between the area under the curve of the apparent heat capacity and the specified heat capacity of the components [12].

The thermal conductivity of the virgin material and the char was measured using the line-source technique. The thermal conductivity of the virgin composite was found to have a weak linear dependence on temperature. The char was found to have an overall linear dependence with a strong temperature dependence above 773 K, which was characterized using a third order polynomial [12].

The parameterized model was evaluated for the ability to predict the in-depth temperature profile of the composite exposed to a significant thermal insult, specifically an external heat flux of 279.7 kW m^{-2}. The complete set of material properties was presented during the initial investigation but is not reproduced here because the composite samples consisted of a different polymer matrix. Also, a comparison between the properties for the glass reinforcement could not be made because the type of glass reinforcement was not specified and there are a variety available. The selected heat flux was considerably higher than the values used in comparable testing and resulted in dramatically greater temperature gradients, both spatially and over the course of the test. The maximum deviation between the predicted temperature profiles and the experimentally measured in-depth temperature profiles were in excess of 343 K [12].

In the following years the cone calorimeter became prominent for bench-scale testing [14]. The benefit to the design was the truncated conical shape that was able to provide a uniform heat flux to the surface of a material and resulted in reproducible heat release rate profiles as a function of time. The data from cone calorimeter testing included the time to ignition, peak heat release rate, total heat release rate, and average heat release rate. The results were consistent, but of little use for modeling. Once the sample ignited and the flame formed at the surface, the heat transfer to the sample was no longer well-defined. Characterizing the heat flux from the flame to the sample has been arguably the largest hurdle for modeling cone calorimeter data.

In 2011, Lattimer, Ouellette, and Trelles characterized the degradation kinetics and thermodynamic properties for a woven glass-reinforced vinyl ester composite. Their methodology used TGA and DSC to test composite samples that were approximately 1 mm thick, 3 mm wide, and 4 mm long [15]. A cross-section of the composite was filed to produce powder samples. The kinetics of degradation were quantified using the data from these milligram-scale tests in addition to the sample mass history measured in the thermal decomposition apparatus (TDA).

Experiments were performed on coupon-size samples in the TDA to provide a variable heating rate and constant heat flux during independent simulations to target specific material properties. The variable heating rate simulations were used to parameterize the Arrhenius rate reaction parameters and the density as a function of temperature.

The constant heat flux simulations were used to characterize the thermal conductivity and specific heat capacity of the virgin resin, the composite, and the glass components. Table 1 below shows the resulting expressions for the thermal conductivity and specific heat capacity.

Table 1. Material properties characterized by Lattimer et al. [15].

Component	Thermal Conductivity ($W\ m^{-1}\ °C^{-1}$)	Specific Heat Capacity ($J\ kg^{-1}\ °C^{-1}$)
Virgin Composite	$k_v = 4.405 \times 10^{-5}\,T + 0.312$	$c_v = 0.0452\,T + 1080$
Char/Glass (decomposed)	$k_d = 2.83 \times 10^{-4}\,T + 0.0949$	$c_d = 0.259\,T + 1041$
Glass	$k_g = 1.873 \times 10^{-4}\,T + 0.0585$	$c_g = 0.285\,T + 1298$

The values for the thermal conductivity of the virgin composite ranged from 0.3-0.35 W $m^{-1}K^{-1}$, the composite (char/glass) intermediate ranged from 0.1-0.3 W $m^{-1}K^{-1}$, and the glass ranged from 0.05-0.22 W $m^{-1}K^{-1}$ [15]. The characterized values for the thermal conductivities of the initial composite sample and the intermediates formed during decomposition were within the range typical of polymeric materials. The thermal conductivity of E-glass has been reported in literature as 1.13 W $m^{-1}K^{-1}$, which is considerably larger than the experimental value defined in this model [10].

The values defined in the model for the specific heat capacity of the virgin composite range from 1050-1120 J $kg^{-1}K^{-1}$, the char/glass intermediate range from 1050-1200 J $kg^{-1}K^{-1}$, and the glass range from 1300-1520 J $kg^{-1}K^{-1}$. These ranges all agree well with commonly reported literature values [12].

The apparent specific heat capacity is reported as a function of temperature for fragment and powder samples tested using DSC and for coupon-sized samples tested in the TDA. There is some variation between the curves for the two tests evaluated using DSC, with notable variations between the DSC measurements and the TDA measurements. The location of the peak endotherm shifts more than 60 K and the final heat capacity of the samples varies more than 300 J $kg^{-1}K^{-1}$. The resulting heats of decomposition were calculated for each sample type, which resulted in an approximate 100% variation between DSC and TDA results.

It is interesting to note that for the fragment sample, the initial mass was reported as 0.01321 g and the decomposed mass was reported as 0.00850 g. The composition of the initial sample can be estimated by assuming that all of the resin decomposed with no char yield, which would be expected to produce a lower bound for the wt% resin composition. For the fragment sample, the ‘lower bound’ is calculated to be 35.6 wt% resin, which is 5.6 wt% above the reported composition. The lower bound for the powder sample was calculated as 28.2 wt% resin and for the coupon-sized sample as 26.6 wt% resin. These variations may be typical for composites, however, they are significant for samples that are identified as being of the same initial composition for pyrolysis modeling. It would be necessary for the model to characterize the constituents individually in order to account for the variations in composition during experimental testing.

Zhou and Yu investigated the ability of a finite-rate model and an infinite-rate model to accurately predict experimental measurements from bench-scale cone calorimeter and intermediate-scale calorimeter testing for fiberglass reinforced polyester composites [16]. The samples tested were fabricated through a pultrusion process.

The kinetics of decomposition can be described using either fine-rate or infinite-rate models. Finite-rate models typically employ a series of Arrhenius rate reactions to reproduce the experimental data from TGA. Infinite-rate models assume that the sample is composed of distinct regions of virgin material and char that are separated by an infinitely thin pyrolysis front region. The location of the pyrolysis front is dictated by the critical sample temperature for the onset of pyrolysis.

TGA data was analyzed to describe the kinetics, but the experiments were conducted in an aerobic environment, which has been shown to produce changes in the reaction mechanism due to oxidation [11]. A single, n-th order reaction was characterized to describe the decomposition of the composite sample as a whole [16]. The material properties that were selected to evaluate the model have been provided in Table 2 below.

Table 2. Material properties characterized by Zhou and Yu for fiberglass reinforced polyester composite [16].

Property	Value
$\rho_{virgin\ resin}$	$1888\ (kg\ m^{-3})$
$\rho_{decomposed\ char}$	$1133\ (kg\ m^{-3})$
$c_{p,fiber}$	$760 + 3.88\ x\ 10^{-2}\ T\ (J\ kg^{-1}K^{-1})$
$c_{p,resin}$	$1600 + 0.8\ T\ (J\ kg^{-1}K^{-1})$
k_{fiber}	$760 + 2.05\ x\ 10^{-4}\ T\ (W\ m^{-1}K^{-1})$
k_{resin}	$0.2 - 1.356\ x\ 10^{-4} T\ for\ T \ll 200℃\ (W\ m^{-1}K^{-1})$ $0.2 + 2\ x\ 10^{-4} T\ for\ T > 200℃\ (W\ m^{-1}K^{-1})$
V_{fiber}	0.2872
W_{fiber}	0.4

The finite-rate model was based on Henderson's model [12]. The infinite-rate model was evaluated using finite-rate methods. A discontinuity was created at the boundaries of the reaction zone due to the instantaneous change in material properties. To address this issue, the pyrolysis region was described by a number of discrete steps, which allowed for a more gradual transition in property values [16]. The dependence of the pyrolysis temperature on the heating rate was described by Equation 1, where $T_{p,max}$ and $T_{p,min}$ are the boundaries for pyrolysis and were measured experimentally as 639.4 K and 579.7 K, respectively.

$$T_p = T_{p,max} - (T_{p,max} - T_{p,min})e^{-\beta/9.21586} \tag{1}$$

The main criticism of the work by Zhou and Yu [16] is that there is no consideration given to the material properties used to evaluate the performance of the models. The values are stated without any justification. The model results are sensitive to the material properties. Deviations between the simulated results and the experimental data cannot be directly attributed to insufficiencies in the model without decoupling the error caused by the input parameters from the error caused by the pyrolysis mechanism.

In 2009, Kim, Lautenberger, and Dembsey [17] parameterized a model with independent consideration for the constituent materials in an attempt to achieve objectives similar to those proposed in the current investigation. TGA/DSC testing was conducted in a nitrogen environment on a brominated polyester resin to develop the kinetic model for thermal decomposition. The iso-conversional method was used to identify three competing reactions. The parameters for a single-step and three-step reaction mechanism were optimized using a generic algorithm (GA) coupled with a pyrolysis model [18].

Fiberglass samples were fabricated with alternating layers of fiberglass chopped strand mat and glass woven roving. One composition consisted of 5 sets of alternating layers (5 layers of chopped strand mat and 5 layers of woven roving) and another of 4 sets of alternating layers, which produced samples of 41 wt% resin and 67 wt% resin, respectively [18]. The samples were tested in the fire propagation apparatus (FPA) with simultaneous recording of the sample mass and temperature profile using thermocouples at varying distances from the surface of the sample. Parameterization was performed for the thermodynamic and optical properties, along with the heats of decomposition. Data collected on the sample with 67 wt% resin was selected as the target for the temperature profiles, the heat flow from DSC. The GA was used to optimize the properties for the three-step reaction mechanism for two cases, targeting the heat flow rate data from DSC. One case used the assumption of a heterogeneous microstructure and the second case was constructed for a homogeneous microstructure. The specific heat capacity and thermal conductivity were assumed to have a temperature dependency described by Equation 2.

$$k(T) = k_0\,(T/T_r)^{n_k} \tag{2}$$

In this expression T_r is the reference temperature, k_0 is the reference thermal conductivity, and n_k is the conductivity temperature dependency. The difference between the material properties for the two assumed microstructures was less than 30%.

The model was evaluated for the ability to simulate the experimental data from the FPA using the properties characterized for the three-step reaction mechanism and heterogeneous microstructure. These properties were held constant and the simulation results were evaluated for the set of four possible combinations of assumptions for a heterogeneous or homogeneous microstructure, and single-step or three-step reaction mechanism. All of the configurations were able to accurately model the temperature profiles through the solid. The mass loss rate of the sample was adequately modeled, and the heterogeneous microstructure was able to resolve the oscillation in the experimental data.

The same set of parameters was evaluated for the ability to replicate the FPA data for the 41 wt% resin sample composition. The model was able to accurately reproduce the temperature profile, but the modeled mass loss rate did not agree with the experimental measurement. The homogeneous model was more representative of the experimental mass loss rate profile, and the heterogeneous microstructure showed significant deviations. This discrepancy between experimental data and model simulations was attributed to variation in the microstructure of the sample at the surface compared to the ideal structure assumed in the model.

The composition of the composite was varied in the experiments. This change in composition resulted in an approximately 44% decrease in the peak mass loss rate from the 67 wt% resin sample to the 41 wt% resin sample. The sample at 41 wt% resin did not have an initial peak, but rather increased to a quasi-steady value. Both sets of experimental data did not appear to support the substantial dip in the mass loss rate that was present in the heterogeneous model, but rather appear to support approaching a steady value [18].

The basis for this method was that the mass loss rate would be well reproduced when the temperature profiles were accurately fit from the optimization using the GA. The temperature profile at 41 wt% resin was reproduced well by the model, which theoretically should accurately simulate the mass loss rate. Even if the microstructure is a major source of error, the parameterization was selected based on the heterogeneous GA optimization. If the microstructure was to be the source of the inaccuracy, then the accuracy of the material properties that were determined based on that microstructure cannot be guaranteed. The material properties for the homogeneous GA optimization should have been evaluated to support the claim that the material properties are valid while the microstructure was not valid; otherwise, the evidence would indicate that the material properties may also have been at issue in this study.

1.2 Objectives

The scope of this investigation is to develop a methodology to characterize the material properties of constituents within a composite to describe pyrolysis and demonstrate the ability of the model to be extrapolated over a range of composition ratios. The constituent materials are parameterized using a combination of four strategies that included (1) the direct measurement from experimental testing, (2) the assumption of literature values, (3) the determination the property values through inverse analysis, targeting experimental data, which is manually iterated in a comprehensive pyrolysis model, ThermaKin, and (4) assumptions about the behavior of a material property for an identified intermediate species relative to other species. The final strategy recognizes the limitations in pyrolysis research, which lacks the ability to isolate the formation and consumption of intermediate species for independent experimental testing. Conservative assumptions are often favorable for these scenarios, when there is not enough information to make a justifiable determination for the behavior of a particular species.

As is characteristic of a semi-empirical model, the complexity of the parameterization depends on the discretion of the model developer. The number of variables can range significantly. This project sought to limit the number of variables in the system to reduce the complexity of the model, while still achieving the other performance objectives. A well-defined set of temperature-dependent material properties is developed to describe the effective degradation reaction mechanism in addition to the thermodynamic and optical properties.

The properties are assessed for agreement between predicted and experimental temperature profiles for UP resin and the twelve sample composition/external heat flux configurations during radiation-driven gasification experiments. Validation is provided for the fully parameterized model by evaluating the agreement between the simulated mass loss rates with the experimental data. The model is characterized using a limited set of experimental data, and validation will be provided for all of the compositions at each heat flux.

2. Methods and Materials

2.1 Sample Material

The samples were prepared using wax-free, general purpose polyester resin and 10 oz style 7500 woven (E-glass) fiberglass fabric. The resin was formulated to cure when combined with MEKP in the amount of 1.25% of the mass of the resin. The glass fabric and the polyester resin were purchased from the same distributor, Fiber Glast. Resin samples were prepared for all milligram-scale and bench-scale testing. Composite samples were prepared for gasification experiments. The fiberglass chosen for the composite was standard style 7500 with a plain weave, as shown in Figure 6.

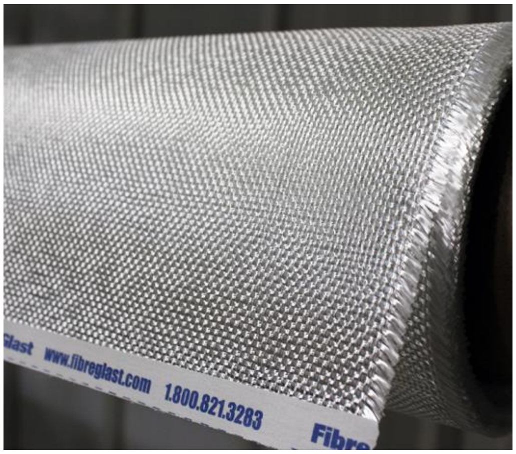

Figure 6. 10 oz fiberglass fabric *[19]*.

This fiberglass is one of the most popular medium weight E-glass fabrics because of its excellent balance of cost, weight, and strength. The fiberglass is electrical continuous filament (ECG) with an average diameter of 9 microns. The finish is specified as a volan chrome complex (504), which promotes the adhesion of the UP resin to the fiberglass reinforcement [19]. This finish gives the composite a green tint and ensures the bonding of the resin to the reinforcement during the polymerization of the unsaturated polyester resin. The weight of the fabric was specified by the manufacturer as 9.64 oz yd^{-2}, commonly listed as 10 oz fabric, and the thickness was specified as 0.0154 inches per layer of reinforcement [19]. It is important to note that the thickness of the woven fabric is greater than the thickness of the individual strands. This fabric is compatible with polyester, vinyl ester, and epoxy resins. Literature values have characterized the density as 2540 kg m^{-3}, the coefficient of thermal expansion (CTE) as 4-5.5 μm $m^{-1}K^{-1}$, the specific heat capacity as 0.78-0.82 J $g^{-1}K^{-1}$, the thermal conductivity as 1.28-1.32 W $m^{-1}K^{-1}$, and the softening point as less than 1113 K [20].

The polymer system consisted of the previously described UP resin, of phthalic anhydride, maleic anhydride, and styrene, which polymerizes into a thermosetting network of polyester chains with polystyrene cross-links [10]. An exemplar UP resin sample is shown in Figure 7.

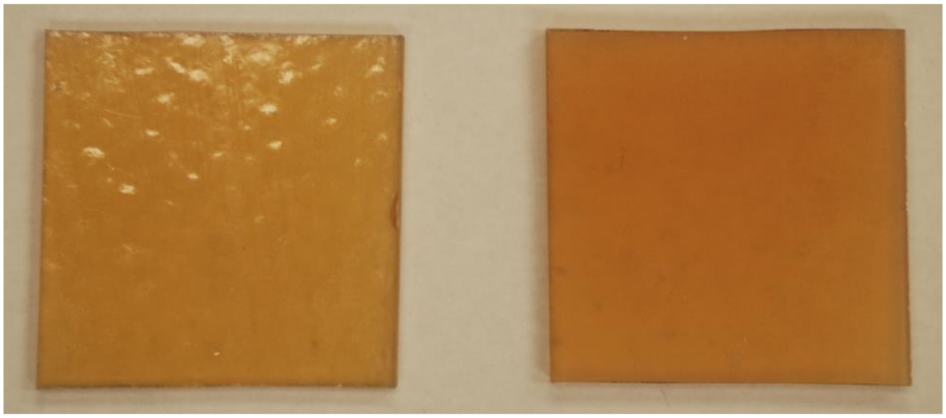

Figure 7. UP resin sample, the glossy surface (left) was exposed during fabrication and the matte surface (right) was against the mold.

The supplies were purchased from an industry-leading third party distributor. The distributor is only involved in the purchasing and selling of the materials, which were obtained from the manufacturers. The materials purchased from the distributor may come from a variety of manufacturers that will prepare a unique product with variations in the ratio of chemical components and the introduction of additives. For example, polyester resin has a relatively short shelf life after the container is opened and the resin is exposed to an oxidative environment. Inhibitors are commonly added during the production of the polyester resin to slow the polymerization process which will naturally occur within the unsaturated resin over an extended period of time. Unfortunately, the impact of these various additives cannot be considered because the distributors have a contractual obligation that prevents them from naming the manufactures of a particular product. In this investigation, the materials are assumed to be representative of the general compositions and standard fabrication processes identified by the distributor.

Composite samples, shown in Figure 8, were prepared using a hand layup method at composition ratios of 41, 48, and 54 wt% resin.

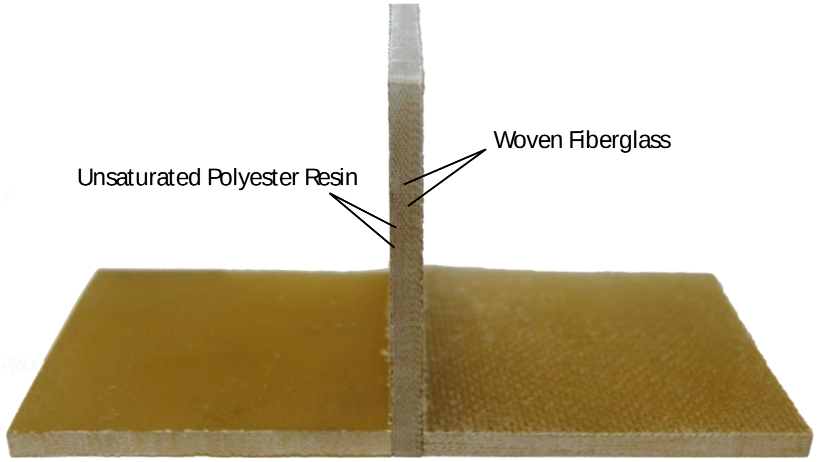

Figure 8. Fiberglass sample fabricated using a hand lay-up method with woven fabric and unsaturated polyester resin (top/side/bottom).

The most ideal composite, in terms of uniform distribution of resin and complete saturation of the fiber reinforcement, fabricated using the hand layup method had the same mass of resin and reinforcement. When the amount of resin was reduced the composite samples had air pockets where there may not have been enough resin to fully saturate the fibers. When the amount of resin was increased the distribution of the resin through the composite may have been non-uniform through the samples. The range of compositions was selected to produce the most ideal samples in addition to samples with compositions that favored each of the constituents.

A mold was used to achieve a uniform distribution of resin throughout the composite. The mold was made of PVC and measured approximately 21.5 inches by 9.5 inches and 0.5 inches deep. Each sample consisted of 16 layers of fiberglass to achieve a thickness of approximately 5-7 mm, in order to establish thermally thick behavior. The orientation of the fabric was not varied between alternating layers to facilitate the consistent behavior of layers within the composite. A layer of wax was applied to the mold to ensure the cured resin could be removed from the mold without damaging the samples. While preparing to fabricate the samples, the exact quantity of constituents to be used was determined, but the imprecise nature of the fabrication method resulted in variations of approximately ± 6% between the preselected composition and the final sample. The compositions selected for fabrication were 40, 50, and 60 wt% resin and the resulting GRP samples were determined to be 41, 48, and 54 wt% resin. An experienced user is able to intuitively compensate for the losses in the process, but every layup is unique and no two samples will be the same. This process was also used to fabricate UP resin samples for gasification experiments. Resin samples were prepared for milligram-scale testing by spreading a thin layer of resin over aluminum foil to facilitate the fine particle size necessary to ensure non-dimensional (i.e., thermally thin) behavior.

An important observation to note was that one side of the sample had a glossy, smooth appearance and the other had a matte, abrasive appearance. This difference was a result of the fabrication process. The individual layers of fiberglass were placed in the mold, and the resin was stippled onto the fiberglass until it was wet through. This process was repeated a total of sixteen times, then the remaining resin was applied to the top of the final layer of fiberglass, and finally the sample was left to cure. This process caused the initial layer to be compressed to the mold, and upon release the indentation from the structure of the woven fiberglass was imprinted along the bottom surface. The top of the mold was open to the ambient air, in the fume hood, where the samples were fabricated. The excess resin added to the system was more concentrated at the top of the sample for compositions with higher resin/glass ratios, which resulted in a smooth glossy appearance.

The samples were allowed to cure at room temperature for twenty-four hours. The degree of cure has been shown to have a significant impact on the properties of the composite, so the samples were post-cured in an oven to ensure a full cure. The DSC was utilized to determine the correct temperature for the post-cure, which will be described in greater detail in a following section. A full cure was achieved by placing the samples in an oven for an hour at 343 K. During this process, the samples were observed to shrink and darken from a translucent tan to a dark amber color, indicative of a chemical reaction. To minimize the effect of moisture content, all samples were stored in a desiccator for at least 48 hours prior to testing.

2.2 Milligram Scale Experiments

A simultaneous thermal analyzer (STA) that couples thermogravimetric analysis (TGA) with differential scanning calorimetry (DSC) was employed to conduct milligram-scale experiments in a Netzsch F3 Jupiter, shown in Figure 9.

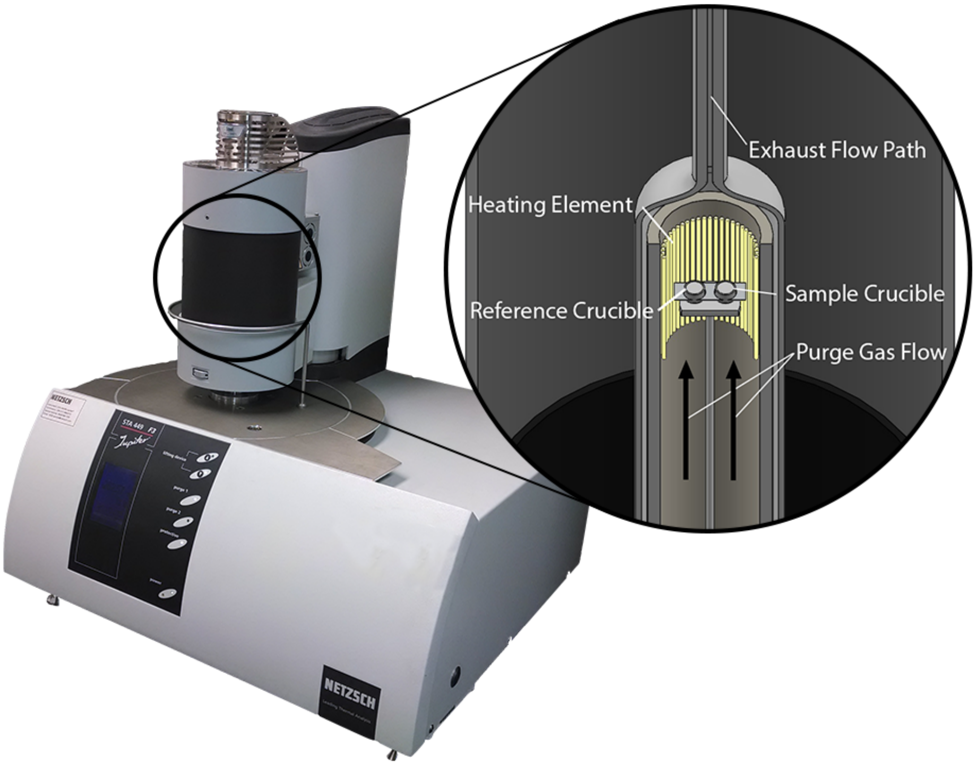

Figure 9. Nezsch F3 Jupiter.

The differential (twin) calorimeter consists of a vertical furnace capable of uniform heating through a user specified linear heating rate. The heating rate is achieved by continuous scanning of the surrounding furnace temperature. The apparatus is equipped with a 1 μg-resolution microbalance and P-type thermocouples at the sample carrier which provide experimental measurements for the TGA and heat flux DSC methods, respectively.

The sample is placed in a Platinum-Rhodium crucible with a lid. The lid has a 0.25 mm hole intended to increase the stability of the measurements by allowing the transport of gases. The heat flux DSC method is based on the differential temperature measurement, in the form on an electrical potential difference, between the sample crucible and the reference crucible. The heat flow sensing thermocouple is located under the sample crucible and a reference crucible. The temperature difference is assumed to be related to the heat flow rate. In practice, the measured signal is not directly proportional to the heat flow rate as a result of time delay and distortion due to non-ideal physical processes. Calibrations are performed to validate the accuracy of the system and the experimental measurements.

In heat flux DSC, the furnace produces a heat flow rate based on the user-defined linear heating rate. The sample and the reference are heated via a conductive path with well-defined thermodynamic properties. The primary measurement is the temperature difference between the sample and the reference. The measured heat flow rate is assumed to be proportional to the temperature difference by a factor determined through calibration. The resulting measured heat flow rate is dependent on both time and the temperature of the sample.

Thermal symmetry between the sample and the reference has been identified as a factor contributing to the accuracy of the measurement. The results are sensitive to the thermal contact between the sample and the crucible, particle size, and configuration of the crucibles. The resin samples were fabricated as a thin sheet and cured in the oven. The samples were mechanically ground using a mortar and pestle to reduce the individual particle size and then pressed into the bottom of the crucible to ensure adequate thermal contact between the sample and the crucible. Samples were between 6-10 mg. The position of the crucibles in the apparatus was monitored to provide consistency during testing. Seven tests were performed for both pure resin and char. The char was harvested from radiation-driven gasification experiments performed on UP resin samples at 70 kW m^{-2}.

The furnace is continually purged with nitrogen at a rate of 50 ml min^{-1} to create an anaerobic environment and to transport gaseous products of decomposition away from the condensed phase. Previous investigations have shown that in an aerobic environment, additional reactions occur due to the presence of oxygen [21]. The user-specified heating program began by heating the sample to 313 K and maintaining this temperature for 20 minutes. The isothermal period ensures that the system is at thermal equilibrium and that no oxygen is present in the system. This time also allows for the analysis of the symmetry in the system, which will cause deviations in the resulting DSC measurement. The system was then subjected to a linear heating profile of 10 K min^{-1} up to 1173 K. Analysis was conducted at this single heating rate due to a previous investigation which identified 10 K min^{-1} as the maximum heating rate that is capable of maintaining the sample at a uniform heating rate [22]. Finally, the system was maintained at this temperature for 15 minutes.

The testing conditions were performed with both crucibles empty to establish a correction for the experimental measurement. This correction, referred to as the zeroline, was used to establish the measured heat flow as a result of non-uniformities in the system configuration. The sample was then tested under the same prescribed heating program. The zeroline was subtracted from the heat flow measurement with the sample, yielding the heat flow associated with the sensible enthalpy.

Data was collected over the course of the complete heating program. The analysis utilized the mass and heat flow measurements during the linear heating phase. Initial testing analyzed the heat flow data from the DSC to determine the appropriate temperature for the oven post-cure.

2.3 Bench-Scale Experiments

2.3.1 Radiation Absorption

The broadband absorption coefficient was quantified using the radiant heater in the cone calorimeter and a water-cooled Schmidt-Boelter heat flux gauge to determine the radiative heat transfer through a thin resin sample. The experiments were performed using a method previously outlined by Linteris [23] and later implemented by Li [8]. Figure 10 shows the experimental configuration under the heater in the cone calorimeter.

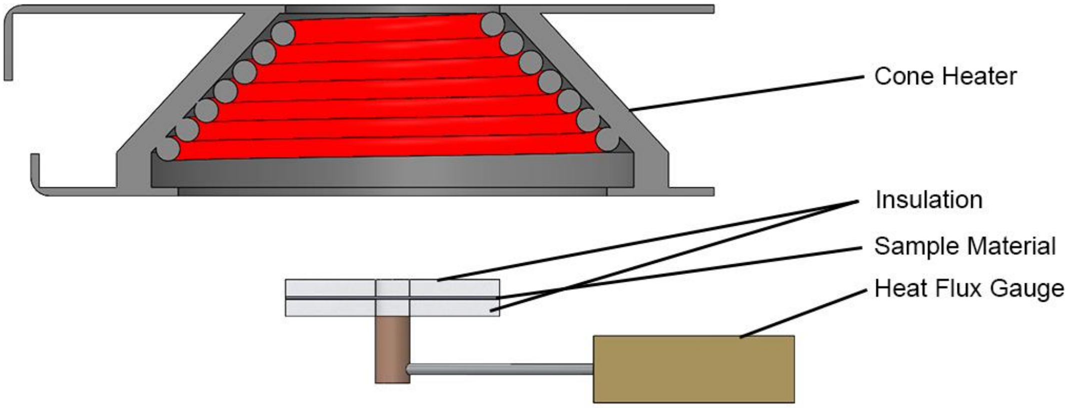

Figure 10. Experimental configuration for absorption coefficient measurement [8].

A piece of Kaowool, with a cylindrical hole corresponding to the size of the heat flux gauge, was mounted horizontally 34 mm from the radiant heater. The heat flux gauge was mounted at the bottom of the cylindrical hole. This configuration collimated radiation transmitted to the heat flux gauge. The radiant heat flux was assumed to be one-dimensional, and measurements were independent of wavelength variations emitted from the source (i.e., the heating element)**.**

UP resin samples were fabricated with thicknesses varying from 0.9 mm to 1.4 mm. The samples were placed on the Kaowool PM over the hole. The radiant heater was set to expose the sample to a radiant heat flux of 20 kW m^{-2}. The previous investigation was performed at an external heat flux of 35 kW m^{-2} [8]. The reduction in heat flux was necessary due to the rapid onset of thermal degradation observed at 35 kW m^{-2}. The heat flux gauge monitored the transmitted radiation for the first 10 seconds. At this time the sample was removed and incident heat flux was recorded for an additional 60 seconds. The heat flux measured by the heat flux gauge was assumed to be equal to the incident heat flux to the sample. Measurements were repeated three times to ensure agreement between the results. A steady value for the incident heat flux was taken for the period 5 seconds after the shutter was open, when the sample was present, and again after the sample was removed. These values, in addition to the sample thickness, were used in an expression based on the Beer-Lambert law to determine the absorption coefficient.

2.3.2 Gasification Experiments

A Govmark CC-1 cone calorimeter equipped with the Controlled Atmosphere Pyrolysis Apparatus (CAPA) and a FLIR Compact Infrared Thermal Imaging Camera was used to perform radiation-driven gasification experiments. The composite was machined into squares with 80 mm sides. The configuration of the truncated cone heater, CAPA, and infrared camera are shown in Figure 11 and Figure 12.

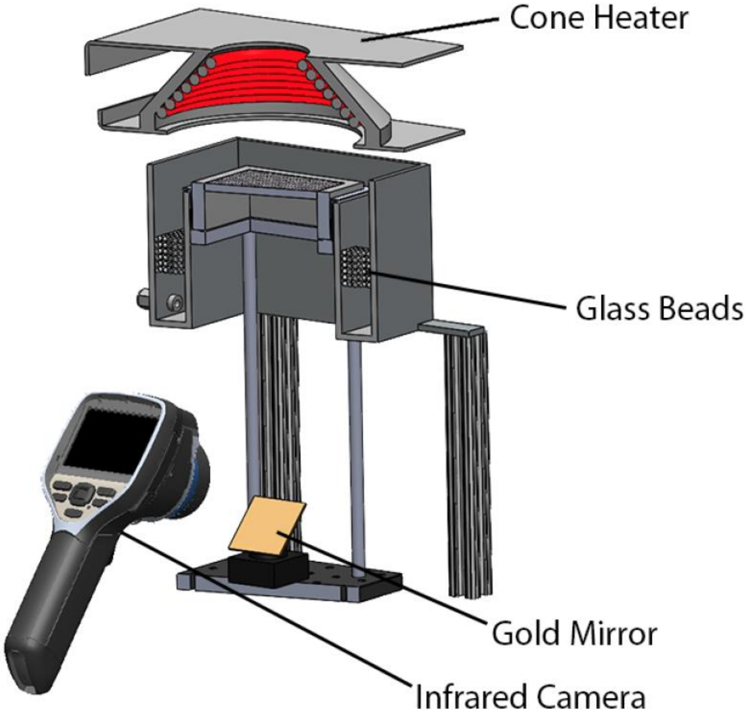

Figure 11. Schematic of the experimental apparatus used during radiation-driven gasification experiments. The truncated cone heater, CAPA, and infrared camera are shown.

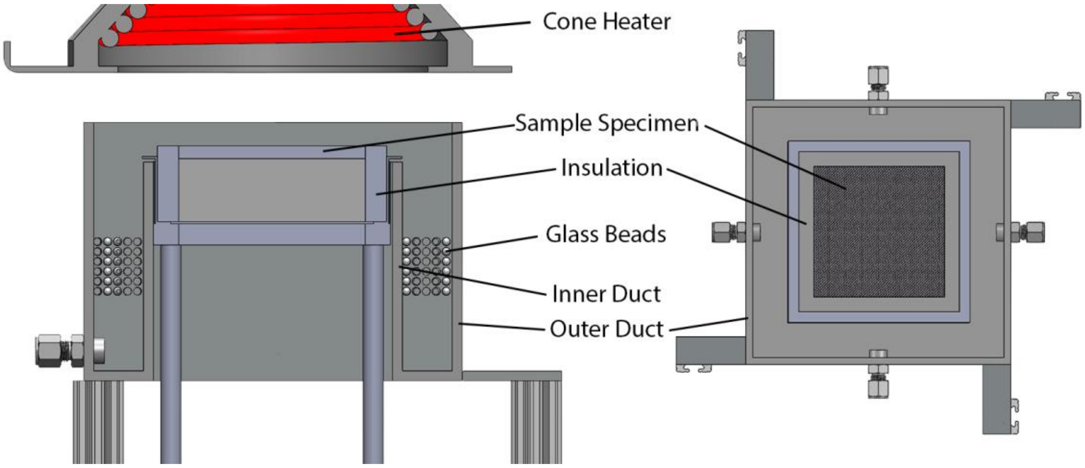

Figure 12. A closer cross-sectional (left) and top (right) view of the CAPA, used to purge the sample surface with nitrogen during radiation-driven gasification experiments.

The cone calorimeter was equipped with a precision balance, used to monitor the instantaneous mass of the sample. The CAPA was mounted below the cone heater and created a nearly anaerobic atmosphere at the sample surface by purging the sample with 225 SLPM of nitrogen through ports located at the midpoint of each side of the sample holder. The frame of the CAPA was designed to provide optical access to the back surface of the sample.

The truncated cone heater exposed the top surface of the sample to a steady radiant heat flux. Experiments were conducted at radiant exposures of 30, 50, and 70 kW m^{-2}. The heat fluxes were set using a Schmidt-Boelter heat flux gauge, mounted where the center of the sample was located. A previous investigation found the heat flux across the majority of the sample surface to be within 3% of the set point, with variations up to 10% at the corners [24]. Each testing configuration was repeated three times to increase the reliability of the results and to evaluate the repeatability of the measurements.

The sample was positioned horizontally 40 mm below the radiant heater. The back surface of the sample was coated with a paint of known emissivity, 0.95, and placed on a 0.8 mm-thick aluminum mesh. The edges of the sample were thermally insulated with a 5 mm wide piece of Kaowool PM, shown in Figure 13.

Figure 13. Sample holder with aluminum mesh and Kaowool.

The Kaowool insulation restricted off-gassing along the sides of the sample. This configuration effectively reduced edge effects and increased the validity of the assumption that the heat and mass transfer processes were one-dimensional. The Kaowool was conditioned under the cone heater prior to each test to prevent degradation of the Kaowool from influencing the mass loss rate measurement.

During experimental testing, the glossy surface was coated with the emissive paint and the matte surface was exposed to the radiation from the truncated cone heater. It was observed that the samples would expand and deform away from the wire mesh. This sample behavior would cause the transfer processes to no longer be one-dimensional. In an effort to mitigate this effect, wires were secured over the sample and around the mesh to prevent the sample from deforming away from the mesh. An exemplar sample configuration is shown in Figure 14. The wires were used to secure the sample for configurations where the composite was observed to deform, which occurred at the higher heat fluxes and when testing the UP resin samples. Samples were not secured with the wires when this behavior was not observed.

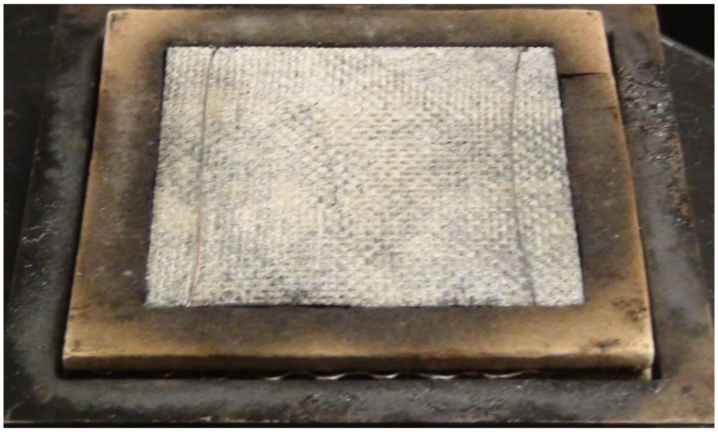

Figure 14. Sample secured in the holder to prevent deformation away from the wire mesh backing.

The infrared camera was mounted in line with the mirror and focused on the bottom of the sample to monitor the surface temperature. The temperature calibration for the camera required the surface emissivity to be provided as an input prior to experimental testing. The temperature data was measured at a rate of 7.5 Hz.

A previous investigation analyzed the accuracy of the temperature measurements and analysis method [8] [6]. A copper plate was coated with the emissive paint and equipped with two type K thermocouples while exposed to a steady radiant heat flux. The agreement between the measurements from the thermocouples and the IR camera was within 5 K for surface temperatures up to 650 K and approximately 10 K at higher temperatures [24] [25].

A single time-dependent temperature history for the entire sample surface was characterized by dividing the surface into three sections, shown in Figure 15.

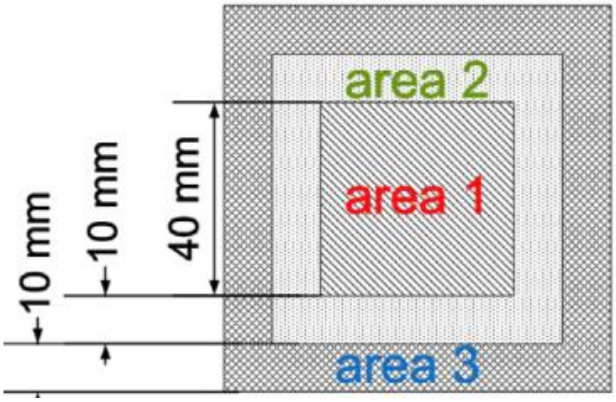

Figure 15. Areas defined for evaluation of the surface temperature and spatial variations across the sample [8].

The first area was a square region with a side length of 40 mm whose center corresponded to the center of the sample. This center region constituted 25% of the total surface area of the sample. Four points were selected within this region, and the temperature history was exported for analysis. The second area was the square region extending 10 mm outward from the sides of the first area. This region constituted 31.25% of the total surface area of the sample. Four points were selected within this region, and the temperature history was exported. The third area was the square region extending from the second region to the outer edge of the sample. Two points were selected within this region, and the temperature history was exported. The arithmetic mean, standard deviation, and uncertainty were evaluated at each time step for the data set. The uncertainty was calculated as two standard deviations of the mean. An average value was calculated for each configuration.

Previous testing, performed by Li [6], using this method was typically conducted with a piece of aluminum foil between the sample and the wire mesh. The foil was spray painted with the emissive paint, the purpose of which was to prevent viscous tar produced during the degradation of polymeric materials from dripping from the back surface of the sample. This observation would cause the mass data to erroneously indicate that additional mass was lost due to the formation of volatiles. The aluminum foil effectively prevented mass transfer from occurring across the bottom surface of the sample. Three fiberglass sample configurations were tested both with and without the aluminum foil backing. The resulting data and analysis for the back surface temperature and mass loss rate for the fiberglass samples, provided in Appendix I, supported the absence of the foil backing during experimental testing. A combination of the testing conditions for the UP resin samples were selected for inverse analysis and validation modeling.

2.4 ThermaKin

To develop an accurate model for the pyrolysis of a material, it was necessary to couple an understanding of the physical, chemical, and thermal processes occurring during pyrolysis with an appropriate numerical pyrolysis solver. In this investigation the ThermaKin modeling environment was employed to parameterize the material properties by simulating experimental conditions in milligram-scale and bench-scale experiments and by predicting the mass loss rate during radiation-driven gasification experiments. ThermaKin has previously been successful in simulating the pyrolysis of noncharring and charring polymers in radiation-driven gasification experiments [9] [24] [7] [25].

ThermaKin is a two-dimensional comprehensive pyrolysis model that solves the transient energy and mass conservation equations to compute the rate of gaseous fuel production [1] [26]. The expression for the conservation of mass for each component, denoted by the subscript j, is given in Equation 3. In this expression ξ is the concentration of the individual species, t is time, θ is the stoichiometric coefficient, r is the rate of consumption or production from the chemical reaction, J is the flux of the gas flow within the solid, ρ is the density, and x is the Cartesian coordinate. The term on the right hand side of the expression accounts for the expansion or contraction of the material.

$$\frac{\delta \xi_j}{\delta t} = \sum_{i=1}^{Nr} \theta_i^j r_i - \frac{\delta J_j}{\delta x} + \frac{\delta}{\delta x}\left(\xi_j \int_0^x \frac{1}{\rho} \frac{\delta \rho}{\delta t} dx \right) \tag{3}$$

The chemical reactions are described using finite-rate chemical kinetics that are governed by the Arrhenius model, as shown in Equation 4. In this expression E_a is the activation energy, A is the pre-exponential factor, R is the molar gas constant, and T is the temperature. This model was selected for the chemical kinetics because it is the only model whose foundation is based on a reliable principal: statistical thermodynamics [1].

$$r_i = A_i exp\left(\frac{-E}{RT}\right) \xi_k \xi_l \tag{4}$$

The reaction is prescribed in the model through the balanced equation, as shown in Equation 5. In this expression h is the heat of reaction and COMP is an arbitrary placeholder for the user defined specie. The stoichiometric coefficient is defined as an input for each reaction specie. The heat of reaction may be defined using a temperature dependency. The initiation or termination of a reaction may be specified using upper or lower temperature bounds.

$$\theta_1 COMP1 + \theta_2 COMP2 \rightarrow \theta_3 COMP3 + \theta_4 COMP4 + h \qquad (5)$$

The flux of the gas flow within the solid is given by Equation 6 where, λ is the gas transfer coefficient.

$$J_g = -\rho_g \lambda \frac{\delta(\xi_g/\rho_g)}{\delta x} \qquad (6)$$

The expression for the conservation of energy is given by Equation 7. In this expression c is the specific heat capacity, q is the heat flux due to conduction, I_{ex} is the absorption of a radiant external heat flux, and I_{rr} is the re-radiation from the surface of the sample. The sixth term (i.e., seconds from the right) accounts for the convective heat transfer from the gaseous component and the seventh term (i.e., last one on the right) accounts for the expansion or contraction of the material. Heat transfer is assumed to occur instantaneously between the gas and solid phase.

$$\sum_{j=1}^{N} \xi_j c_j \frac{\delta T}{\delta t} = -\sum_{i=1}^{Nr} h_i r_i - \frac{\delta q}{\delta x} - \frac{\delta I_{ex}}{\delta x} + \frac{\delta I_{rr}}{\delta x} - \sum_{g=1}^{N_g} c_g J_g \frac{\delta T}{\delta x} + c_g \frac{\delta T}{\delta x} \int_0^x \frac{1}{\rho} \frac{\delta \rho}{\delta t} dx \qquad (7)$$

The heat flux resulting from conduction through the sample is given by Equation 8, where k is the thermal conductivity.

$$q = -k \frac{\delta T}{\delta x} \qquad (8)$$

The absorption of a radiant thermal heat flux is given by Equation 9, where α is the broadband radiation absorption coefficient.

$$\frac{\delta I_{ex}}{\delta x} = -I_{ex} \sum_{j=1}^{N} \alpha_j \, \xi_j \qquad (9)$$

The re-radiation from the surface of the sample to the environment is given by Equation 10 where I_{ex}^0 is the transmitted radiation across the boundary of the material and ε is the emissivity.

$$\frac{\delta I_{rr}}{\delta x} = \frac{\varepsilon \sigma T^4}{I_{ex}^0} \frac{\delta I_{ex}}{\delta x} \tag{10}$$

The composition of the material is specified as a mass fraction of the user-defined species. The density of the composite is evaluated in ThermaKin using the following expression, where mf is the mass fraction of individual species, γ is the swelling factor, and the subscripts s, l, and g denote the solid, liquid, and gaseous phases, respectively.

$$\frac{1}{\rho} = \sum_{s=1}^{N_s} \frac{mf_s}{\rho_s} + \sum_{l=1}^{N_l} \frac{mf_l}{\rho_l} + \gamma \sum_{g=1}^{N_g} \frac{mf_g}{\rho_g} \tag{11}$$

The specific heat capacity of the material is calculated using the following expression.

$$c = \sum_{i=1}^{N} mf_i c_i \tag{12}$$

The emissivity and absorption coefficient are specified as constant values for individual components and computed for a mixture through appropriate averaging. The other properties (i.e., density, thermal conductivity, specific heat capacity, and gas transport coefficient) may be described as temperature dependent in the following form, where the units are always taken as Kelvin.

$$p(T) = \ p_0 + p_1 T + p_n T^n \tag{13}$$

The thermal conductivity and gas transport coefficient are dependent on the relative amount and orientation of the components. For a material whose layers are in the direction normal to the flow of heat, the following expression is used for both properties where v_i is the volume fraction of each species. This expression describes the effective resistance to the process as a combination of the constituents acting in series.

$$k_n = \frac{1}{\sum_{i=1}^{N} \frac{v_i}{k_i}} \tag{14}$$

For a material whose layers are parallel to the direction of the flow of heat, the effective resistance is described as such using following expression.

$$k_p = \sum_{i=1}^{N} v_i k_i \tag{15}$$

Equation 16 is used to weight the effective thermal conductivity between the two orientations where β is a user-defined input value for the material on the range from zero to one with a default value of 0.5.

$$k = \beta k_p + (1 - \beta) k_n \tag{16}$$

The ThermaKin framework requires the user to specify the material properties and the boundary conditions to describe the mass transport, the ambient temperature, the convective heat transfer coefficient, and the radiative heat flux to the surface. The ambient temperature can be described using a linear time dependency. Radiative heat transfer is specified by the external heat flux at the boundary, which can contain up to two linear phases and may be repeated. Conditions to account for ignition and flame stabilization on the surface of the sample may also be specified.

ThermaKin divides the material into finite elements and uses a modified Crank-Nicolson scheme to calculate the temperature and concentration of constituents for each element at every time step.

2.4.1 Milligram-Scale Modeling

The heating program was specified to model the heat transfer processes and conditions present during experimental testing. The initial temperature of the sample was set to 313 K. The temperature of the ambient gases at the top surface was specified initially as 313 K. The heating rate was specified as a boundary condition input in to the model based on the experimental measurement. The true heating rate was calculated from the two independent measurements, temperature and time, shown in Figure 16.

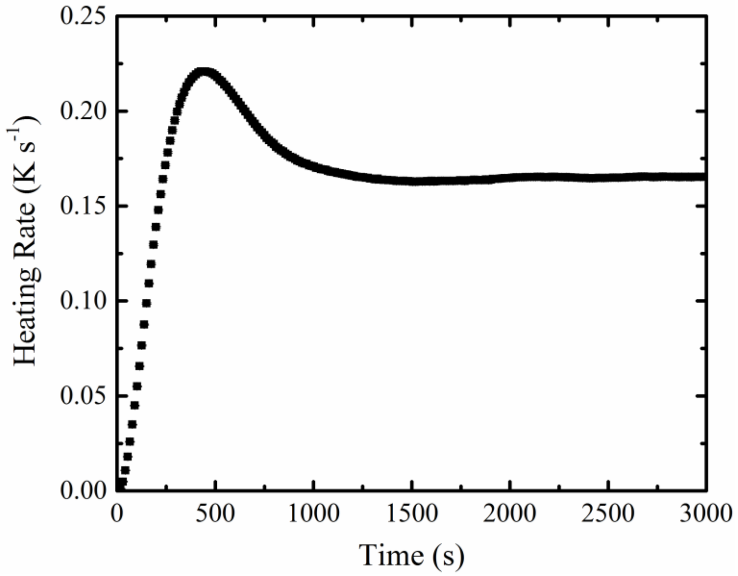

Figure 16. True heating rate measured from TGA/DSC testing.

The error was calculated as two standard deviations of the mean, which was small enough that the error bars were not discernable from the data points. The true heating rate was fit with a time-dependent equation to accurately model the heat transfer processes during milligram-scale testing, given by Equation 17.

$$\frac{dT}{dt} = 0.1667\left[1 - \left(e^{-0.002258\times t}(cos(0.004515t) - 0.4338\sin(0.004515t))\right)\right] \quad (17)$$

Figure 17 shows the agreement between the expression input to the model simulation and the measured heating rate.

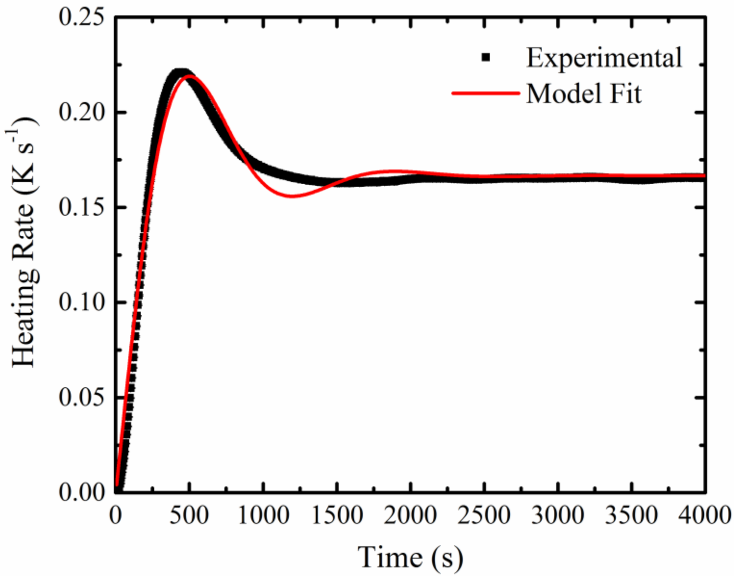

Figure 17. Agreement between the true heating rate and the fit for modeling the variable heating rate.

The convective heat transfer coefficient was set to 10^5 W m^{-2}K^{-1} to ensure that the sample would almost exactly follow the prescribed temperature program. The thickness of the sample was specified as 0.05 mm to ensure that the material would behave thermally thin. The top boundary specified the transport of gaseous products of decomposition from the condensed phase to occur at a linear rate, defined to effectively remove the gaseous volatiles instantaneously upon formation. The bottom boundary was declared such that no mass transport would occur across the surface. The element size was specified as 0.005 mm with a 0.01 time step. A sensitivity analysis showed that varying the integration parameters by a factor of 2 did not produce significant changes in the results.

The mass data from the TGA was used to determine the stoichiometric coefficients and the Arrhenius rate reaction parameters in the effective reaction mechanism for the thermal degradation of the resin. The heat flow data from the DSC was analyzed to determine the heat capacities of the model constituents, the heats of decomposition, and the heat of gasification. The heat flow data from the DSC tests on the char were analyzed to independently determine the heat capacity.

2.4.2 Modeling Gasification Experiments

The heat program was input to the model as the thermal boundary conditions, which were specified to simulate the conditions during radiation-driven gasification experiments. The external radiant exposure at the top boundary was defined as the steady value for the testing conditions of interest, which were calibrated with a Schmidt-Boelter heat flux gauge. The radiative heat flux at the bottom surface was set to the steady value of 0.5 kW m^{-2} for all three radiant heater set points.

Convective heat transfer at the boundaries was described by the temperature of the ambient gases at the sample surface and the convective heat transfer coefficients, which were quantified in a previous investigation [8]. A copper plate with well-defined thermodynamic properties was exposed to a steady heat flux under the truncated cone heater. The temperature of the bottom surface was monitored using the IR camera. This data was used as a target for inverse analysis to determine the characteristics of the convective flow necessary to replicate the measured temperature profiles. The convective heat transfer coefficient at the top surface of the sample was found to be well represented by 5 W $m^{-2}K^{-1}$. The temperature of the ambient gases at the top surface was found to be 330 K at 30 kW m^{-2}, 350 K at 50 kW m^{-2}, and 370 K at 70 kW m^{-2}. The convective heat transfer coefficient at the bottom surface of the sample was determined to be 4 W $m^{-2}K^{-1}$. The temperature of the ambient gases at the bottom surface was represented well by 310 K for the range of experimental heat fluxes.

The gas transport coefficient was set to 2 x 10^{-5} m^2 s^{-1} for all components, to remove the gaseous products of decomposition from the condensed phase upon formation. The heat capacity of the gaseous products of decomposition was assumed to be 1.8 kJ $kg^{-1}K^{-1}$, based on a previous investigation to determine the heat capacity of C1-C8 hydrocarbons at 400-500 K [27]. The time step was set to 0.01 seconds. A sensitivity analysis showed that varying the integration parameters by a factor of two did not produce significant variation in the results.

The composite was described as a homogeneous mixture of the individual components in the model. However, there were important physical processes occurring in the condensed phase of the composite where the material properties did not behave as a homogeneous mixture, but rather as layers on distinct species, notably the thermal conductivity. The values for the thermal conductivity of reinforcing fibers in a polymer composite have typically been reported being order(s) of magnitude greater than their polymer counterparts [10]. The reinforcing fibers will exhibit anisotropic behavior providing for transfer heat via lateral conduction along the through-plane direction when exposed to an external heat flux. The thermal conductivity of the composite was modeled as alternating, uniform layers oriented normally to the flow of heat by adjusting the model parameter β for the parallel conductivity from the initial value of 0.5 to 0.

The composition and thickness of the sample for each configuration was specified from the experimental measurements. The compositions were reported in Table 3.

Table 3. Composition ration calculated based on average sample measurements for each individual configuration (wt% resin).

Average Composition Ratio (wt% resin)	Heat Flux (kW m^{-2}) 70	 50	 30
41	41.3 ±0.24	40.9 ±0.41	41.1 ±0.60
48	48.3 ±1.1	48.0 ±0.78	47.7 ±0.90
54	53.5 ±0.27	53.3 ±1.32	56.0 ±2.23

The average thickness for each configuration were reported in Table 4.

Table 4. Average thickness based on measurements for each configuration (mm).

Average Composition Ratio (wt% resin)	Heat Flux (kW m^{-2}) 70	 50	 30
41	5.6 ±0.00	5.5 ±0.07	5.6 ±0.60
48	6.3 ±0.12	6.1 ±0.12	6.3 ±0.08
54	6.7 ±0.06	6.7 ±0.24	7.4 ±0.71

The values for each configuration were specified based on the individual test measurements. When the large composite samples were removed from the mold and machined to prepare individual samples it was observed that there were slight variation in the thickness between samples of the same composition. During experimental testing the composite samples with similar thicknesses were tested together. Sample selection was performed this way to reduce the variability between the individual testes where the experimental data would ultimately be combined and to provide a set of similar sample measurements for modeling.

3. Results and Discussion

3.1 Milligram Scale

Analysis of milligram-scale experiments were used to characterize the semi-global degradation reaction mechanism and the thermodynamic properties of the initial material and decomposition species. The stoichiometric coefficients and Arrhenius rate reaction parameters were determined from TGA. The apparent heat capacity measured by DSC was used to quantify the sensible heat and latent heat in order to characterize the specific heat capacities and heats of reaction.

3.1.1 Thermogravimetric Analysis

3.1.1.1 Experimental Results

TGA provided the instantaneous mass of the pure resin sample in 6-second increments during the prescribed linear heating rate of 10 K min^{-1} in an anaerobic environment. The results of interest were the normalized total mass and mass loss rate as a function of the sample temperature. The experimental procedure was repeated 7 times to ensure adequate agreement between the numerical results. The normalized mass, shown in Figure 18, was calculated as the statistical mean for the set of experimental data.

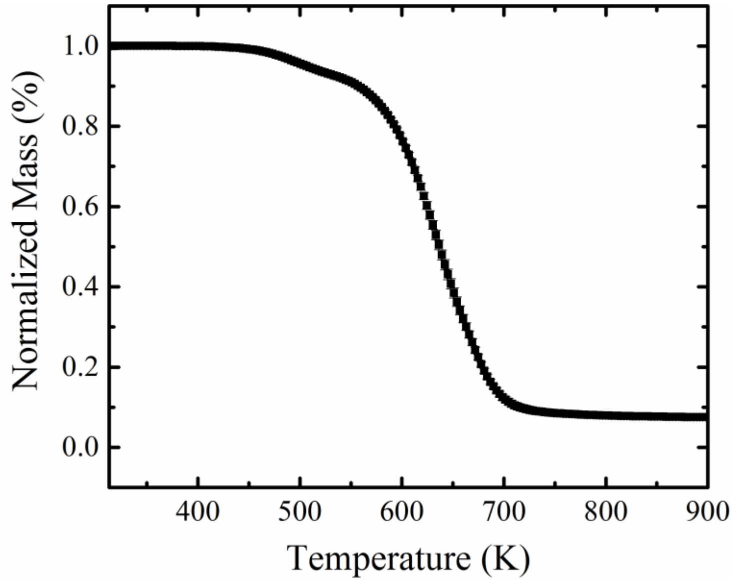

Figure 18. Average normalized mass of the resin measured from TGA.

The error was calculated as two standard deviations of the mean. The resulting errors were included in Figure 18, but the values were small enough that they could not be discerned from the data points.

The normalized mass loss rate, shown in Figure 19, was the change in mass over the discrete time step from the average normalized mass.

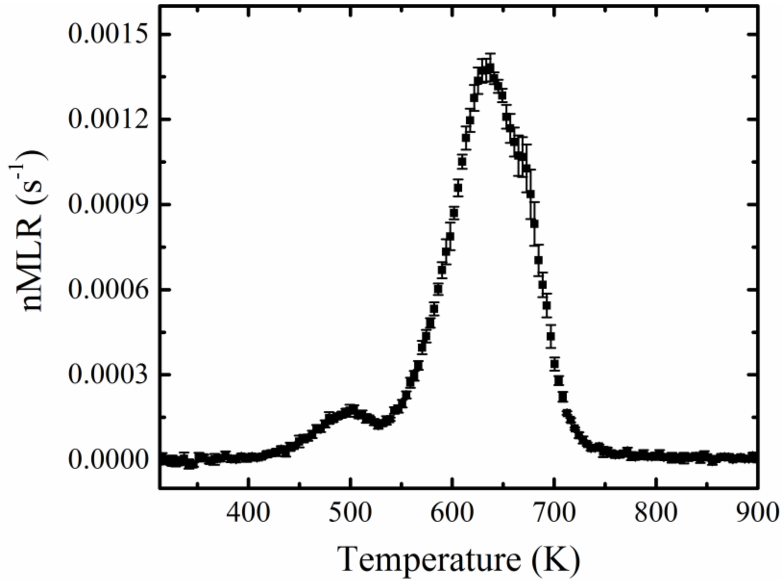

Figure 19. Average normalized mass loss rate calculated from TGA.

The error was calculated as two standard deviations of the mean. These measurements were utilized to determine the Arrhenius rate reaction parameters and the stoichiometric coefficients for the degradation mechanism to describe the effective kinetic model. The purpose of this analysis was to describe the kinetics of decomposition using as few first-order Arrhenius rate reactions as possible to simultaneously optimize the mass and mass loss rate from experimental testing as the target data sets. The mass loss rate was analyzed to determine the number of reactions necessary to describe the semi-global reaction mechanism.

A first reaction was observed to occur over a temperature range from 390-530K. The temperature identified for the upper bound of the reaction was the temperature where the local minimum indicates the transition from the first reaction to the second reaction, not the absolute temperature where the first reaction ceases. The second process was observed to occur over a temperature range from 530-700K. The majority of the mass loss occurs during this second reaction. A third reaction was identified to occur over a temperature range from 630-760 K. The mass of the remaining char was analyzed at the end of the heating program and it was determined that seven percent of the initial mass remained. The three identified reactions were described using consecutive first-order reactions to describe the degradation process.

The individual tests had the same qualitative shape, particularly the location of the reactions with respect to temperature. There was some variation in the individual tests between the maximum normalized mass loss rates in the second reaction and the third reaction. A larger peak value for the normalized mass loss rate during the second reaction corresponded to a smaller peak value for the normalized mass loss rate during the third reaction.

3.1.1.2 Global Reaction Mechanism

An apparent reaction mechanism consisting of three consecutive first-order reactions was developed to describe the degradation of the unsaturated polyester resin, as shown in Equation 18-20.

$$Virgin\ Resin\ \rightarrow\ \theta_1 Intermediate\ 1 + (1 - \theta_1)\ gas \tag{18}$$

$$Intermediate\ 1\ \rightarrow\ \theta_2\ Intermediate\ 2 + (1 - \theta_2)\ gas \tag{19}$$

$$Intermediate\ 2\ \rightarrow\ \theta_3\ Char + (1 - \theta_3)\ gas \tag{20}$$

The virgin resin decomposed to form an intermediate and a gas species, as shown in Equation 18. The first intermediate decomposed to yield a second intermediate and a gas species, as shown in Equation 19. The second intermediate reacted and produced the char and a gas species, as shown in Equation 20.

The stoichiometric coefficients were determined directly from the TGA data. The normalized mass loss was taken at the temperature corresponding to the local minimum in the normalized mass loss rate during the transition between each reaction. The stoichiometric coefficient was specified as the normalized mass loss relative to the portion of remaining material in the condensed phase from the previous reaction(s), as shown in Equations 21-23.

$$\theta_1 = \frac{m_1}{m_i} \tag{21}$$

$$\theta_2 = \frac{m_2}{\theta_1 m_i} \tag{22}$$

$$\theta_3 = \frac{m_3}{\theta_1 \theta_2 m_i} \tag{23}$$

The term m_i was the initial mass of the sample and subscripts 1-3 corresponded to the mass remaining at the end of each respective reaction.

For a single-step first-order Arrhenius rate reaction, the mass loss rate would be determined from Equation 24, where A is the pre-exponential factor (sec^{-1}), E_a is the activation energy (J mol^{-1}), R is the universal gas constant, ξ is the concentration of the species, and dm dt^{-1} is the rate of change of mass of the sample.

$$\frac{dm}{dt} = A\, exp\left(\frac{-E_a}{RT}\right)\xi \tag{24}$$

An approximate solution for the first-order reaction under linear heating conditions is shown in Equations 25 and 26. The subscript *max* denotes the local maximum for the reaction. m_0 is the initial mass of the reactant when the reaction occurs, which accounts for the conversion factor from any previous reactions [7].

$$E_a = \frac{eRT_{max}^2 \dfrac{{}^{dm}\!/_{dt_{max}}}{m_0}}{(1-\theta)\dfrac{dT}{dt}} \tag{25}$$

$$A = \frac{e\, {}^{dm}\!/_{dt_{max}}}{m_0} e^{E/_{RT_{max}}} \tag{26}$$

The process was complicated by the presence of not one, but three consecutive reactions. The equations described above were used as a first-order approximation during analysis. Inverse analysis was used to evaluate the activation energy and pre-exponential factors for the three reactions with the normalized mass loss rate as the optimization target. The first reaction was isolated, and the above expressions were used to initially quantify the parameters. The local maximum occurred at 500 K, and the corresponding values for the normalized mass loss rate and normalized mass were taken at this reference point. The parameters were refined by making minor adjustments to the values, evaluating the inputs in the comprehensive pyrolysis model, and comparing the results to the optimization target. The target for the curve fitting was the location of the initial increase and the maximum value of the normalized mass loss rate at the local maximum. The parameters for each reaction in the effective degradation mechanism are shown in Table 5.

Table 5. Effective reaction mechanism for degradation of polyester resin.

Reaction	Equation	A (sec^{-1})	E_a ($J\ mol^{-1}$)
1	Virgin Resin → 0.935 Intermediate1+ 0.065 Gas	$8.3x10^5$	$7.7x10^4$
2	Intermediate 1 → 0.292 Intermediate2 + 0.708 Gas	$4.99x10^5$	$9.7x10^4$
3	Intermediate 2 → 0.282 Char + 0.718 Gas	$6.2x10^8$	$1.45x10^5$

Once the first reaction was satisfactorily characterized, the second reaction was added and the refinement process was repeated. The local maximum was taken at 633 K. The reactions were described as occurring in series, meaning that the products from one reaction became the reactants for the following reaction. Thus, the addition of each new reaction introduced a competing process to the system and caused the other reactions to shift both the temperature at which the relative peak mass loss occurred and the width of the distribution of mass loss around the corresponding temperature. The first and second reactions occur at notably different temperatures, and the resulting shift was not significant. However, the second and third reactions occur at similar temperatures, which presented a challenge for the fitting process. The target for fitting the second reaction was the increase in normalized mass loss rate from the first to the second reaction, the location of the peak at 633 K, and the magnitude of the peak.

The reaction parameters were adequately characterized, and the third reaction was added to the system. The local maximum for the reaction occurred at 670 K, partially simultaneously with the second reaction. The targets for the fitting process were the decay along the tail of the degradation reaction, and the location and magnitude of the relative peak. Once all of the reactions were included, the parameters were further refined to the TGA data. Figure 20 shows the normalized mass as a function of temperature for the parameterized model and the experimental data.

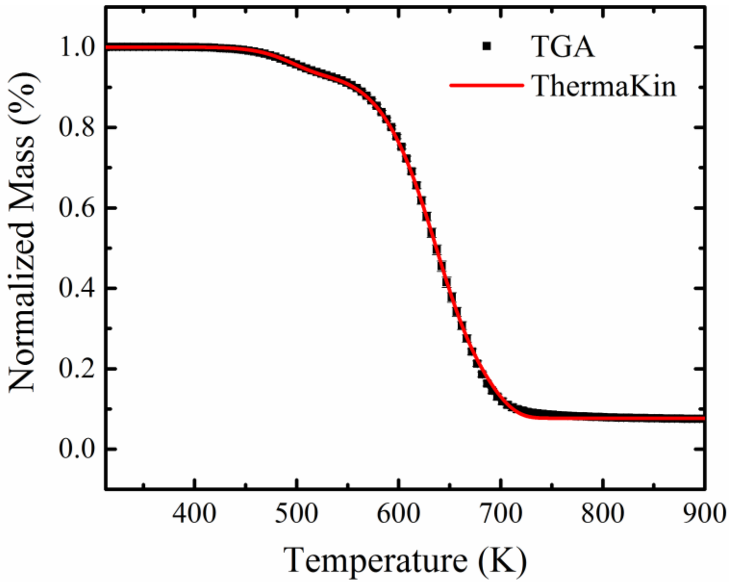

Figure 20. Agreement between the normalized mass from the simulation and the experimental results.

Figure 21 shows the agreement between the kinetic model and the experimental data, and Table 5, presented earlier, gives the optimized stoichiometric coefficients and Arrhenius rate reaction parameters.

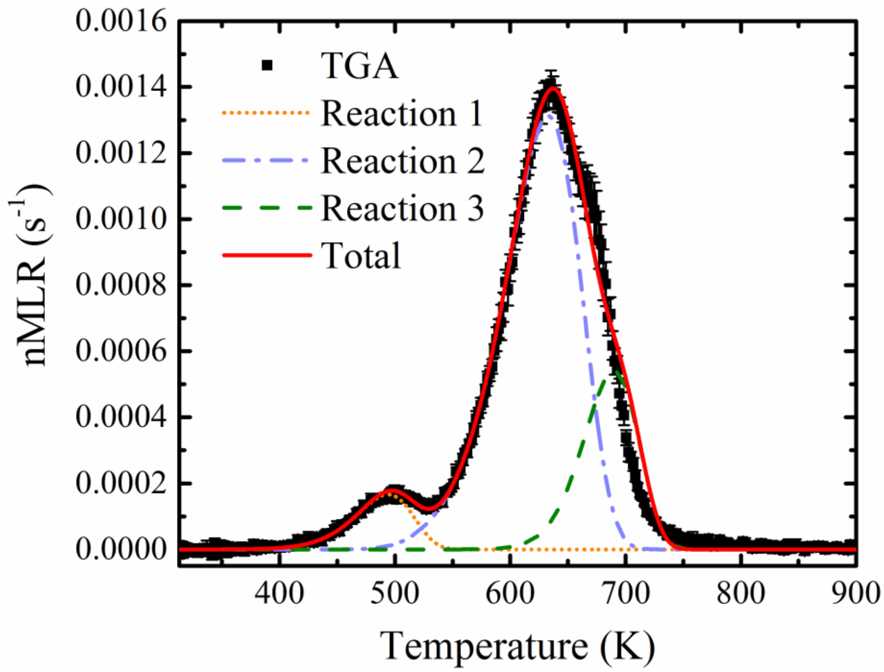

Figure 21. Normalized mass loss rate from simulation showing contribution of individual reactions with data.

The stoichiometric coefficients determined the mass lost during each reaction and the Arrhenius rate reaction parameters determined the temperature range the reaction will occur over. The smallest amount of mass was lost during the first reaction, which occurred at relatively low temperatures and occurred over a temperature range of approximately 100 K. The majority of the mass was lost during the second reaction, which occurred over a temperature range of approximately 200 K. The final reaction corresponded was greater than that in the first reaction, but less than the third reaction and occurred over a temperature range of approximately 150 K. The model prediction from the parameterized reaction mechanism agrees well with both experimentally determined temperature-dependent profiles.

3.1.2 Differential Scanning Calorimetry

The primary measurement from DSC was the heat flow rate as a function of time and sample temperature. For this investigation, the adopted sign convention will assume a positive value of the heat flow rate for an endothermic process and a negative value of the heat flow rate for an exothermic process.

3.1.2.1 Glass Transition Temperature

The complete cure of the resin was desirable prior to experimental testing to prevent variations in the heat flow rate measurement as a result of the glass transition. In order to complete the polymerization process in the resin, an oven post-cure at the glass transition temperature was included in the fabrication process. Preliminary DSC measurements were performed to determine the temperature for the oven post-cure. Figure 22 shows the heat flow rate for the resin without post-processing during the fabrication of the sample.

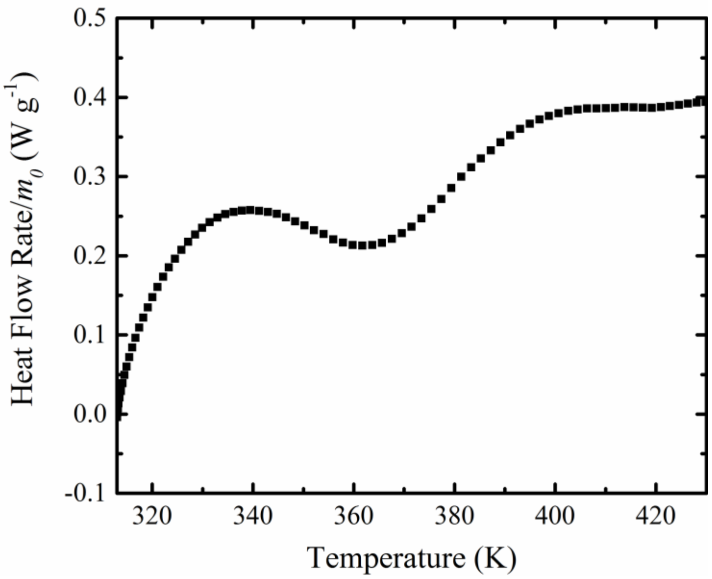

Figure 22. DSC measurement of heat flow rate to the resin sample to determine the oven post-cure temperature.

A feature was observed along the curve between 330 and 400 K. The TGA showed that the onset of mass loss did not occur until 400 K, which indicated that the feature was the result of a transition in the sample causing a change in the sensible enthalpy. The during the glass transition the material properties (e.g., the specific heat capacity and coefficient of thermal expansion) of the UP resin undergo dramatic changes as the polymer matrix transitions from a rigid, brittle structure to a rubber-like state. The extrapolated onset temperature of the glass transition was identified as approximately 343 K, which was selected as the temperature for the oven post-cure.

3.1.2.2 Polyester Resin Experimental Data

Figure 23 shows the average heat flow rate measurement for seven tests at the specified heating rate of 10 K min^{-1} in an anaerobic environment.

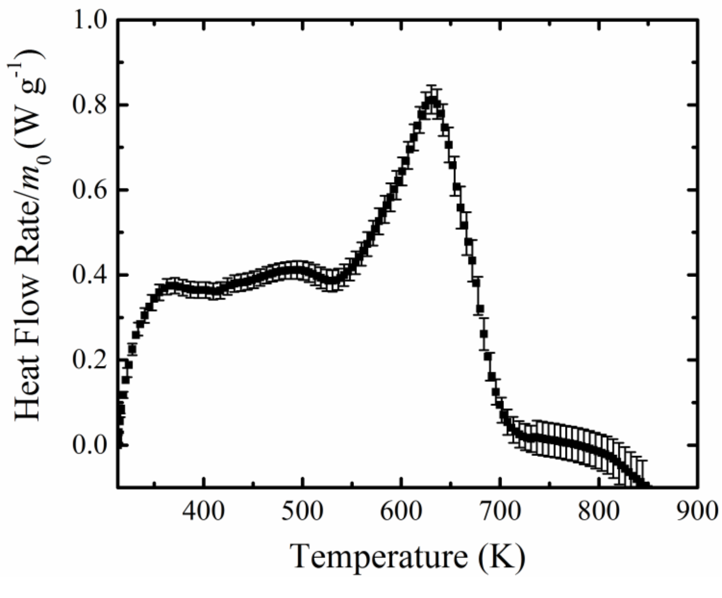

Figure 23. DSC measurement of the heat flow rate as a function of time for the oven-cured polyester resin.

The error was calculated as two standard deviations of the mean. The degradation process was endothermic for the first 3000 seconds, which corresponded to a temperature of 810 K. At higher temperatures the measured heat flow rate indicated an exothermic process where, according to the TGA, no mass loss occurred. The reduction in the accuracy of the heat flow rate measurement was previously shown to occur at these elevated temperatures. This apparent exothermic region was assumed to be a product of systematic error rather than indicative of the degradation processes occurring within the resin.

The apparent heat capacity of the resin was determined by dividing the heat flow rate to the sample by the true heating rate. This value was used to describe the amount of energy per unit mass required to increase the temperature of the sample, which was a combination of the sensible enthalpy and the enthalpy of reaction. The kinetic model was used to generate a baseline for the specific heat capacity, which was necessary to quantify the heats of decomposition.

Figure 24 shows the heat flow rate to the sample integrated with respect to time. The heat of gasification was determined from the total of the integral.

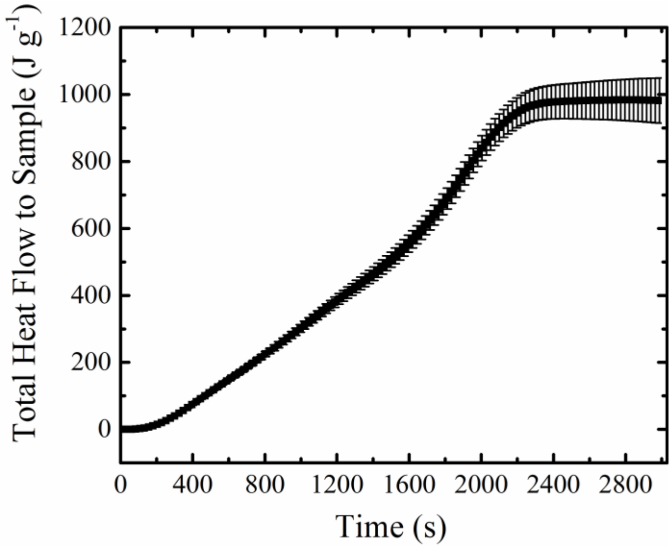

Figure 24. Temperature dependent heat of gasification calculated from the heat flow rate measurement.

The error was calculated as two standard deviations of the mean. The total heat flow to the sample was an important value against which to check the parameterized model in order to ensure that the reaction mechanism was representative of the material behavior. The total energy required for heating and degrading the sample observed in the experiments was evaluated for agreement with the model simulation after the thermodynamic properties were characterized from DSC measurements.

3.1.2.3 Specific Heat Capacity

The apparent heat capacity was calculated from the experimental data by dividing the heat flow to the sample by the true heating rate, as shown in Figure 25.

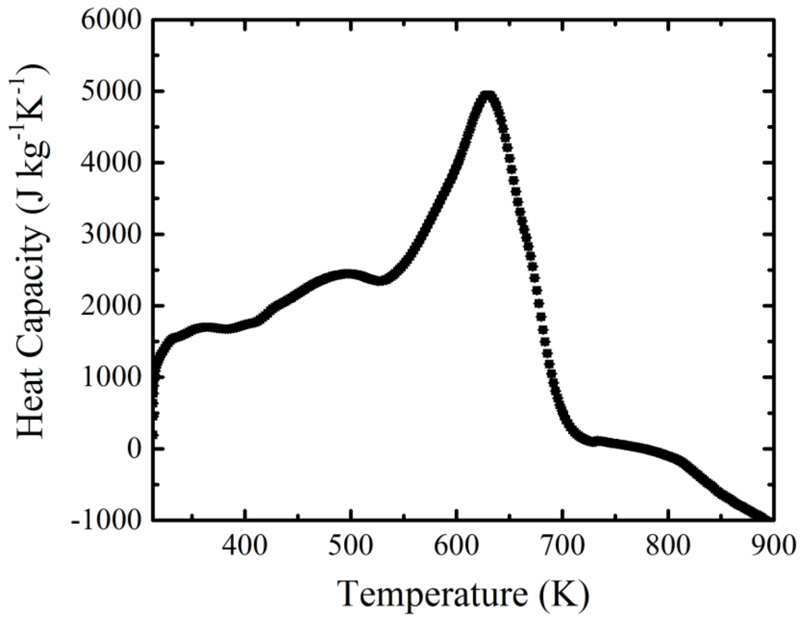

Figure 25. Apparent specific heat capacity calculated from DSC measurements.

The error was calculated as two standard deviations of the mean. The values were small enough that the error bars could not be discerned from the data points. A baseline for the specific heat capacity was developed in order to quantify the energy attributed to the heats of decomposition. The STA was run at constant pressure so the baseline could be expressed by the enthalpy, given in Equation 27.

$$H_{baseline}(t) = \frac{1}{m_i}\frac{dT}{dt}\sum_{i=1}^{N} c_j(T)m_j(t) \tag{27}$$

The apparent heat capacity, shown in Figure 25, had a feature along the temperature range from 313 – 339 K corresponding to a 70% increase in the value calculated from measurement. An initial analysis was performed using the variable heating rate and the measurement was determined not to be a result of the experimental conditions. The material behavior was captured by describing the virgin resin using two specific heat capacities with a temperature dependent transition. The first reaction that was previously characterized was replaced with three subroutines. The complete set of reactions and kinetic parameters can be found in Table 6.

Table 6. Effective degradation reaction mechanism with piece-wise subroutine.

Reaction	Equation	A (sec^{-1})	E_a ($J\ mol^{-1}$)
1a	Virgin Resin → Virgin Resin 1	1	0
1b	Virgin Resin → 0.935 Intermediate 1+ 0.065 Gas	$8.3\text{x}10^5$	$7.7\text{x}10^4$
1c	Virgin Resin 1 →0.935 Intermediate 1+0.065 Gas	$8.3\text{x}10^5$	$7.7\text{x}10^4$
2	Intermediate 1 →0.292 Intermediate 2+0.708 Gas	$4.99\text{x}10^5$	$9.7\text{x}10^4$
3	Intermediate 2 → 0.282 Char + 0.718 Gas	$6.2\text{x}10^8$	$1.45\text{x}10^5$

The first reaction was characterized using a lower temperature limit of 339.2 K. The specific heat capacity of the initial specie (i.e., virgin resin) was described by fitting the feature in the apparent heat capacity curve with a temperature dependent quadratic expression, as shown in Figure 26.

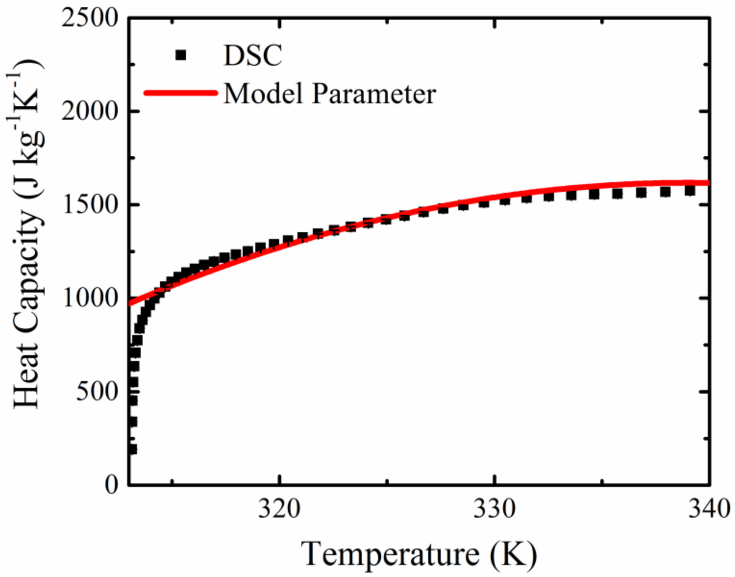

Figure 26. Second order polynomial fit for the initial rise in heat capacity of the virgin UP resin.

When the temperature reached the lower limit, the virgin resin would instantaneously become virgin resin 1. This reaction (i.e., 2c) had the same parameters previously determined for the first reaction. The reaction identified as 1b had the same Arrhenius rate reaction parameters as the initial reaction to ensure that the model captured any initial mass loss below the lower temperature limit.

The specific heat capacity of the intermediate virgin material and the first intermediate were specified assuming a linear temperature dependency from 1619.9 J kg^{-1}K^{-1}, at the reaction transition temperature (339.2 K), to 2035.9 J kg^{-1}K^{-1}, at the local minimum between the first and second reaction (523 K). This assumption agreed well with previous investigations [12] [6] which showed that the specific heat capacity increased linearly as a function of temperature. The specific heat capacity of second intermediate could not be distinguished from the heat of reaction in the apparent heat capacity measurement. This specie would require a value to be assumed based on the specific heat capacities of the relative decomposition species.

The specific heat capacity of the char was determined through a separate set of experimental measurements. When the DSC experiments were performed on the UP resin there was less than 10% of the initial mass present when the char was formed. This relative decay in sample mass indicated a loss of thermal contact between the sample and crucible, which was necessary for the accuracy of this test method. This loss of thermal contact was coupled with the decreased sensitivity of the apparatus at these elevated temperatures. Additional DSC experiments were performed using char harvested from gasification testing of UP resin samples at 70 kW m^{-2} in order to obtain a reliable and accurate experimental measurement for the char. A thorough presentation of the milligrams-scale experiments performed on the char is provided in Appendix II. The apparent heat capacity of the char, shown in Figure 27, was calculated by dividing the heat flow to the sample by the true heating rate.

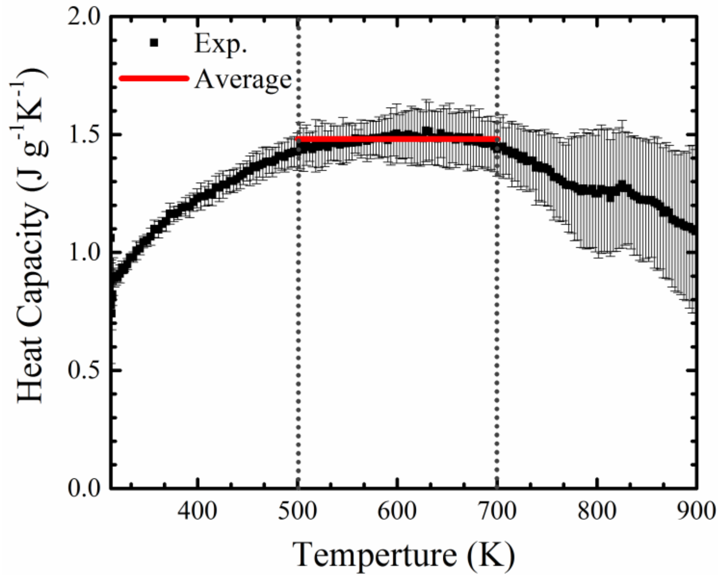

Figure 27. Apparent specific heat capacity of the char as a function of temperature.

The char was assumed to be nonreactive in a non-oxidizing atmosphere, and the specific heat capacity was taken as the average apparent heat capacity over a temperature range from 500-700 K. Based on this methodology, the specific heat capacity of the char was found to be 1480 J $kg^{-1}K^{-1}$. The specific heat capacity of the second intermediate was declared as 1760 J $kg^{-1}K^{-1}$, the average between the final char and the first intermediate at 523 K.

DSC testing was conducted on the glass fibers in an effort to experimentally determine the specific heat capacity. The results from numerous iterations showed significant scatter in the experimental data; consequently, the data could not be employed meaningfully. This outcome was probably due to the structure of the fibers and the thermal contact between the fibers and the crucible. Subsequently, well-defined literature values were used to determine the property value. The specific heat capacity of E-glass was reported as 810 J $kg^{-1}K^{-1}$ at 296 K and 1030 J $kg^{-1}K^{-1}$ at 473 K [20]. A linear, temperature-dependent relationship was assumed, which resulted in the following expression, where the temperature is in K.

$$c_p = 440 + 1.24\,T \quad (J\,kg^{-1}K^{-1}) \tag{28}$$

The values of the specific heat capacity for all of the UP resin species are provided in Table 7 and are shown in Figure 28.

Table 7. Specific heat capacity of constituent species.

Species	Specific Heat Capacity (J $kg^{-1}K^{-1}$)
Virgin Resin	$-108136 + 647.5\,T - 0.995\,T^2$
Virgin Resin 1	$843.5 + 2.28 \times T$
Intermediate 1	$843.5 + 2.28 \times T$
Intermediate 2	1760
Char	1480
Fiberglass	$440 + 1.24\,T$

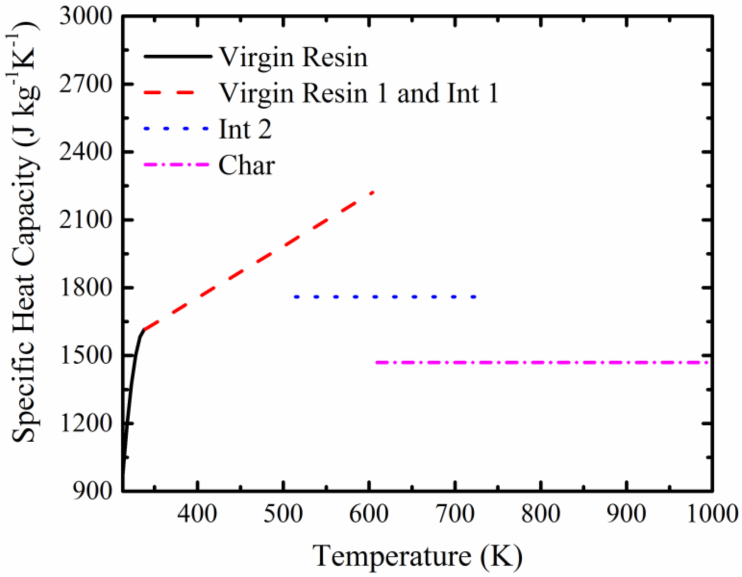

Figure 28. Specific heat capacity of individual species over the temperature range each is present.

The baseline and experimental data for the specific heat capacity as a function of temperature are shown in Figure 29.

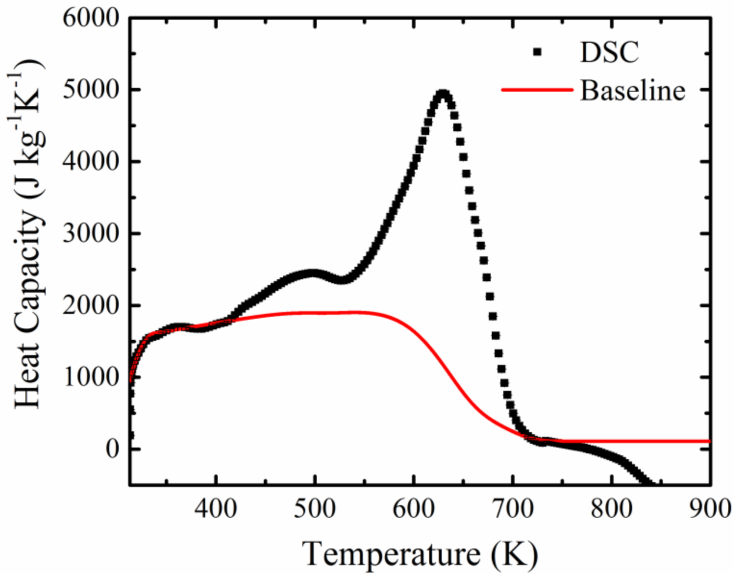

Figure 29. Baseline for the energy required to heat the sample through the specified heat profile as a function of temperature.

The polynomial fit for the initial period agreed well with the experimental data. The baseline increased linearly for the first two reactions. The heat capacity then declined quickly from 600-700 K as the baseline approached the heat capacity of the final char. At higher temperatures the tail of the experimental measurement decayed as the sensitivity of the apparatus declined. The area between the baseline and the measured heat flow rate curve was used to determine the heats of degradation for the reaction mechanism.

3.1.2.4 Heats of Degradation

The characterized reactions were all endothermic processes, which were quantified using the heat flow rate data from DSC. The experimental conditions were modeled in ThermaKin using the kinetic model and specific heat capacities previously identified to produce a baseline, as shown in Figure 29. This baseline was representative of the sensible enthalpy. The effective heats of reaction were defined as the integral between the experimental DSC heat flow rate and the baseline from ThermaKin, evaluated over the respective time interval for each reaction.

The baseline for the heat flow rate as a function of time is shown in Figure 30.

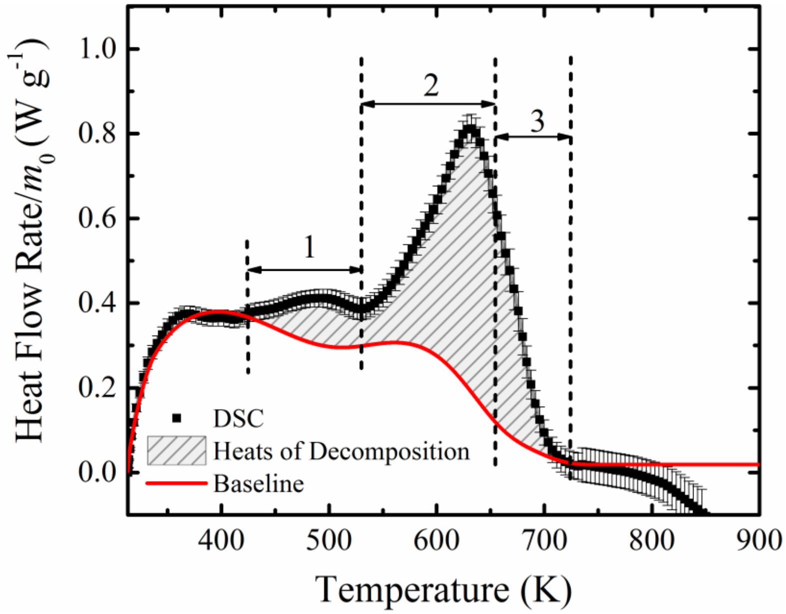

Figure 30. Energy evaluated for the heats of decomposition for the kinetic model.

When the baseline for the specific heat capacity was graphed as a function of temperature, shown earlier in Figure 29, the baseline increased linearly during the first reaction. However, when the heat flow rate was expressed as a function of time, there was a decay in the baseline during the first reaction.

The times for the integration parameters were determined from the values corresponding to the identified temperatures that bound the reactions. The first reaction was evaluated over the interval from 700 – 1300 seconds. The calculated effective heat of decomposition for the first reaction was -37 J g^{-1}. The second reaction was evaluated on the interval from 1300 – 2200 seconds, yielding a heat of decomposition of -314 J g^{-1}. The third reaction was evaluated on the interval from 2200 – 2800 seconds, resulting in a heat of decomposition of -24 J g^{-1}. The integrated value was calculated per unit of initial mass and was normalized for the fraction of the initial mass remaining at the beginning of each reaction. The heats of decomposition are given in Table 8.

Table 8. Heat of decompositions for each reaction in the mechanism.

Reaction	Equation	Heat of Reaction ($J\ kg^{-1}$)
1a	Virgin Resin → Virgin Resin 1	0
1b	Virgin Resin →0.935 Intermediate 1+0.065 Gas	0
1c	Virgin Resin 1 →0.935 Intermediate 1+0.065 Gas	-37000
2	Intermediate 1 →0.292 Intermediate 2+0.708 Gas	-336000
3	Intermediate 2 →0.282 Char+0.718 Gas	-184000

The agreement between the heat flow rate as a function of time and the characterized heats of decomposition is shown in Figure 31.

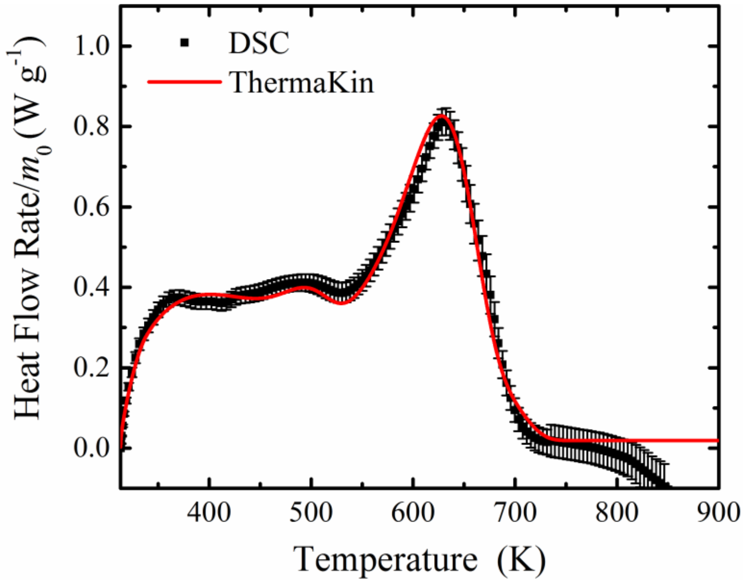

Figure 31. Agreement between the heat flow rate from the model simulation and experimental data.

The heat flow to the sample as a function of time is shown in Figure 32**.**

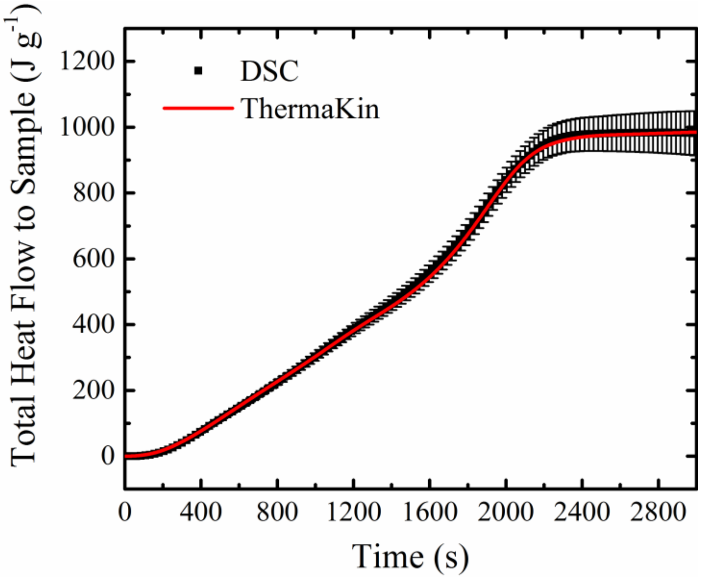

Figure 32. Total heat flow to the sample as a function of sample temperature for the model simulation and experimental data.

The total heat flow to the sample (i.e., heat of gasification) was calculated to be -987 J g^{-1}, and agreed well with the model simulation. The model prediction agreed well with the experimental results. The agreement was a result of the fitting process, which used the total heat flow to the sample as a target for inverse analysis when determining the heats of reaction.

3.2 Radiative Properties

The material properties necessary to characterize the radiative heat transfer included the radiative absorption coefficient and emissivity. Previous work has shown that the overall heat transfer process was of limited sensitivity to the radiative properties of a material [28]. An appropriate amount of consideration for these properties was determined to be a combination of simplified experimental testing and assumptions based on literature values. The absorption coefficient of the virgin resin was determined from experimental testing. The absorption coefficients of the other species were assumed based on literature values and the behavior of relative intermediate species. The emissivity of each species was specified from literature values.

3.2.1 Absorption Coefficient

The heat transfer process was assumed to be one-dimensional for the determination of the absorption coefficient for the UP resin. The in-depth radiation absorption was assumed to be wavelength-independent. The initial heat transfer measurement was evaluated when the UP resin sample was placed over the heat flux gauge and taken as a time average over the first five seconds of the thermal exposure. This time increment was selected to minimize the effects from in-depth heat conduction of the resin that would result in radiative feedback from the back surface of the sample to the heat flux gauge. Linteris used the initial heat flux measurement when the shutter was open for his analysis [29]. The calculated absorption coefficients were evaluated and found to produce similar results for both methods using Equation 29, which accounts for reflection at the interface**.** In the expression *r(0)* is the reflection loss coefficient, τ is the transmission coefficient, and *b* is the film thickness [30].

$$\alpha = \frac{2\ln\left(1 - \mathrm{r}(0)\right) - \ln(\tau)}{\mathrm{b}} \tag{29}$$

The average value for the three tests was 2.1 $\mathrm{m}^2\,\mathrm{kg}^{-1}$ with a variance of 2.2%. This value was taken as representative for the virgin UP resin. The final char was assumed to be effectively non-transparent and the absorption coefficient was taken as 100 $\mathrm{m}^2\,\mathrm{kg}^{-1}$ [8]**.** The absorption coefficients for the intermediate species were assumed to be equal to the virgin resin or the non-transparent final char. The absorption coefficient for the fiberglass was taken from literature as 100 $\mathrm{m}^2\,\mathrm{kg}^{-1}$ [31].

The absorption coefficient of the intermediate species were specified based on the behavior of the other species. The intermediates were assumed to be equal to the absorption coefficient of the virgin resin, the char, or the mean value. The parameters were evaluated as a fitting mechanism to reconcile discrepancies between the model and the experimental measurements. Table 9 shows the absorption coefficient for each species.

Table 9. Absorption coefficients of evolved species.

Species	Absorption Coefficient ($m^2\ kg^{-1}$)
Virgin Resin	2.1
Virgin Resin 1	2.1
Intermediate 1	2.1
Intermediate 2	100
Char	100
Fiberglass	100

3.2.2 Emissivity

The emissivity of each constituent specie was specified from literature. Table 10 shows the assumed emissivity for all of the species.

Table 10. Emissivity of evolved species.

Species	Emissivity
Virgin Resin	0.95
Virgin Resin 1	0.95
Intermediate 1	0.95
Intermediate 2	0.86
Char	0.86
Fiberglass	0.85

The emissivity of the UP resin and decomposition species were assumed to be 0.95 based on the work of Linteris, which showed that most polymers have an emissivity greater than 0.9 [23]. The emissivity of the char was assumed to be equal to that of graphite, 0.86, because of the inherently high carbon content of char [32]. The emissivity of the fiberglass was set as 0.85 based on literature values [31].

3.3 Gasification Experiments

Gasification experiments were conducted in a modified cone calorimeter equipped with the CAPA to purge the sample with nitrogen, creating a nearly anaerobic environment. The samples were tested at steady conditions for external heat fluxes of 30, 50, and 70 kW m^{-2}. UP resin was evaluated at 30 kW m^{-2} with a high emissivity paint on the top surface of the sample. Seven UP resin sample configurations were tested in triplicates. Fiberglass samples were fabricated at composition ratios of 41, 48, and 54 wt% resin. Every composition ratio was tested in triplicates for each external heat flux, resulting in nine fiberglass configurations.

3.3.1 Back Surface Temperature

Figure 33 and Figure 34 show the time progression of thermal images for representative fiberglass compositions at 30 kW m^{-2} and 70 kW m^{-2}, respectively.

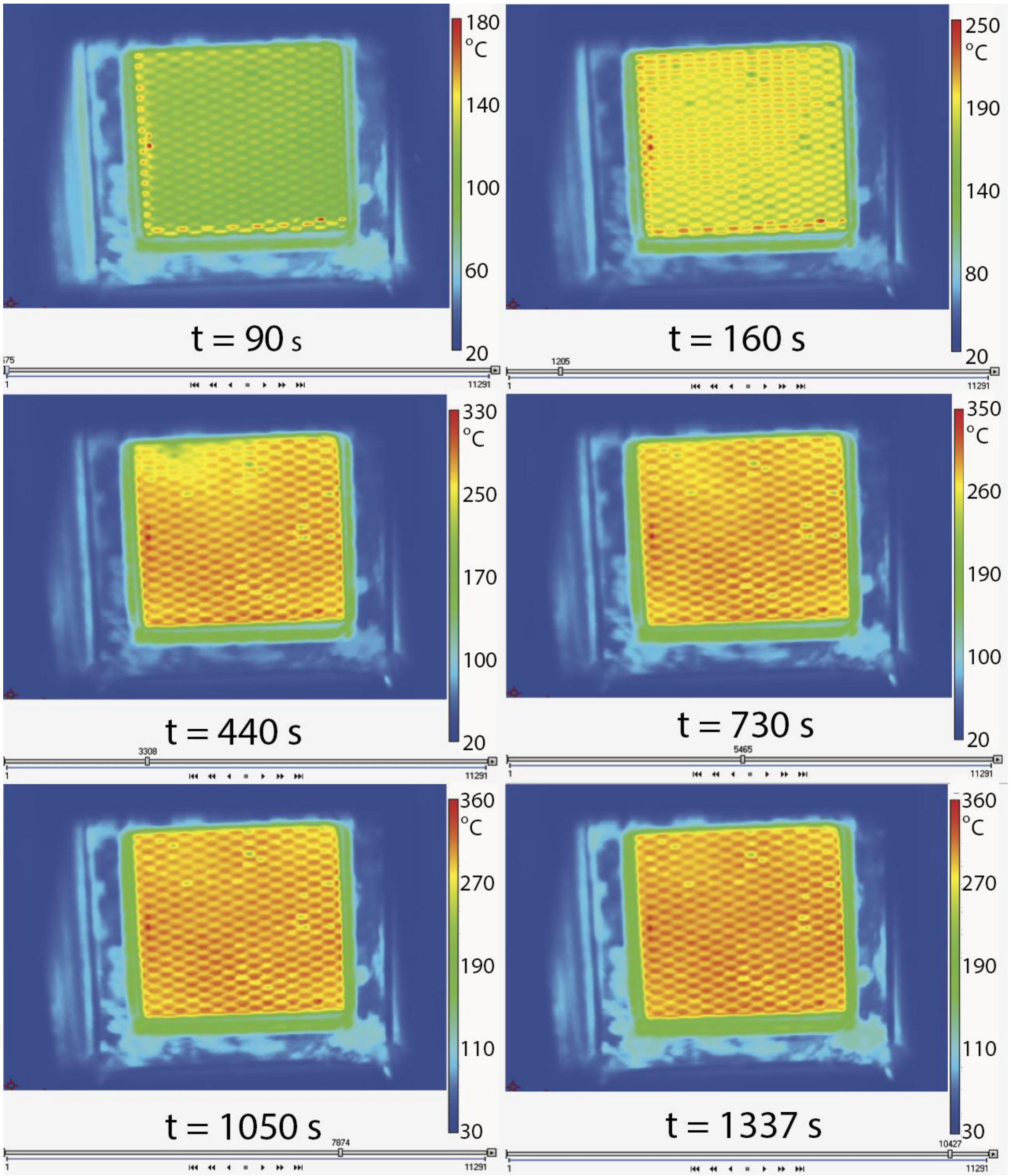

Figure 33. Thermal images from IR camera testing of fiberglass 41 wt% resin at 30kW m^{-2}.

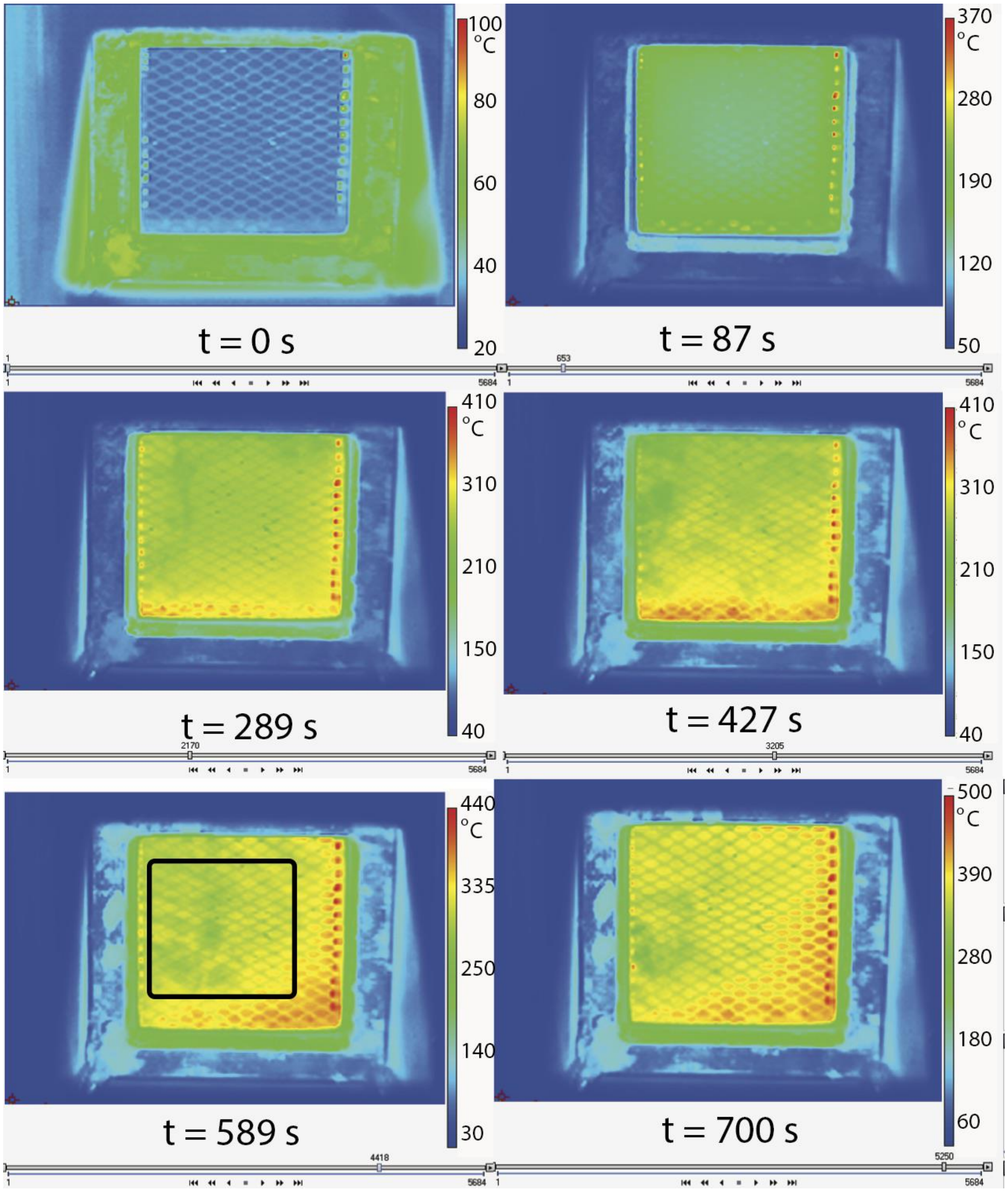

Figure 34. Thermal images from IR camera testing of fiberglass 48 wt% resin at 70 kW m^{-2}. The gaseous species are highlighted in the frame at 589 seconds.

Gaseous volatiles were observed at the back surface of the sample in the frame at 440 seconds for the sample at 30 kW m^{-2}, as shown in Figure 33. The presence of gaseous species was not significant at this low heat flux, and appropriate points were selected for data collection to minimize the impact on the resulting temperature data.

Data at this heat flux was selected as the target for inverse analysis to characterize thermal conductivity. The resulting model parameters for thermal conductivity were found to be sensitive to the surface temperature measurement. The presence of gaseous species was much more pronounced at 70 kW m^{-2}, as highlighted in the frame at 589 seconds for the 48 wt% resin sample in Figure 34. The gaseous species were present in most of the frames and were observed to be at a lower temperature than the sample surface behind them.

The emissive coating applied to the bottom surface of the sample was found to degrade at temperatures in excess of 650 K. This temperature was determined by coating the bottom surface of a copper plate with the emissive paint and exposing it to a steady heat flux. The properties of the copper plate were well-defined. The thermal exposure was modeled, and the temperature where the predicted and experimental temperature profiles deviated was determined to be the temperature where the paint began to degrade [25] [8]. This value corresponded well with the manufacturer's listed temperature of 623 K. These measurements indicated that when the paint began to degrade, the surface temperature of the sample decreased. The temperature profiles were reported only up to this critical value. The error was calculated as two standard deviations of the mean. For a number of profiles, the calculated error was minimal, preventing the data point from being distinguished from the error bar.

The temperature profiles for UP resin at 30 kW m^{-2} and 50 kW m^{-2} are shown in Figure 35.

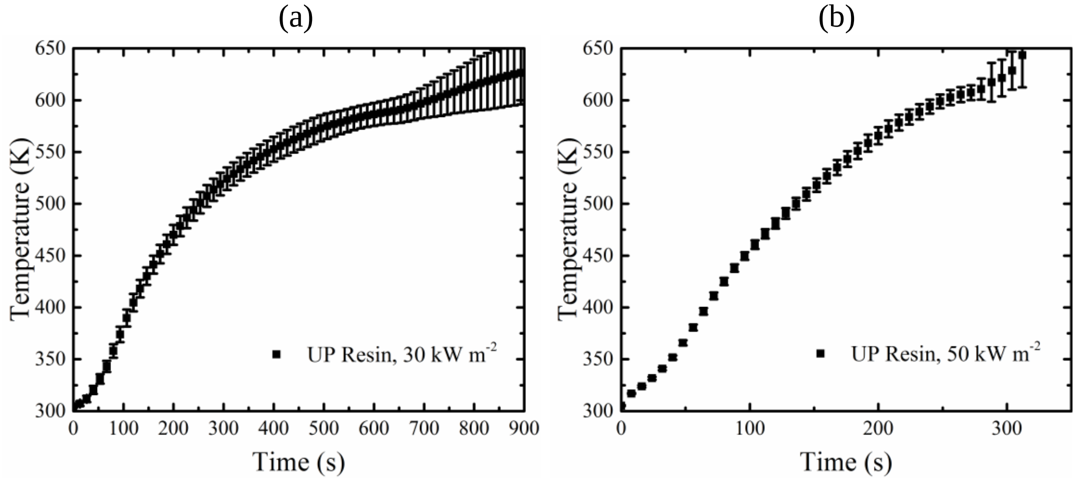

Figure 35. Back surface temperature measurements for UP resin samples during gasification experiments at external heat fluxes of – (a) 30 kW m^{-2}; (b) 50 kW m^{-2}. The top surface of the samples at 30 kW m^{-2} were coated with a layer of the emissive paint that was applied to the back surface of all of the samples.

The experiments performed on UP resin samples experienced deterioration of the boundary conditions, resulting in flaming ignition at 50 and 70 kW m^{-2}. Flaming ignition did not occur during the experimental testing of the UP resin samples at 30 kW m^{-2}. The flame was observed to form on the bottom surface of the sample at 70 kW m^{-2} and spread to the top surface when the edge of the sample deformed and contact was lost between the sample and the Kaowool between two to four minutes after the onset of the exposure to the external heat flux. As a result, the experimental measurements for the UP resin at 70 kW m^{-2} were excluded from further analysis.

During the testing of the UP resin at 50 kW m^{-2} the boundary conditions were steady until the end of the test when the structure of the sample was composed of a fragile char. The char was observed to break, creating discontinuities along the surface of the sample. The discontinuities probably caused a flow path the form that allowed the gases at the back surface of the sample to mix with the nearly anaerobic atmosphere at the top surface. The apparatus was initially intended for a sample with a Kaowool backing and the nitrogen was designed to flow over the top surface of the sample. The oxidative environment at the back surface was able to increase the concentration of oxygen at the sample surface enough to allow for flaming ignition of the sample. The data collected for this configuration was valid up until the onset of this sequence of events. The temperature profile at 50 kW m^{-2} approached the degradation temperature of the emissive paint at approximately 5 minutes, prior to flaming ignition. Thus, the temperature profile was not affected by the observed phenomena.

Figures 36-39 show the temperature profiles for the composite samples exposed to external heat fluxes of 30, 50, and 70 kW m^{-2} during gasification testing. Flaming ignition did not occur during experimental testing of the composite samples.

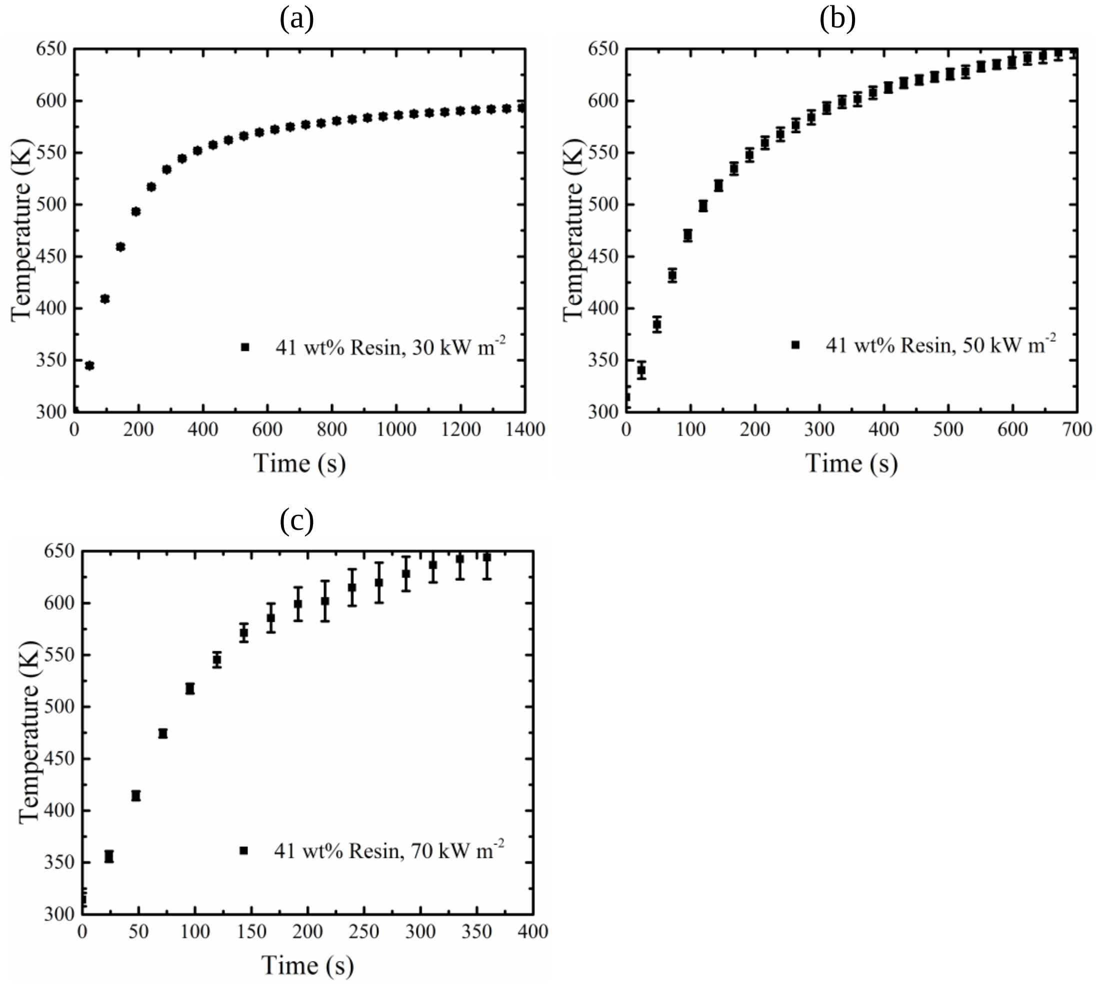

Figure 36. Back surface temperature measurements for fiberglass samples, 41 wt% resin, tested at an external heat flux of – (a) 30 kW m^{-2}; (b) 50 kW m^{-2}; (c) 70 kW m^{-2}.

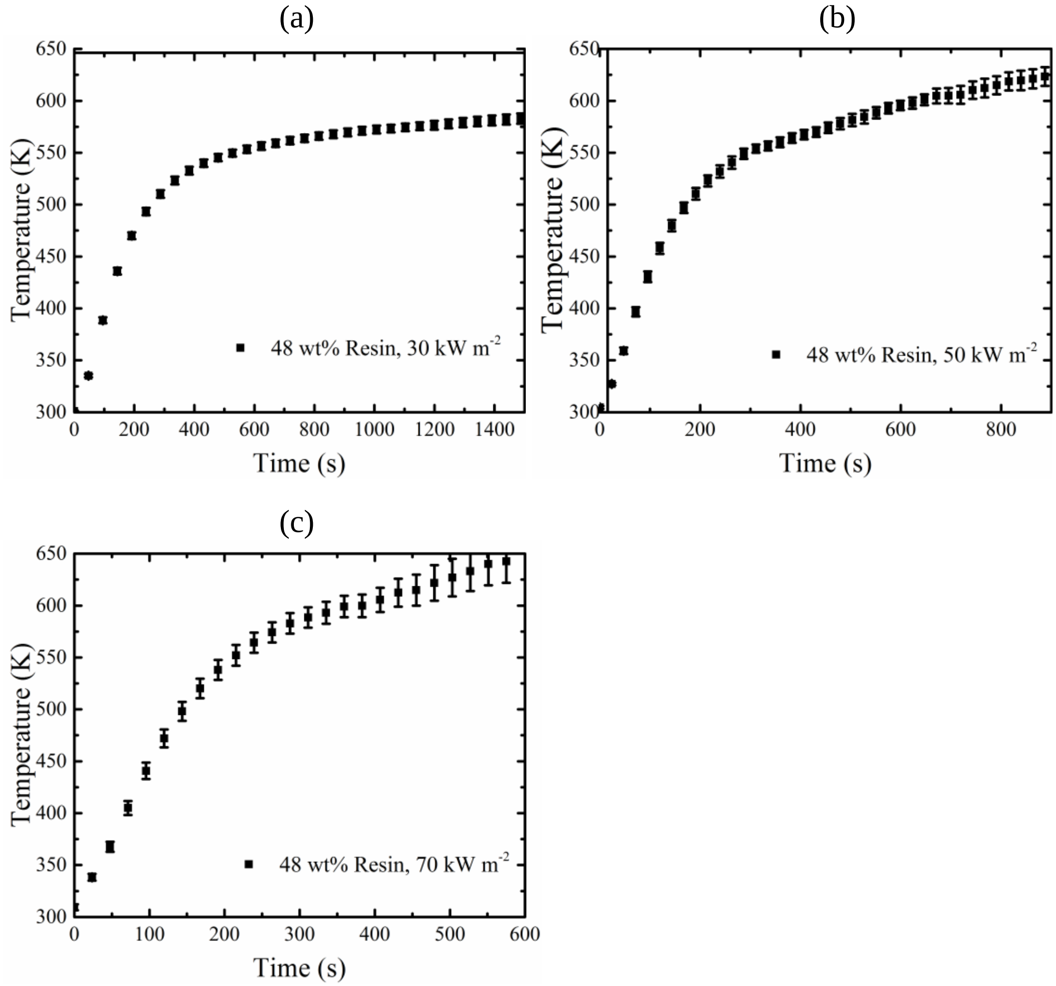

Figure 37. Back surface temperature measurements of fiberglass samples, 48 wt% resin, tested at an external heat flux of – (a) 30 kW m^{-2}; (b) 50 kW m^{-2}; (c) 70 kW m^{-2}.

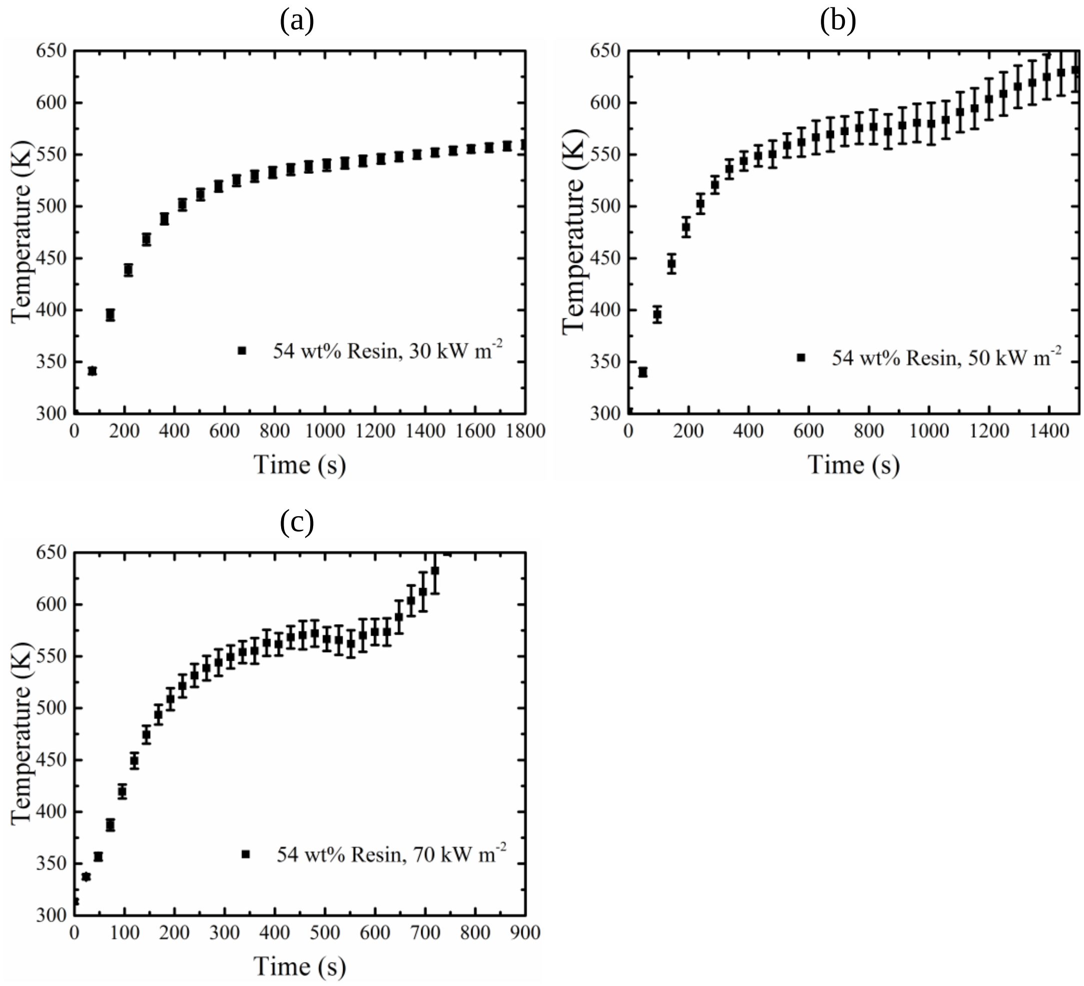

Figure 38. Back surface temperature measurements of fiberglass samples, 54 wt% resin, tested at an external heat flux of – (a) 30 kW m^{-2}; (b) 50 kW m^{-2}; (c) 70 kW m^{-2}.

The temperature increased rapidly during the first two hundred seconds. The rate in rise of the temperature decreased after this initial period. The measured surface temperatures and observed rate of rise of the temperatures were greater for the samples with the higher glass content (i.e., lower resin content).

3.3.2 Density

The density of the material was determined from direct measurements of the samples and averaged for each composition ratio. The mass and dimensions of the samples were recorded prior to each test.

The mass of glass was determined from the weight of the fabric specified by the manufacturer per unit surface area (9.64 oz yd^{-2}), the number of layers of reinforcement in the composite, and the area of the sample. The density of E-glass is well-defined in literature as 2540 kg m^{-3} [20]. The mass of polyester resin was calculated as the difference between the measured mass and the mass of the glass. The average sample density was 1599 ± 12 kg m^{-3} for 40 wt% resin, 1621 ± 16 kg m^{-3} for 48 wt % resin, and 1640 ± 31 kg m^{-3} for 54 wt% resin. The mass of resin in each sample was used to calculate the actual composition ratio and averaged for each nominal composition. Overall, the composites with higher resin content had a higher density. This was probably due to the hand lay-up process, specifically the incomplete saturation of the fiberglass, which may have resulted in the presence of air pockets in the composite. This behavior was more pronounced at lower resin compositions, where the UP resin was limited. The density of the reinforcing glass layers was specified in the model as an effective value to account for this material behavior.

The general expression for the density of the composite samples can be simplified to determine the initial density of the composite consisting of resin and glass reinforcement. The terms are specified in Equation 30 as follows: mf_r is the mass fraction of the resin, mf_g is the mass fraction of the glass, ρ_r is the density of the resin, ρ_g is the density of the glass, and ρ_s is the density of the composite sample.

$$\frac{mf_r}{\rho_r} + \frac{mf_g}{\rho_g} = \frac{1}{\rho_s} \tag{30}$$

A representative experimental data set must be selected to evaluate the above expression for the density of the resin in order to characterize a single system capable of describing all of the configurations. The median sample density was selected to be most representative of the material at 1621 kg m^{-3}. The average experimental measurements for the nominally 48 wt% resin samples were substituted into the above expression, with the density of the fiberglass to yield an effective density for the UP resin in the composite samples of 1160 kg m^{-3}. This value agrees with the ranges provided in literature [33].

The initial thickness of the sample was measured prior to testing and the final thickness of the sample was measured after the sample had returned to room temperature. The average overall increase in thickness was found to be 6.1%, with a standard deviation of 10.7%. During experimental testing, it was observed that at low heat fluxes the sample would not change thickness and at higher heat fluxes the sample would slightly swell. This behavior was difficult to quantify as the delamination process occurred. The change in thickness was assumed to be negligible since the observed and calculated behaviors were both relatively small, but contradictory. The densities of the intermediate species were specified from the initial density and reduced proportionally to the condensed phase yield for each reaction. The individual values are given in Table 11.

Table 11. Density of constituent species for composite samples.

Species	Density (kg m^{-3})
Virgin Resin	1160
Virgin Resin 1	1160
Intermediate 1	1084.6
Intermediate 2	316.7
Char	89.3
Fiberglass	2540

The density of the UP resin calculated as the average from experimental measurements for the pure resin samples tested and found to be 1240 ± 9 kg m^{-3}. The density calculated for the pure UP resin samples was 800 kg m^{-3} greater than the value calculated for the composite samples. The difference was probably due to the presence of air bubbles within the composite samples. The density for modeling the pure UP resin samples was specified separately from the density of the composite samples. The pure UP resin samples were assumed to degrade such that the densities of the decomposition species maintained a constant thickness of the sample, as given in Table 12.

Table 12. Density of the pure UP resin and decomposition species.

Species	Density (kg m^{-3})
Virgin Resin	1240
Virgin Resin 1	1240
Intermediate 1	1159.4
Intermediate 2	338.5
Char	95.5

3.3.3 Thermal Conductivity

The thermal conductivity of the virgin resin and decomposition species were characterized through inverse analysis targeting the exposed back surface temperature profile of the UP resin during gasification experiments at 30 kW m^{-2}. The top surface of the samples were coated with a layer of the emissive paint applied to the bottom surface of all of the samples. The absorption coefficient of all of the species was set to 100 m^{-2} kg^{-1} to model the behavior of the emissive surface coating, which prevented in-depth radiation absorption. Inverse analysis was performed in 100-second time increments to reduce the number of unknown parameters influencing the system. By limiting the time interval, the thermal conductivity could be analyzed for partially-isolated resin components beginning with the virgin resin, followed by the intermediate, and continuing until all species were analyzed. The virgin resin and first intermediate were assumed to follow the same linear temperature dependency to limit the number of variables in the model, as described by Equation 31.

$$k_{VR} = k_{VR1} = k_{Int1} = 0.03 + 3.5 \times 10^{-4}T \qquad (31)$$

The thermal conductivity of the he char was characterized as a third order polynomial based on the radiative diffusion approximation [34], as shown in Equation 32.

$$k_{Char} = 0.18 + 8 \times 10^{-10}T^3 \qquad (32)$$

This expression accounts for porosity effects that drive thermal radiation during char formation at elevated temperatures [6]. The thermal conductivity of the second intermediate was characterized as a combination of the values for the virgin resin and char, as shown in Equation 33.

$$k_{Int2} = 0.23 + 3.5 \times 10^{-4}T + 8 \times 10^{-10}T^3 \qquad (33)$$

Table 13. Thermal conductivity of UP resin and decomposition species.

Species	Thermal Conductivity (W m^{-1} K^{-1})
Virgin Resin	$0.03 + 3.5 \times 10^{-4}T$
Virgin Resin 1	$0.03 + 3.5 \times 10^{-4}T$
Intermediate 1	$0.03 + 3.5 \times 10^{-4}T$
Intermediate 2	$0.23 + 3.5 \times 10^{-4}T + 8 \times 10^{-10}T^3$
Char	$0.18 + 8 \times 10^{-10}T^3$

The agreement between the model prediction and the series of experimental measurements is shown in Figure 39.

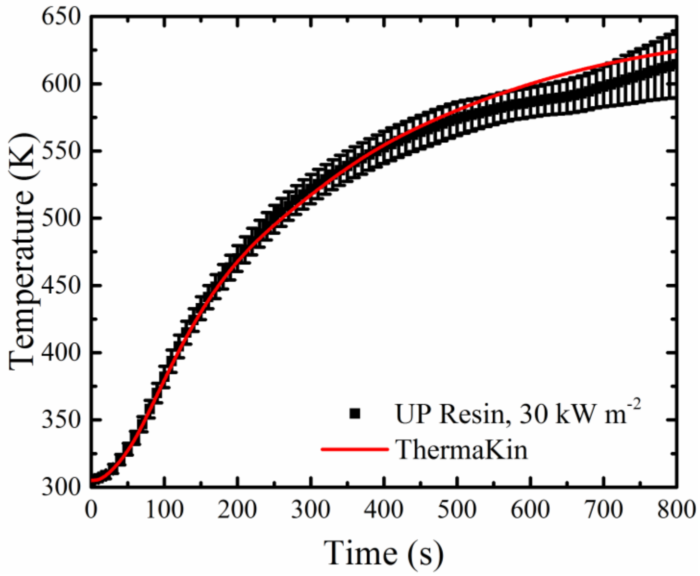

Figure 39. Agreement between UP resin back surface temperature profiles from experimental measurement and model prediction at 30 kW m^{-2}.

The parameterized model was able to reproduce the experimental data well. The characterized properties were evaluated for the ability to predict the temperature profiles for the experimental measurements for UP resin at external the heat flux 50 kW m^{-2}, as shown in Figure 40.

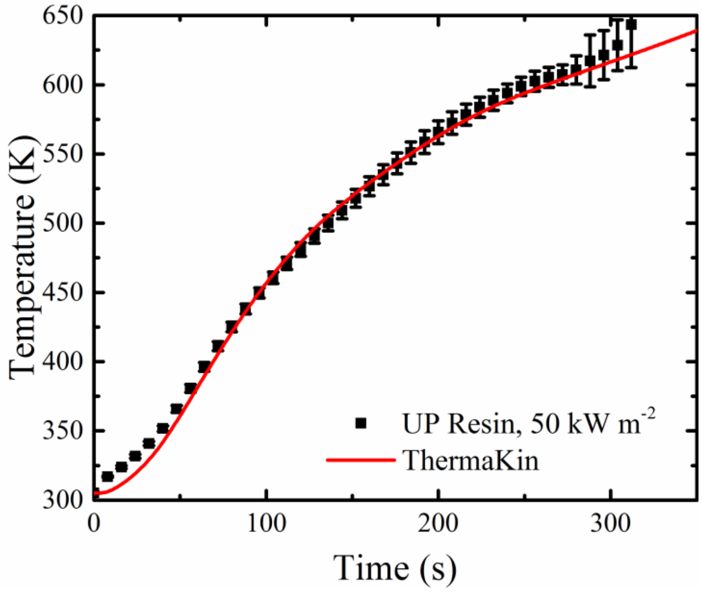

Figure 40. Agreement of bottom surface temperature profiles for UP resin from experimental measurements and model predictions at 50 kW m^{-2}.

The UP resin samples tested at 50 kW m^{-2} did not have a coating on the surface facing the truncated cone heater. The absorption coefficients were set to the experimentally determined values to model the experimental samples. The temperature profile at 50 kWm^{-2} was replicated well by the model. The agreement between the model and experimental temperature profiles at 50 kW m^{-2} supports the previously characterized values for the absorption coefficient and the high emissivity of the UP resin and decomposition species.

The thermal conductivity of the fiberglass reinforcement was assumed to be described by a linear temperature-dependent program, which was evaluated by targeting the bottom surface temperature profile through manual iterations using inverse analysis. The sample configuration selected for the target data set was the 48 wt% resin composite at 30 kW m^{-2}. This sample was selected because the samples were observed to have minimal imperfections that may indicate non-ideal material behavior and the measurements of the sample size and calculated composition were consistent. The resulting parameter was defined using Equation 34.

$$\mathrm{k_{glass}} = 0.48 - 5.5 \times 10^{-4}\mathrm{T} \tag{34}$$

This expression was less than zero at temperatures greater than 872.7 K. The transition to a negative value is beyond the scope of physical possibility. A piece-wise function was introduced to the model that allowed the thermal conductivity to follow Equation 33 at temperatures below 781.8 K; after this point, the parameter transitioned to a constant value of 0.05 W m^{-1}K^{-1}, in order to maintain realistic values for the physical process. Agreement between the experimental profile and the model is shown in Figure 41.

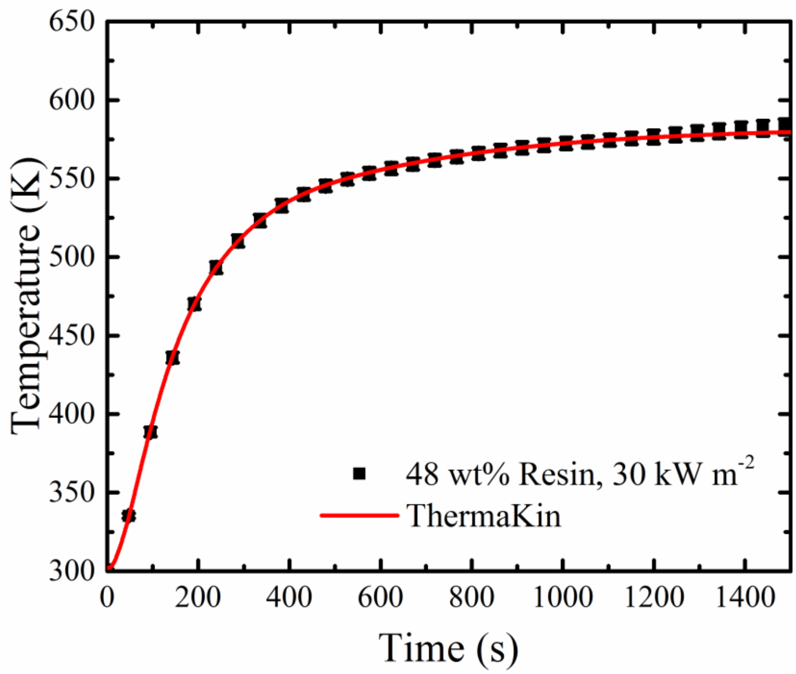

Figure 41. Agreement of temperature profiles for the fiberglass composite, nominally 48 wt% resin, from experimental measurements and the model prediction.

The error bars for surface temperature measurements were calculated as two standard deviations of the mean. The fully parameterized model was evaluated for the agreement between predicted and experimental temperature profiles at external heat fluxes of 30, 50, and 70kW m^{-2} for composition ratios of 41 wt%, 48 wt%, and 54 wt% resin by adjusting only the composition ratios, sample thickness, and thermal boundary conditions. The complete sets of temperature profiles for the 41 wt% resin composites are shown in Figure 42.

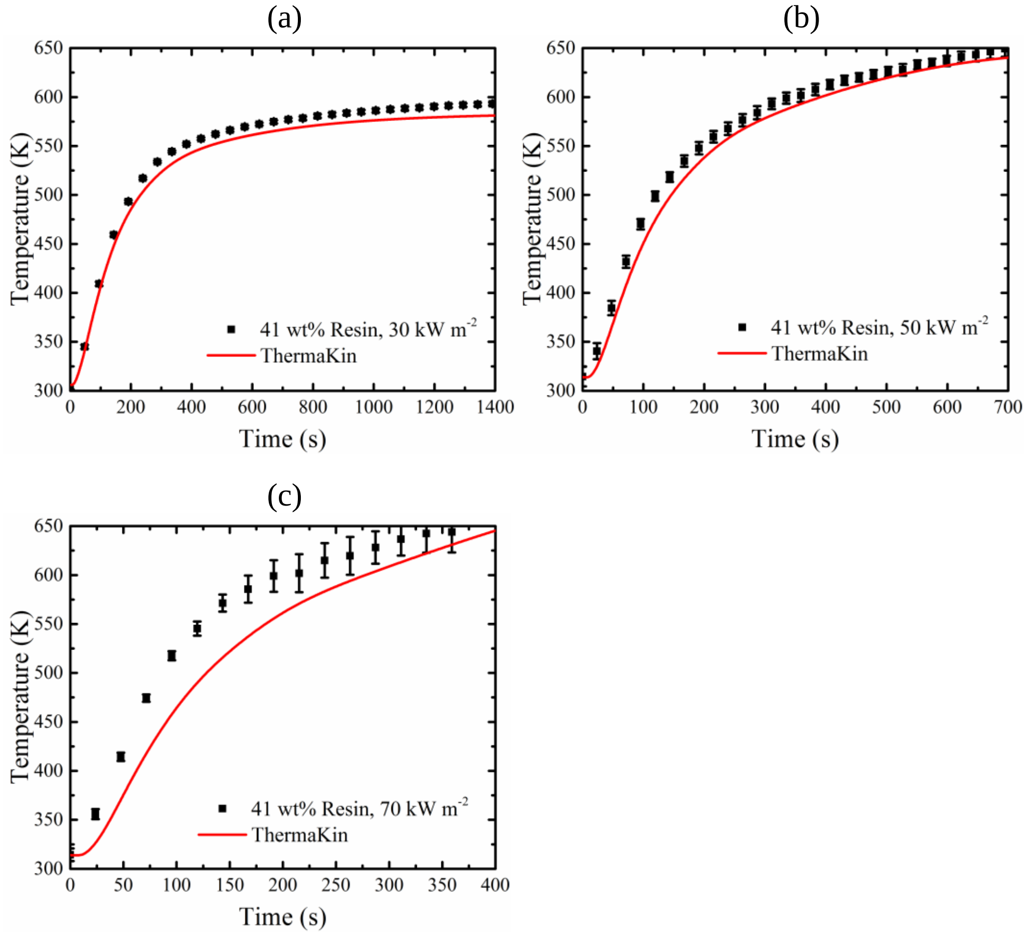

Figure 42. Back surface temperature profiles from experimental data and model predictions for fiberglass samples composed of 41 wt% resin and tested at an external heat flux of – (a) 30 kW m^{-2}; (b) 50 kW m^{-2}; (c) 70 kW m^{-2}.

The model slightly under-predicted the temperature profiles systematically for the lower resin composition. The deviation was most significant at 70 kW m^{-2}. This was possibly the result of physical processes occurring in the composite that were not accounted for in the model, such as the presence of air bubbles in the sample.

The complete sets of temperature profiles for the 48 wt% resin composites are shown in Figure 43.

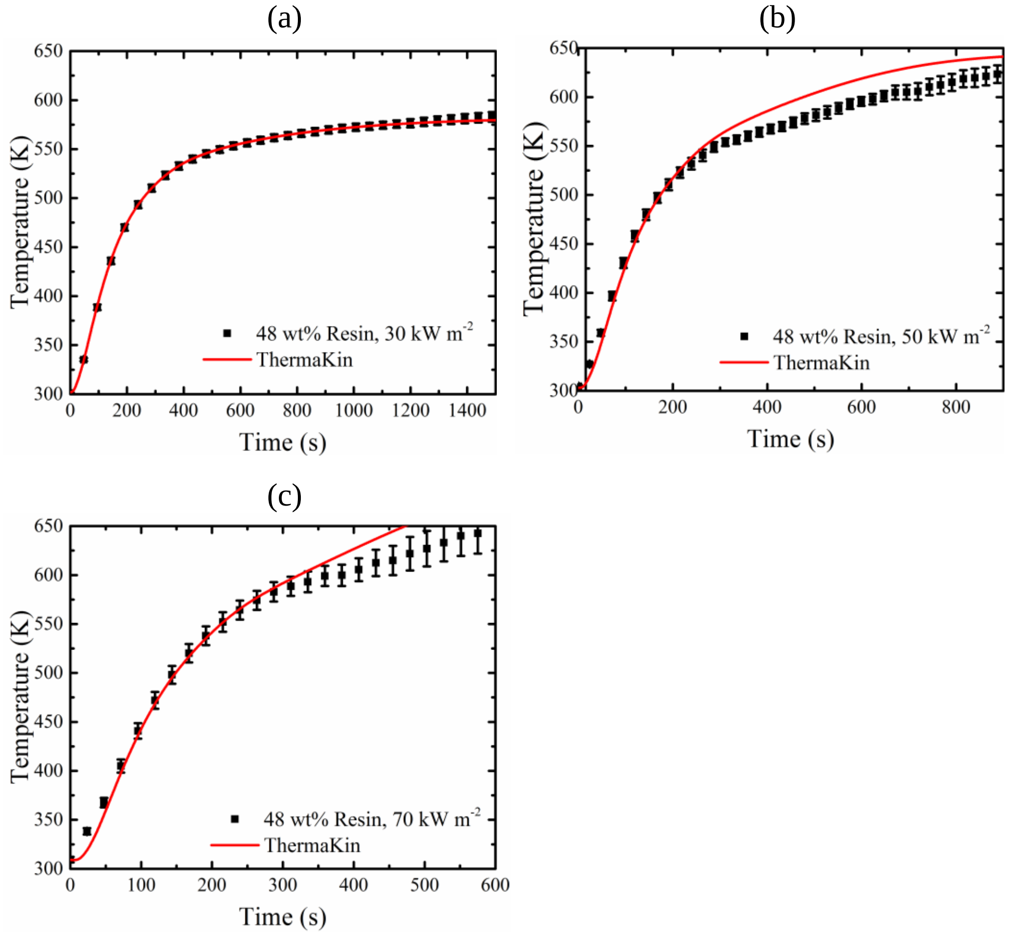

Figure 43. Back surface temperature profiles from experimental data and model predictions for fiberglass samples composed of 48 wt% resin and tested at an external heat flux of – (a) 30 kW m^{-2}; (b) 50 kW m^{-2}; (c) 70 kW m^{-2}.

The model was able to reproduce the temperature profiles accurately for the majority of the experimental measurements from the 48 wt% resin samples over the range of heat fluxes. The model began to over-predict the experimental measurements for the 48 wt% resin samples at 50 and 70 kW m^{-2} as the surface temperature exceeded 550 K. These over-predictions were probably caused by the presence of gaseous species at the back surface of the sample and the onset of thermal degradation of the layer of emissive paint on the back of the sample, which would both cause the reported measurements to be lower than the true surface temperature.

The complete sets of temperature profiles for the 54 wt% resin composites are shown in Figure 44.

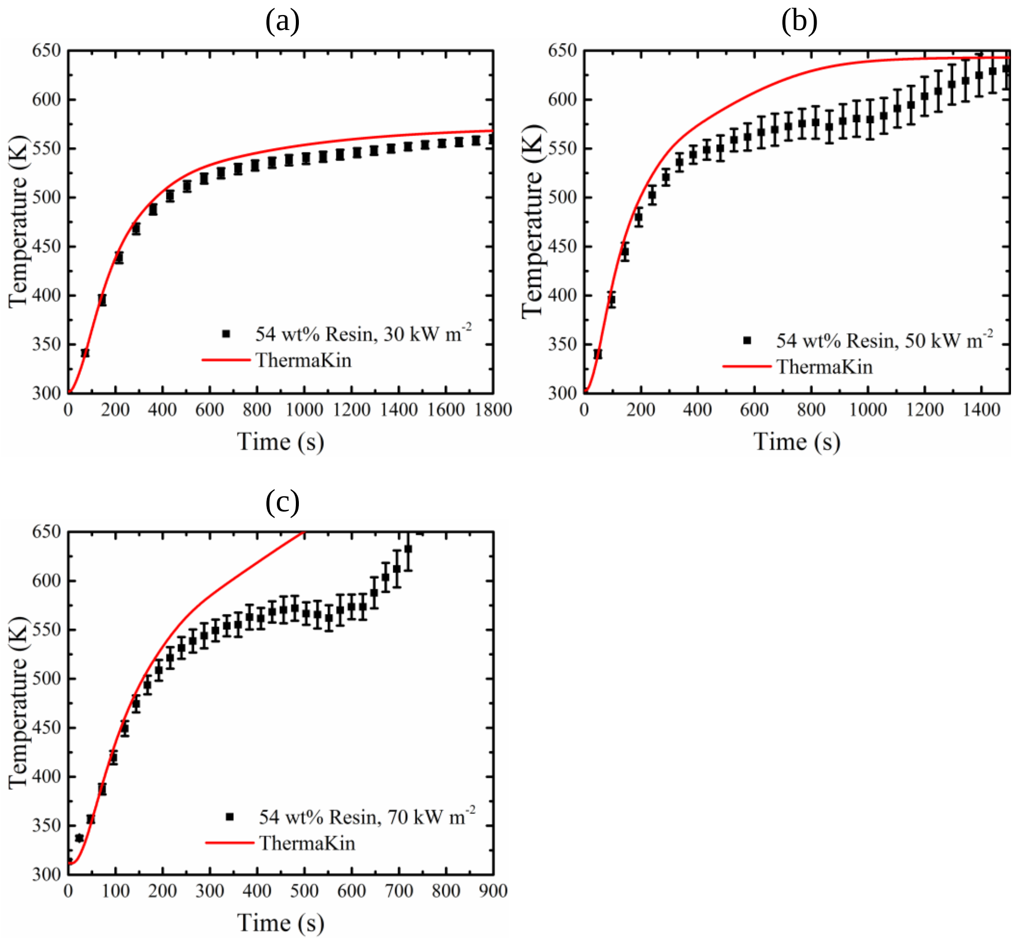

Figure 44. Back surface temperature profiles from experimental data and model predictions for fiberglass samples composed of 54 wt% resin and tested at an external heat flux of – (a) 30 kW m^{-2}; (b) 50 kW m^{-2}; (c) 70 kW m^{-2}.

The model slightly over-predicted the temperature profiles for the 54 wt% resin samples in a systematic manner similar to the behavior noted for the 41 wt% resin samples. There were additional over-predictions at 50 and 70 kW m^{-2} similar to the behavior noted for the samples at 48 wt% resin. The deviations between the model predicted curves and the experimental measurements were probably the result of a combination of the behaviors noted for the 41 and 48 wt% resin samples.

In Figure 45, the thermal conductivities of the resin and decomposition species are shown over the temperature range each specie was present in the system.

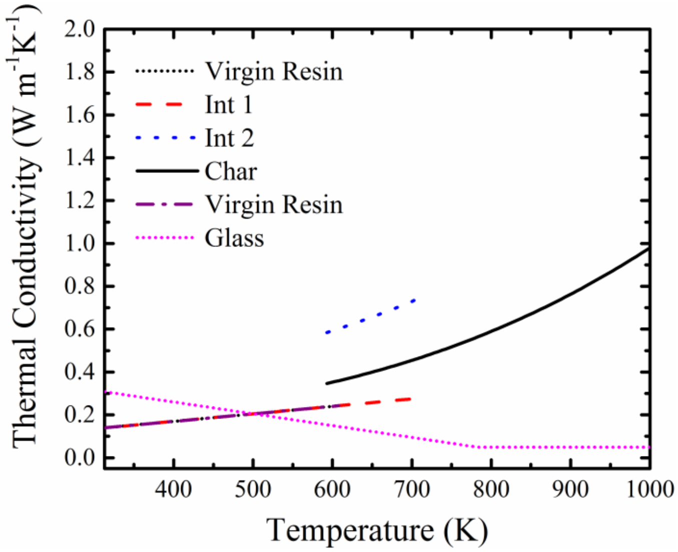

Figure 45. Thermal conductivity of individual species over the temperature range the species was present.

At ambient conditions, the thermal conductivity of the resin was approximately 0.3 W m^{-1}K^{-1} and increased linearly to approximately 0.44 W m^{-1}K^{-1} for both the virgin resin and the first intermediate during the initial reaction. The thermal conductivities of the second intermediate and the char were 0.3 W m^{-1}K^{-1} at 500 K and increased to 2.4 W m^{-1}K^{-1} at 1000 Kelvin. The thermal conductivity characterized for the fiberglass was notably lower than typical literature values, which range from 1.13-1.3 W m^{-1}K^{-1} [10] [17] [20]. This result was probably a caused by physical processes occurring within the material that were not accounted for in the model, such as the presence of air pockets within the micro-structure of the composite due to incomplete wet-though of the fiber reinforcement with resin during fabrication.

3.3.4 Mass Loss Rate

Three tests were performed at each composition ratio and heat flux. The three-second average was statistically combined for each configuration to produce one representative graph of the mass loss rate for each configuration. The output frequency of the measurement was also reduced to produce a concise figure for each configuration. Each figure was considered individually to ensure that the integrity of the data was maintained during this portion of the analysis. The resulting profiles for the mass loss rate, as a function of time, are shown in Figures 46-49. The uncertainty was calculated as two standard deviations of the mean.

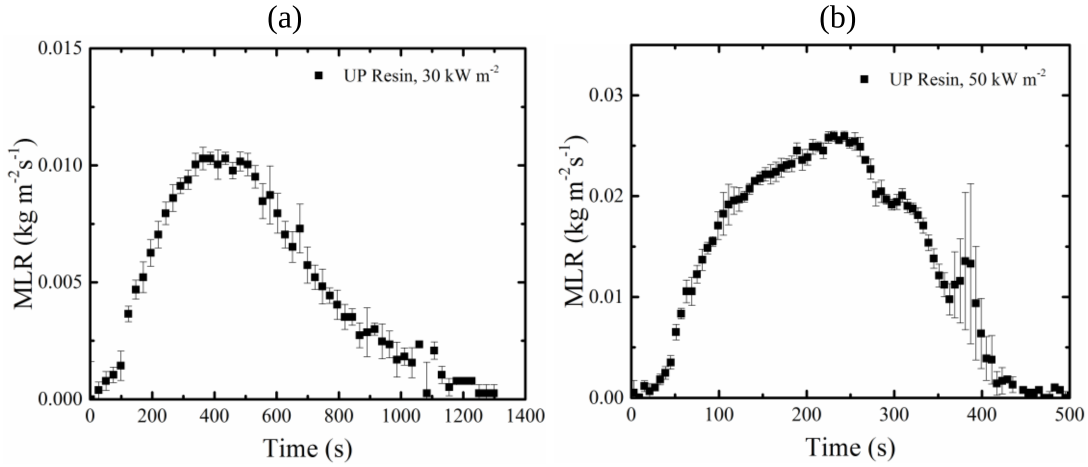

Figure 46. Mass loss rate from gasification experiments for UP resin, with a foil backing, at external heat fluxes of – (a) 30 kW m^{-2}; and (b) 50 kW m^{-2}.

The gasification experiments for UP resin were determined to be repeatable for the range of external heat fluxes. The initial peak mass loss rate occurred at approximately 400 and 250 seconds for external heat fluxes of 30 and 50kW m^{-2}, respectively. The corresponding peak mass loss rates were 0.012 and 0.025 kg m^{-1}s^{-1}, respectively.

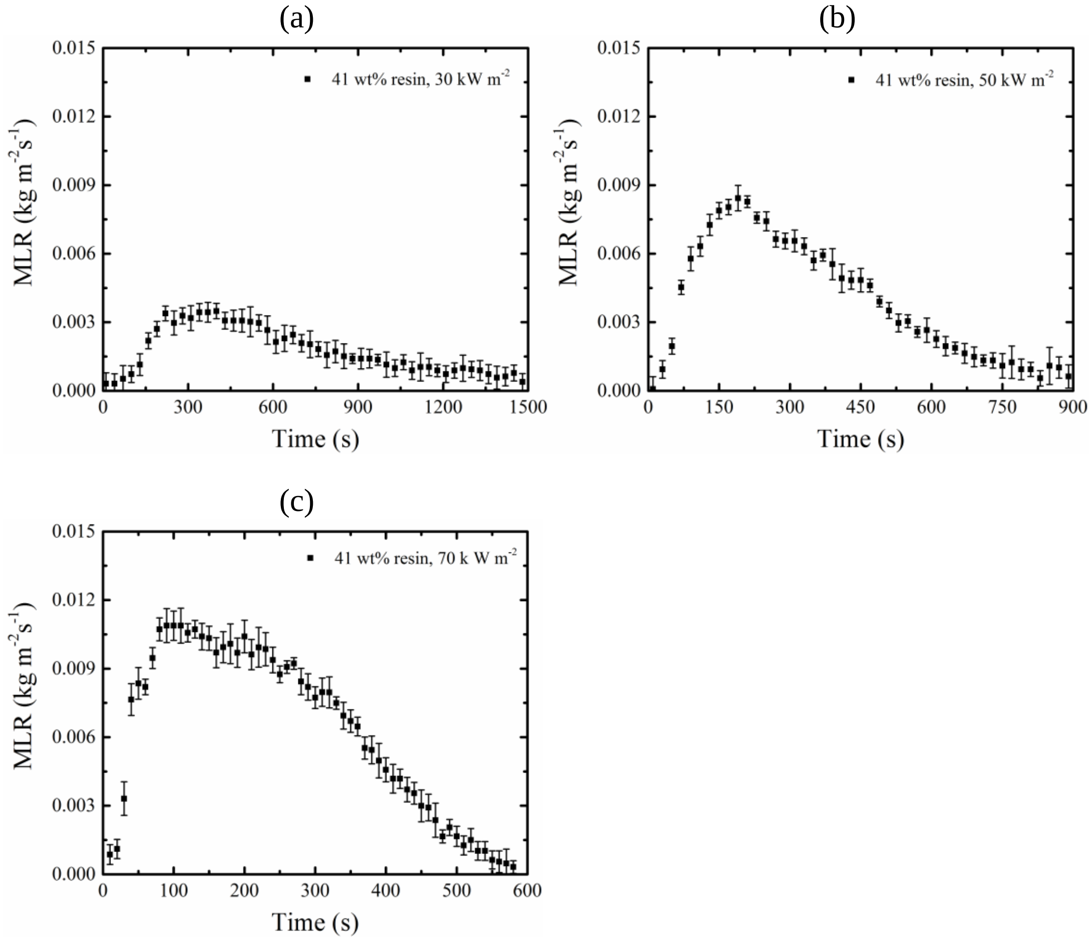

Figure 47. Mass loss rate measured during gasification experiments for fiberglass samples composed of 41 wt% resin and tested at an external heat flux of – (a) 30 kW m^{-2}; (b) 50 kW m^{-2}; (c) 70 kW m^{-2}.

The fiberglass samples exhibited repeatable behavior for the range of external heat fluxes at all of the composition ratios. At 70 kW m^{-2}, the peak mass loss rate occurred approximately 70 seconds after the initial increase. This peak corresponded to a mass loss rate ranging from 0.011-0.014 g m^{-2}s^{-1}. The mass loss was rapid following the onset of the test due to the significant thermal exposure. These tests were the shortest, and the majority of the mass loss occurred during the first 900 seconds, more than twice the duration of the UP resin.

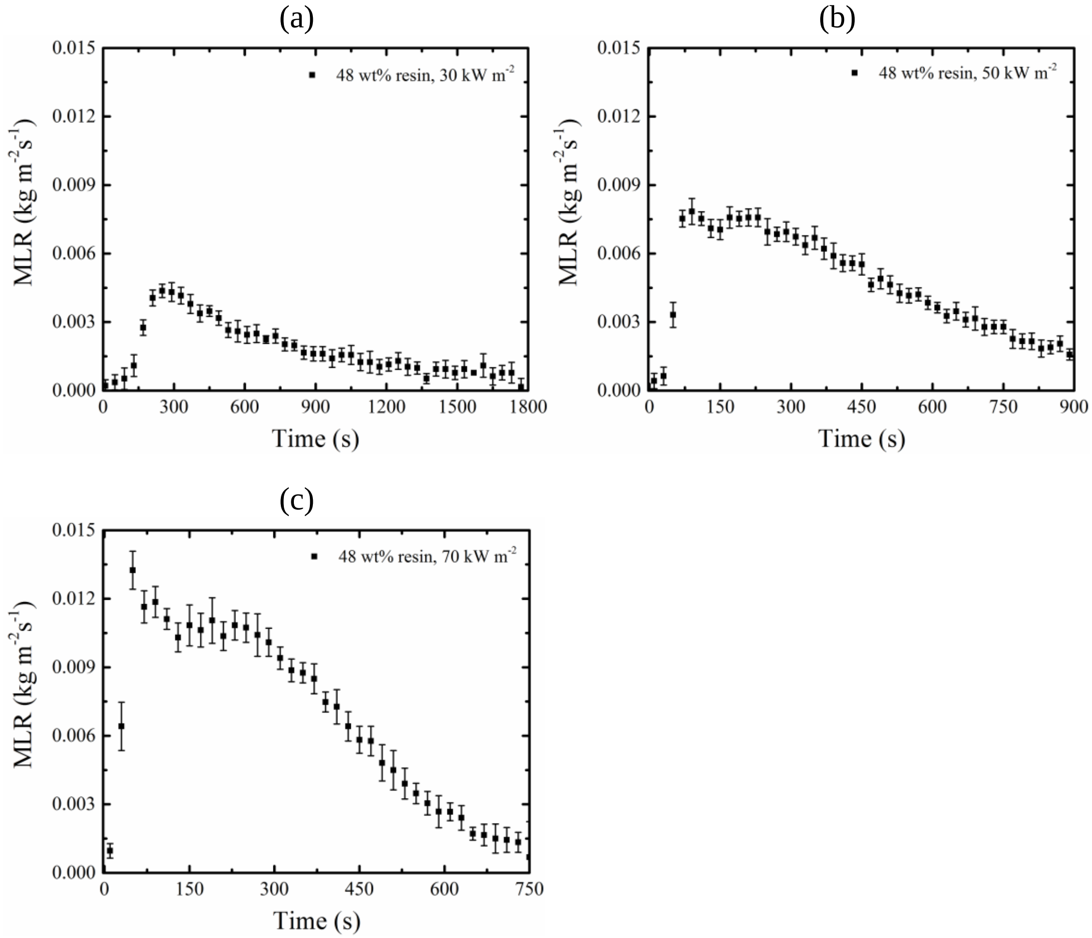

Figure 48. Mass loss rate measured during gasification experiments for fiberglass samples composed of 48 wt% resin and tested at an external heat flux of – (a) 30 kW m^{-2}; (b) 50 kW m^{-2}; (c) 70 kW m^{-2}.

At 50 kW m^{-2}, the peak occurred over the range 0f 100-200 seconds. This peak corresponded to a mass loss rate ranging from 0.007-0.009 g $m^{-2}s^{-1}$. The initial increase in mass loss rate was much less dramatic for the lower external heat flux, but still occurred within the first 2-3 minutes. These tests were typically performed for 900 seconds, but mass loss was observed for up to 1500 seconds when the experimental conditions allowed.

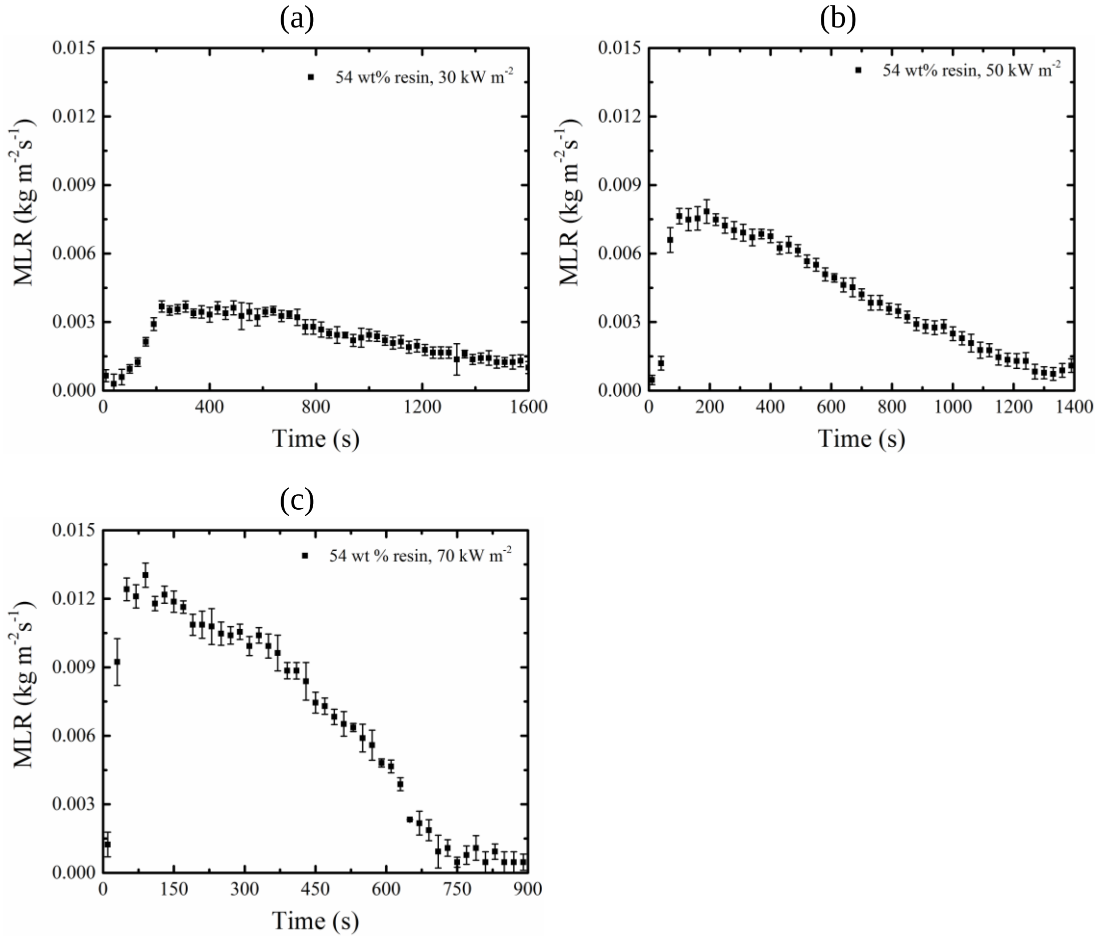

Figure 49. Mass loss rate measured during gasification experiments for fiberglass samples composed of 54 wt% resin and tested at an external heat flux of – (a) 30 kW m^{-2}; (b) 50 kW m^{-2}; (c) 70 kW m^{-2}.

At 30 kW m^{-2}, the peak occurred from 200-500 seconds. This peak corresponded to a mass loss rate ranging from 0.003-0.004 g m^{-2}s^{-1}. The relatively minor external heat flux resulted in a sustained peak mass loss rate for more than six minutes. These tests were the longest, typically running for approximately 1500-1800 seconds before the decomposition process neared completion and the available nitrogen for the system was depleted.

The orientation of the fiberglass sample during gasification testing was found to have an impact on the resulting mass loss rate. Samples were tested with the matte surface facing the cone heater and the glossy surface facing down, always coated with a layer of emissive paint. When the sample configuration for 54 wt% resin at 70 kW m^{-2} was tested in the opposite orientation, with the glossy surface exposed to the radiant heater, the initial peak mass loss rate increased over 90%. The glossy appearance was the result of the sample surface being exposed to the ambient atmosphere during the polymerization process.

3.3.5 Validation

The ability of the single set of characterized material properties to describe the material behavior of UP resin and fiberglass composites of varying compositions for a range of thermal exposures was evaluated by comparing the model predictions with a set of experimental data independent from the measurements considered for property determination. The complete set of material properties are given in Table 14.

Table 14. Complete set of material properties.

Property	Value
θ_2	0.935
θ_3	0.292
θ_4	0.282
A_1	$8.3 \times 10^5\ s^{-1}$
E_1	$7.7 \times 10^4\ J\ mol^{-1}$
A_2	$4.99 \times 10^5\ s^{-1}$
E_2	$9.7 \times 10^4\ J\ mol^{-1}$
A_3	$6.2 \times 10^8\ s^{-1}$
E_3	$1.45 \times 10^5\ J\ mol^{-1}$
h_1	$-37000\ J\ kg^{-1}$
h_2	$-336000\ J\ kg^{-1}$
h_3	$-90000\ J\ kg^{-1}$
$c_{p,VR}$	$-108136 + 647.5 \times T - 0.955$
$c_{p,VR1}$	$843.5 + 2.28\ \times T(J\ kg^{-1}K^{-1})$
$c_{p,Int1}$	$843.5 + 2.28\ \times T(J\ kg^{-1}K^{-1})$
$c_{p,Int2}$	$1760\ (J\ kg^{-1}K^{-1})$
$c_{p,Char}$	$1480\ (J\ kg^{-1}K^{-1})$
k_{VR}	$0.03 + 3.5 \times 10^{-4}\ T\ (W\ m^{-1}K^{-1})$
k_{VR1}	$0.03 + 3.5 \times 10^{-4}\ T\ (W\ m^{-1}K^{-1})$
k_{Int1}	$0.03 + 3.5 \times 10^{-4}\ T\ (W\ m^{-1}K^{-1})$
k_{Int2}	$0.21 + 3.5 \times 10^{-4}\ T + 8$
k_{Char}	$0.18 + 8 \times 10^{10} T^{-3}\ (W\ m^{-1}K^{-1})$
ϵ_{vr}	0.95
ϵ_{vr1}	0.95
ϵ_{Int1}	0.95
ϵ_{Int2}	0.86
ϵ_{Char}	0.86
α_{VR}	$2.1\ m^2\ kg^{-1}$
α_{VR1}	$2.1\ m^2\ kg^{-1}$
α_{Int1}	$2.1\ m^2\ kg^{-1}$
α_{Int1}	$100\ m^2\ kg^{-1}$
α_{Int1}	$100\ m^2\ kg^{-1}$

The complete set of material properties was developed through a series of well-defined experiments, systematic analysis, and practical considerations. The comparisons between the predicted and experimental mass loss rates for UP resin are provided in Figure 50.

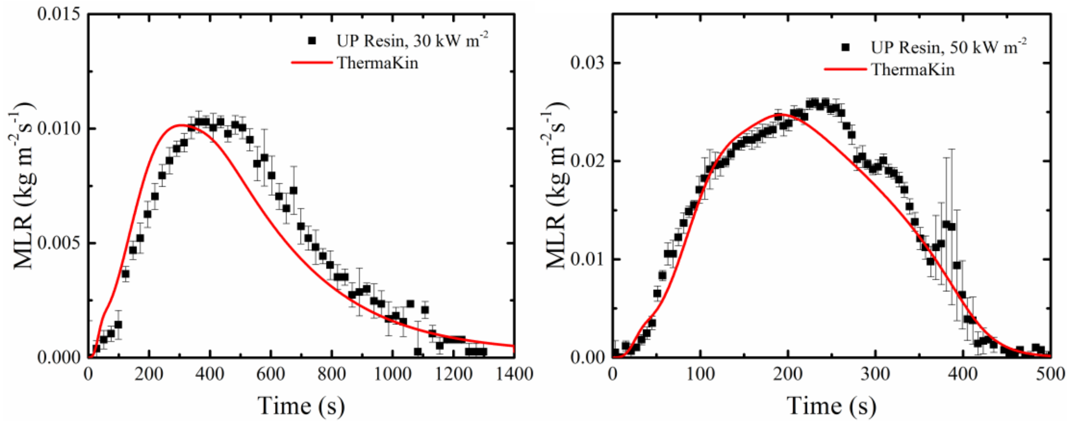
(a)
(b)

Figure 50. Mass loss rate profiles from experimental data and model simulations for UP resin at an external heat fluxes of – (a) 30; and (b) 50 kW m^{-2}.

Overall, the model produced mass loss rate profiles that agreed very well with the experimental measurements.

The predictive capability of the model was compared with the experimental results for the mass loss rate of fiberglass samples during gasification testing, as shown in Figures 51-54.

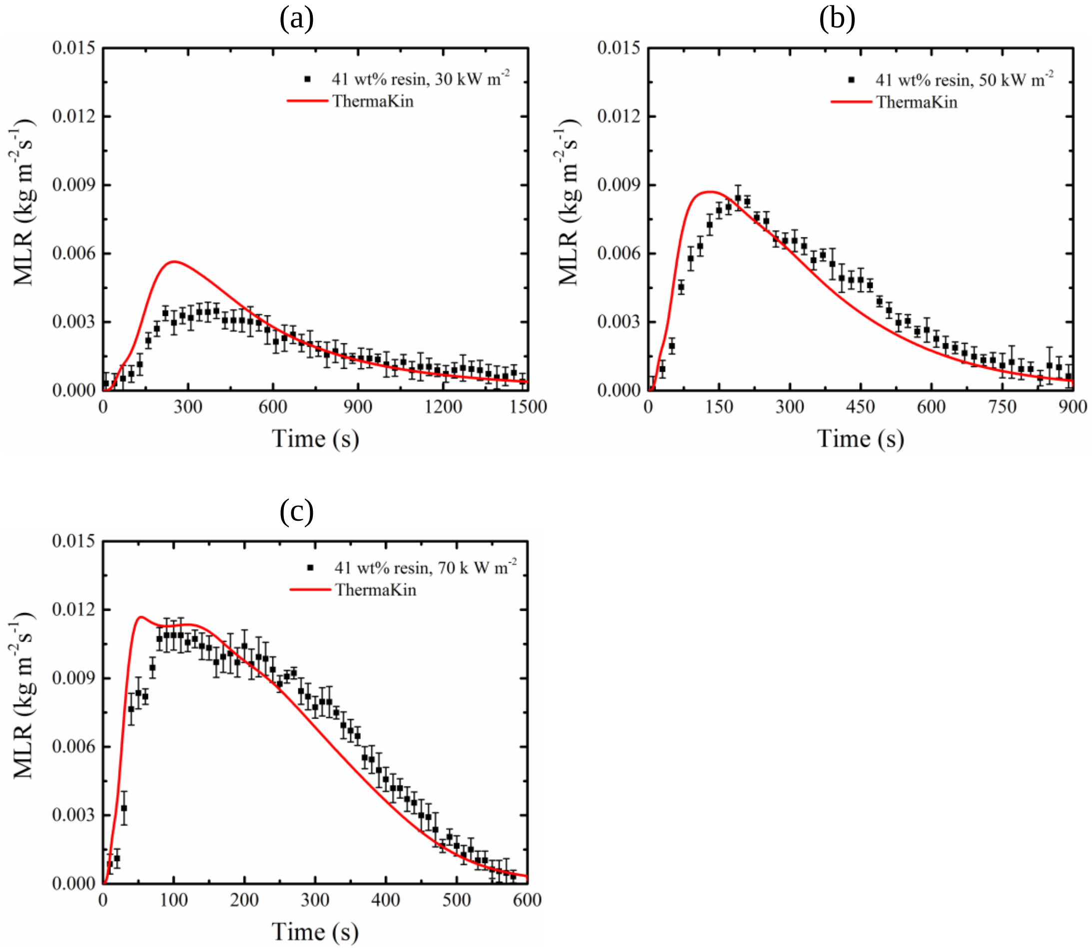

Figure 51. Mass loss rate from experimental data and model simulations for 41 wt% resin composite samples tested at an external heat flux of – (a) 30 kW m^{-2}; (b) 50 kW m^{-2}; (c) 70 kW m^{-2}.

Overall, the model adequately determined the initial rise, the location of the peak mass loss rate, and the decay. The peak mass loss rate was systematically over-predicted at 30 kW m^{-2}. The model was able to reproduce the entirety of the mass loss rate profile very well for experimental testing at 50 kW m^{-2}.

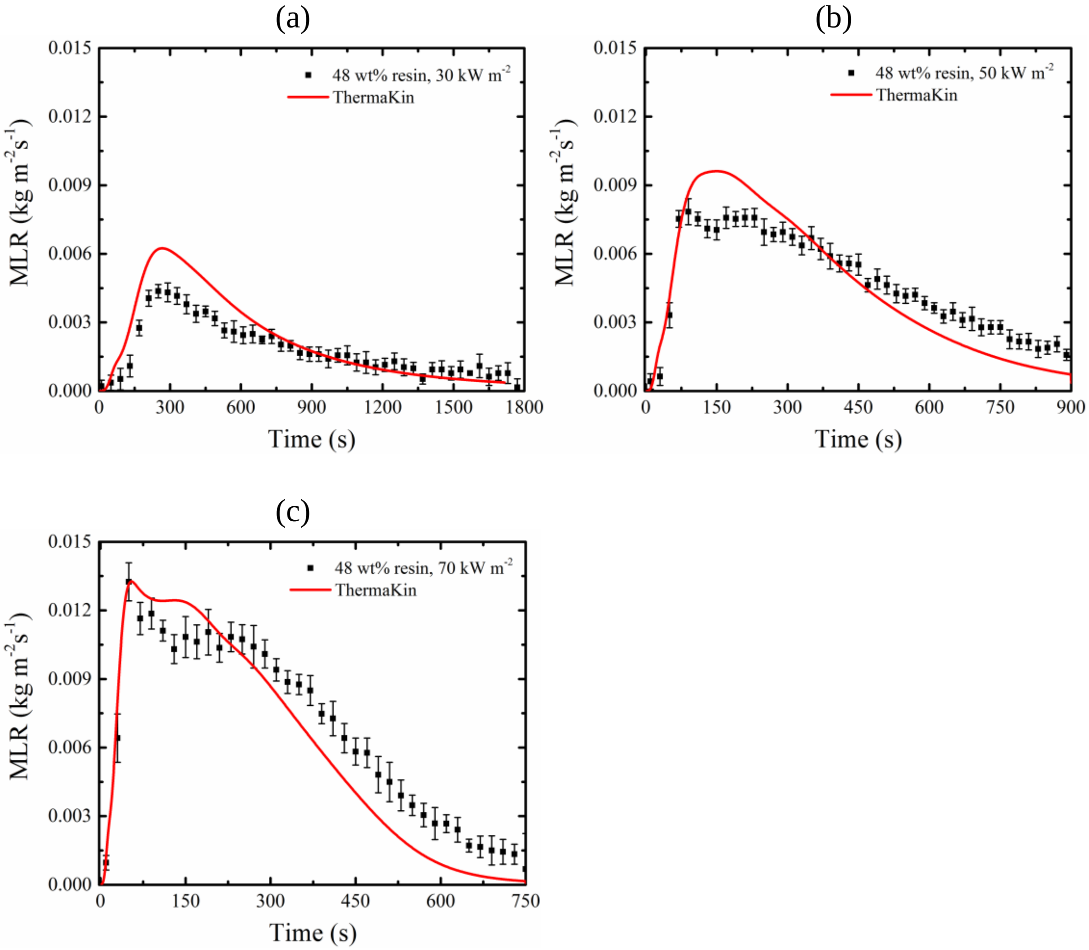

Figure 52. Mass loss rate from experimental data and model simulations for 48 wt% resin composite samples tested at an external heat flux of – (a) 30 kW m^{-2}; (b) 50 kW m^{-2}; (c) 70 kW m^{-2}.

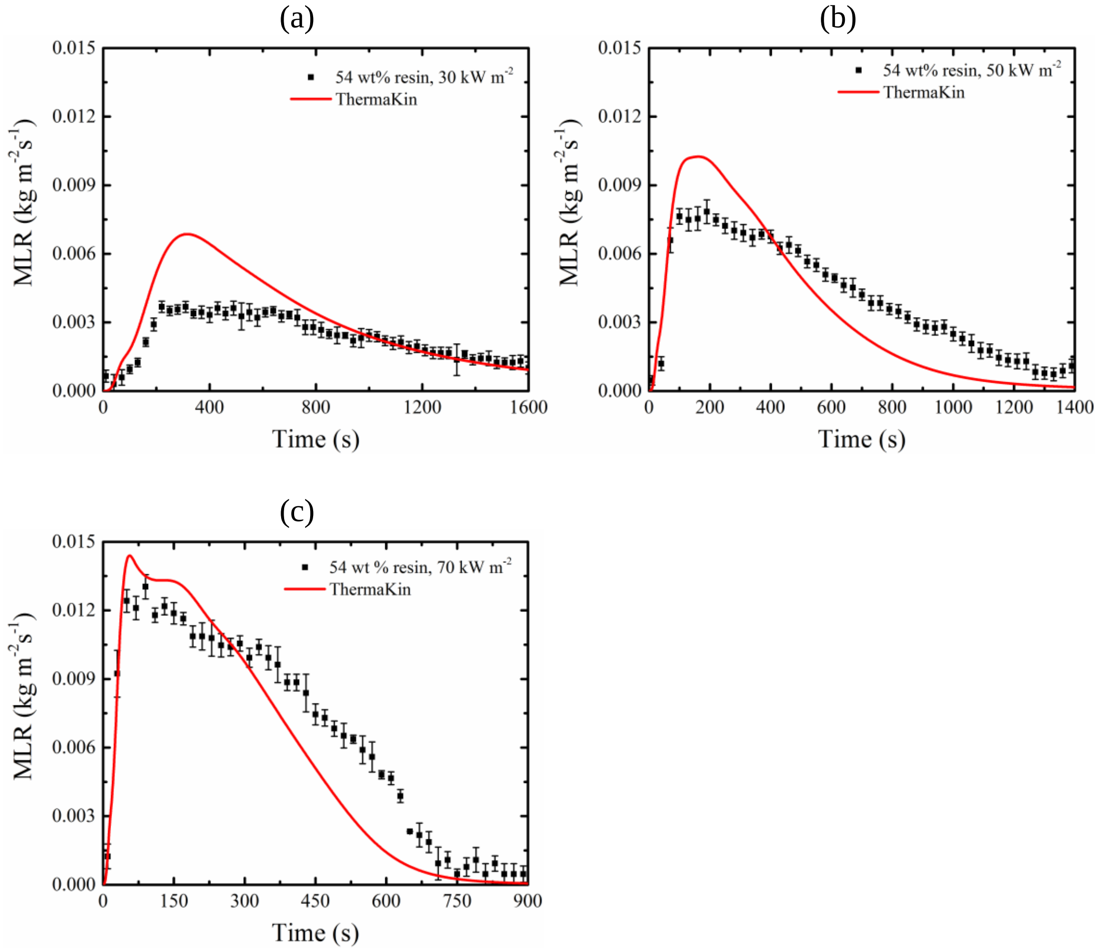

Figure 53. Mass loss rate from experimental data and model simulations for 54 wt% resin composite samples tested at an external heat flux of – (a) 30 kW m^{-2}; (b) 50 kW m^{-2}; (c) 70 kW m^{-2}.

The model was able to reproduce the experimental data very well for external heat fluxes of 50 and 70 kW m^{-2}. The model slightly over-predicted the peak of the experimental curve at 30 kW m^{-2}. The systematic over-prediction was probably a result of the fiberglass reinforcement inhibiting the flow of gases from the condensed phase of the sample. This phenomena has been noted anecdotally in previous works, but there has been little justification for the practical implementation. The effects of gas transport were not observed to influence the mass loss rate significantly at 70 kW m^{-2} because the samples were observed to undergo delamination at this heat flux.

The largest deviation between the predicted and experimental curve occurred at 54 wt% resin. The increased deviation between the model prediction and the experimental measurement for the higher resin content samples was probably due to non-uniform distribution of the resin within the sample. The excess resin was observed to have a slightly higher localized concentration along the bottom surface of the sample; however, the model assumed a homogeneous mixture of the constituents. The difference between the model simulation and the composite samples likely caused the model to over-predict the experimentally measured peak mass loss rate. The growth and decay of the mass loss rate profiles were accurately simulated at the low heat flux. Overall, this model for a fiberglass reinforced polymer composite was able to be expanded to multiple compositions and showed a stark improvement compared to a previous investigation [17].

4. Conclusion

A complete set of material properties was developed for the pyrolysis modeling of fiberglass reinforced polyester composites with the ability to reproduce experimental data at multiple composition ratios and external heat fluxes. The single set of properties was derived from milligram-scale and bench-scale testing coupled with direct and inverse analyses, assumptions regarding material behavior, and values from literature sources. The specific heat capacity, density, and absorption coefficient for the fiberglass reinforcement, as well as the emissivity of all components, were taken from literature values.

Modeling was conducted in a comprehensive pyrolysis model, ThermaKin. The heat transfer was specified in the model to simulate the conditions of the thermal exposure for each experiment. The model was developed through systematic analysis to isolate or partially isolate the material property of interest.

Milligram-scale testing was conducted in a STA on the UP resin, following an oven post-cure at the glass transition temperature. The effective semi-global reaction mechanism was described using three first-order Arrhenius rate reactions, which were characterized through a series of direct calculations and manual iterations of inverse analysis targeting experimental data from TGA. The specific heat capacities for the virgin resin and evolved decomposition species were quantified using DSC measurements coupled with direct analysis of the apparent heat capacity, curve fitting for the temperature range from 313-360 K, and assumptions regarding the behavior of intermediate species. The specific heat capacity of the char was determined through DSC of the isolated component. The heat of decomposition for each degradation reaction was quantified as the difference between the baseline and the sensible energy over the respective temperature range for each reaction.

The broadband spectrum radiative absorption coefficient for the virgin resin was evaluated from experimental testing utilizing the uniform heat flux from the truncated cone calorimeter and the water-cooled Schmidt-Boelter heat flux gauge. The heat flux gauge was used to measure the differential collimated heat flux from the direct exposure to a cone heater and the indirect exposure through a thin sample of resin mounted at the top of the gauge.

Gasification experiments were performed on UP resin samples and composites with composition ratios of 41, 48, and 54 wt% resin in a cone calorimeter equipped with a CAPA and an infrared camera. The CAPA provided a nearly anaerobic environment to prevent the formation of a flame at the sample surface for steady radiant exposures of 30, 50, and 70 kW m^{-2}. The IR camera was mounted to provide optical access to the back of the sample to record the surface temperature, without affecting the precision scale. The mass loss rate and temperature profiles were found to be repeatable for the configurations tested. The back surface temperature data was used as a target for inverse analysis, performed though manual iterations, to characterize the thermal conductivity of the constituents. The thermal conductivity of the UP resin species were determined first through analysis of the UP resin samples. This methodology effectively decoupled the thermal conductivities of the UP resin and fiberglass for analysis. Once the UP resin was parameterized, the 48 wt% resin composite sample was selected, at the low heat flux, as the target to determine the effective thermal conductivity of the fiberglass reinforcement. A linear temperature dependency was assumed for all species except for the second intermediate and the char, which were assumed to follow a third degree polynomial based on the radiation-diffusion approximation.

Validation was provided from the monitored mass loss during the gasification experiments, which was removed from the data analyzed and targeted for model parameterization. The complete set of material properties demonstrated the ability to predict the mass loss rate for UP resin and three composition ratios over a wide range of thermal insults comparable to fire conditions.

Appendix I: Gasification experiments with and without aluminum foil backing

The polymer of interest in this analysis was an unsaturated polyester resin, which was a thermosetting polymer. As the temperature of the polymer increases, the resin will not melt. Tests were performed on the fiberglass samples with and without the aluminum foil to analyze the effect and determine the best configuration for this investigation. The configurations tested include 41 wt% resin at 50 kW m^{-2}, Figure 55, and 30 kW m^{-2}, Figure 54, and 48 wt% resin at 30 kW m^{-2}, Figure 56. The data for the samples without the foil backing are shown in black and the data for the samples with the foil back are shown in blue. The experimental data showed similar results for the mass loss rate, indicating that the mass transfer was not occurring across the bottom surface of the sample and the presence of aluminum foil was not affecting the mass transfer process. However, there were notable deviations between the bottom surface temperature measurements for the samples with and without foil. This would indicate that the addition of the aluminum foil backing resulted in a systematic error. It was decided that testing for the set of configurations would be completed without an aluminum foil backing to reduce the modeling error caused by deviations between the conditions in the laboratory experiment and the physical processes represented in the model.

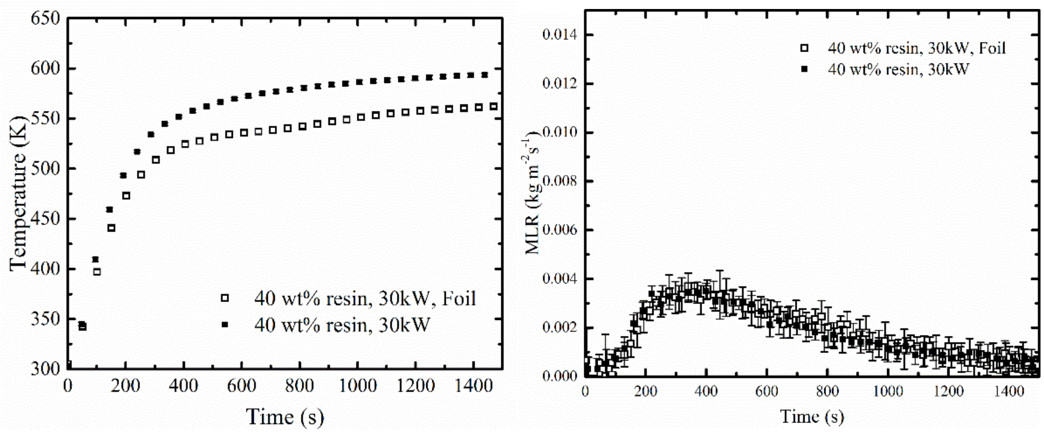

(a) (b)

Figure 54. Back surface temperature and mass loss rate for 41 wt% resin fiberglass samples tested at 30 kW m^{-2} with and without an aluminum foil backing.

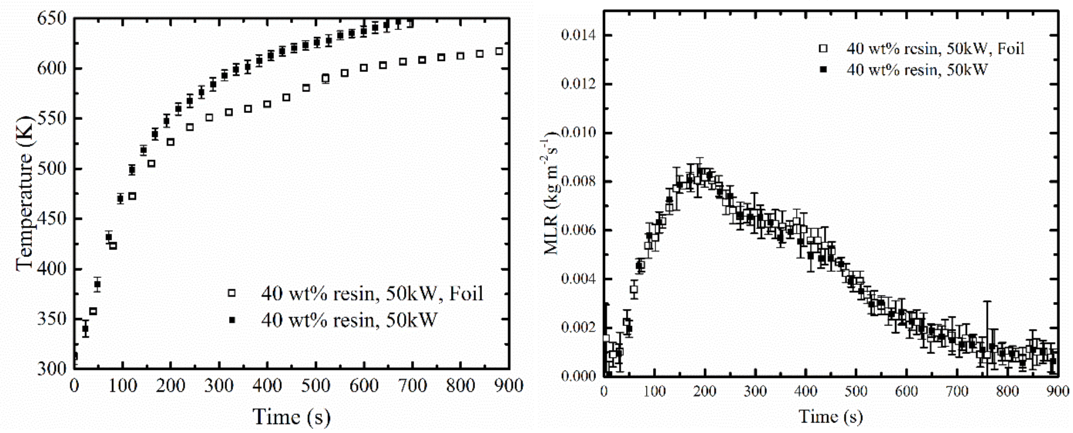

(a) (b)

Figure 55. Back surface temperature and mass loss rate for 41 wt% resin fiberglass sample tested at 50 kW m^{-2} with and without an aluminum foil backing.

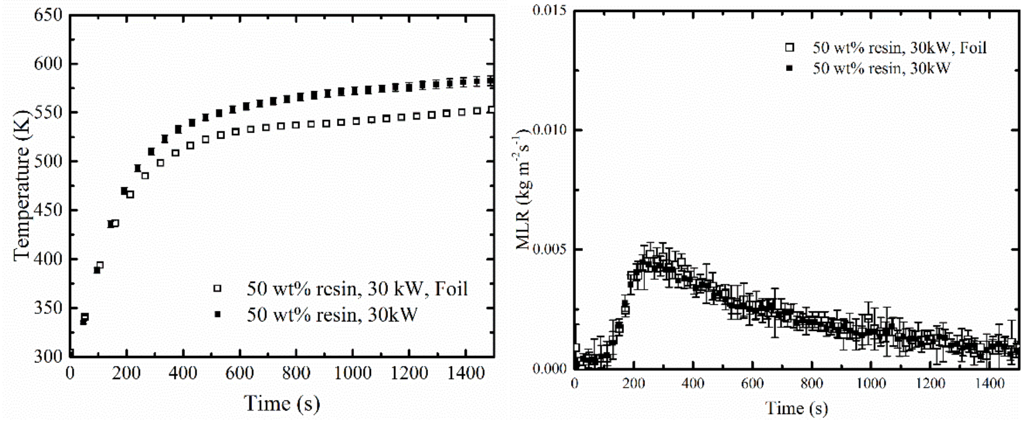

(a) (b)

Figure 56. Back surface temperature and mass loss rate for 48 wt% resin fiberglass samples tested at 30 kW m^{-2} with and without an aluminum foil backing.

Appendix II: Milligram-scale experiments with char samples

In an effort to produce more accurate experimental data, additional TGA/DSC tests were performed on the char. The char samples were harvested from bench-scale tests performed on the resin. This method was selected to provide enough char to produce a sample size within the specified range, and sufficient thermal contact was maintained throughout the test. The disadvantage of this method was that the degradation process may not have been complete and the measurements would have captured the remaining degradation processes.

The normalized mass, measured from TGA, for the milligram-scale experiments on the char are shown in Figure 57.

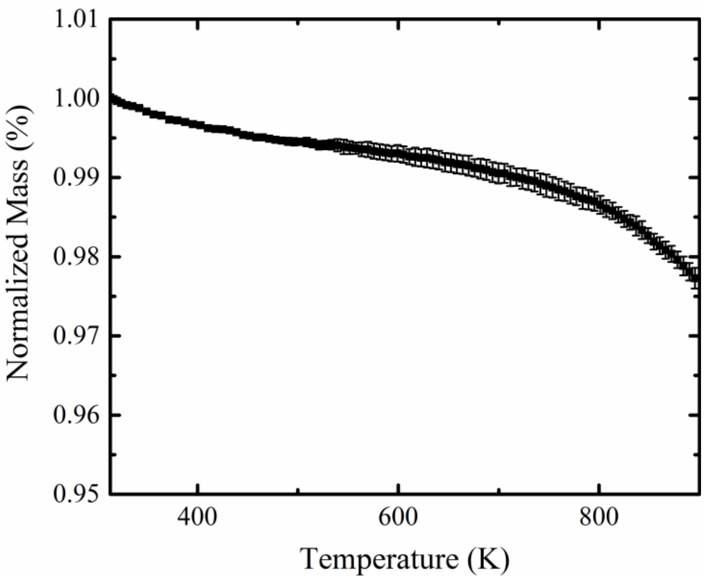

Figure 57. Normalized mass loss during TGA/DSC testing of the char.

The error bars were calculated as two standard deviations of the mean. The small portion of the degradation process observed to occur during this thermal exposure supports the application of the experimental data to model the thermal properties of the char. The heat flow measurement as a function of time is shown in Figure 58.

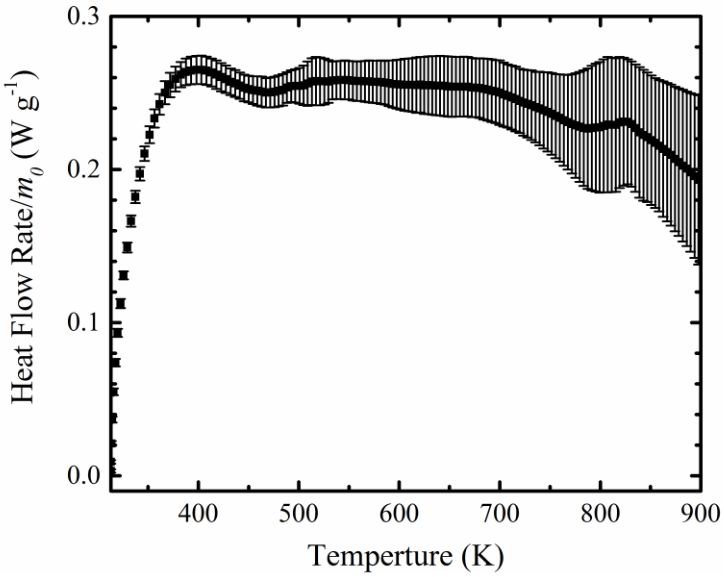

Figure 58. DSC measurement of heat flow to the char.

The decay in the heat flow measurement indicated a loss of measurement accuracy at the elevated temperatures or a loss of thermal contact between the sample and the crucible. Overall, there was more scatter in the char data compared to the experimental results for the polyester resin, with considerable scatter at temperatures above 700 K. The temperature range of 500-700 K was selected as most representative for analysis to determine the specific heat capacity of the char.

The apparent heat capacity of the char, shown in Figure 59, was calculated by dividing the heat flow to the sample by the true heating rate.

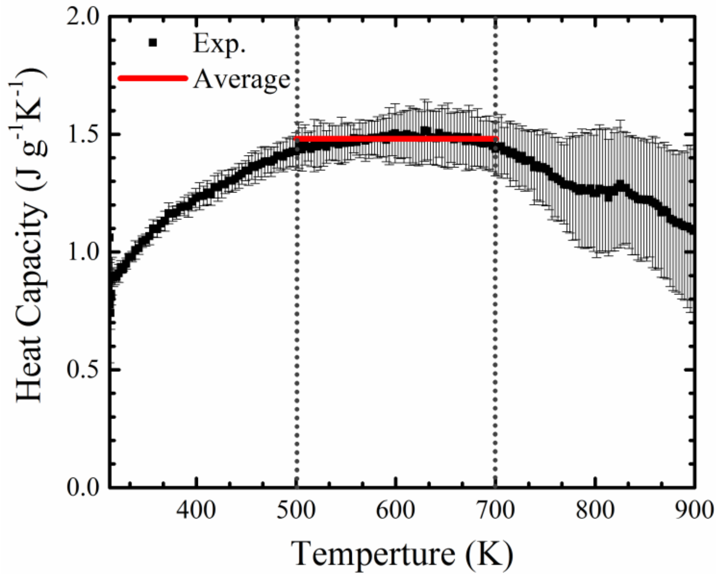

Figure 59. Apparent specific heat capacity of the char as a function of temperature.

The char was assumed to be nonreactive in a non-oxidizing atmosphere, and the specific heat capacity was taken as the average apparent heat capacity over a temperature range from 500-700 K. Based on this methodology, the specific heat capacity of the char was found to be 1470 J kg^{-1}K^{-1}.

Works Cited

[1] S. I. Stoliatrov and R. E. Lyon, *Thermo-Kinetic Model of Burning,* 2008.

[2] C. Lautenberger and C. Fernandez-Pello, "Generalized Pyrolysis Model for Combustible Solids," *Fire Safety Journal,* vol. 44, pp. 819-839, 2009.

[3] A. Y. Snegirev, V. A. Talalov, V. V. Stepanov and J. N. Harris, "A new moel to predict pyrolysis, ignition and burning of flammable materials in fire tests," *Fire Safety Journal,* vol. 59, pp. 132-150, 2013.

[4] K. McGrattan, S. Hostikka, R. McDermott, J. Floyd, C. Weischenk and k. Overholt, *Fire DYnamics Simulator (Version 6) Technical Reference Guide,* 2014.

[5] D. M. Marquis, E. Guillaume, A. Camillo, T. Rogaume and F. Richard, "Exitence and uniqueness of solutions of a differential equation system modeling the thermal decomposition of polymer materials," *Combustion and Flame,* vol. 160, pp. 818-829, 2013.

[6] J. Li, "A Multiscale Approach to Parameterization of Burning Models for Polymeric Materials," College Park, MD, 2014.

[7] M. B. McKinnon, S. I. Stoliarov and A. Wikowski, "Development of a Pyrolysis Model for Corrugated Cardboard," *Combustion and Flame,* vol. 160, pp. 2595-2607, 2013.

[8] J. Li, J. Gong and S. I. Stoliarov, "Gasification Experiments for Pyrolysis Model Parameterization and Validation," *International Journal of Heat and Mass Transfer,* vol. 77, pp. 738-744, 2014.

[9] J. Li and S. I. Stoliarov, "Measurement of Kinetics and Thermodynamics of the THermal Degradation for Non-charring Polymers," *Combustion and Flame,* vol. 160, pp. 1287-1297, 2013.

[10] A. P. Mouritz and A. G. Gibson, Fire Properties of Polymer Composite Materials, Springer, 2006.

[11] A. N. Das and S. K. Baijal, "Degradation Mechanism of Styrene-Polyester Copolymer," *Journal of Applied Polymer Science,* pp. 211-223, 1982.

[12] J. B. Henderson, "A Model for the Thermal Response of Polymer Composite Materials with Experimental Verification," *Journal of Composite Materials,* pp. 579-595, 1985.

[13] J. B. Henderson and M. R. Tant, "A Study of the Kinetics of High-Temperature Carbon-Silica Reactions in an Ablative Polymer Composite," *Polymer Composites,* vol. 4, no. 4, pp. 233-237, 1983.

[14] *ASTM Standard E1354 - 13, Standard Test Method for Heat and Visibile Smoke Release Rate for Materials and Products Using an Oxygen*

Consumption Calorimeter, West Conshohocken, PA: ASTM International, 2013.

[15] B. Y. Lattimer, J. Ouellette and J. Trelles, "Measuring Properties for Material Decomposition Modeling," *Fire and Materials,* vol. 35, pp. 1-17, 2011.

[16] A. Zhou and Z. Yu, "Validating Thermal Response Models Using Bench-Scale and Intermediate-Scale Fire Experiment Data," *Mechanics of Advanced Materials and Structures,* vol. 21, no. 5, pp. 412-421, 2014.

[17] E. Kim, C. Lautenberger and N. Dembsey, "Property Estimation for Pyrolysis Modeling Applied to Polyester FRP Composites with Different Glass Content," in *Fire and Materials*, San Francisco, 2009.

[18] E. Kim, C. Lautenberger and N. Dembsey, "Property Estimation for Pyrolysis Modeling Applied to Polyester FRP Composites with Different Glass Content," in *Fire and Materials*, San Francisco, 2009.

[19] "Fibre Glast Development Corporation," 2010. [Online]. Available: http://cdn.fibreglast.com/downloads/00345-A.pdf. [Accessed 29 March 2015].

[20] "MatWeb Material Property Data," [Online]. Available: http://matweb.com/search/DataSheet.aspx?MatGUID=d9c18047c49147a2a7c0b0bb1743e812&ckck=1. [Accessed 29 March 2015].

[21] S. J. Evans, P. J. Haines and G. A. Skinner, "The effect of structure on the thermal degradation of polyester resin," *Thermochimica Acta*, vol. 278, pp. 77-89, 1996.

[22] R. E. Lyon, N. Safronava, J. Senese and S. I. Stoliarov, "THermokinetic Model of Sample Response in Nonisothermal Analysis," *Thermochimica Acta,* vol. 545, pp. 82-89, 2012.

[23] G. Linteris, M. Zammarano, B. Wilthan and L. Hanssen, "Absorption and Reflection of Infrared Radiation by Polymers in Fire-like Environments," *Fire and Materials,* vol. 36, pp. 537-553, 2012.

[24] J. Li and S. I. Stoliarov, "Measurement of Kinetics and Thermodynamics of the THermal Degradation for Charring Polymers," *Polymer Degradation and Stability,* vol. 106, pp. 2-15, 2014.

[25] M. Semmes, X. Liu, M. B. McKinnon, S. I. Stoliarov and A. Witkowski, "A Model for Oxidative Pyrolysis of Corrugated Cardboard," in *Proceedings of the Eleventh International Symposium on Fire Safety Scienec*, 2014.

[26] S. I. Stoliarov, I. T. Leventon and R. E. Lyon, "Two-dimensional Model of Burning for Pyrolyzable Solids," *Fire and Materials,* vol. 38, pp. 391-408, 2014.

[27] "NIST Chemistry WebBook," The National Institute of Standards and Technology (NIST) Standard Reference Database 69, [Online]. Available: webbook.nist.gov/chemistry/.

[28] S. I. Stoliarov, N. Safronava and R. E. Lyon, "The Effect of Variation of Polymer Properties on the Rate of Burning," *Fire and Materials,* vol. 33, pp. 257-271, 2009.

[29] G. T. Linteris, "Numerical Simulations of Polymer Pyrolysis Rate: Effect of Property Variations," *Fire and Materials,* vol. 35, pp. 463-480, 2010.

[30] P. T. Tsilingiris, "Comparative Evaluation of the Infrared Transmission of Polymer Films," *Energy Conservation and Management,* vol. 44, pp. 2839-2856, 2003.

[31] G. Brauer, "Large area glass coating," *Surface and Coating Technologies,* vol. 112, pp. 358-365, 1999.

[32] T. Matsumoto and A. Ono, "Specific Heat Capacity and Emissisivity Measurements of RIbbon-shaped Graphite using Pulse Current Heating," *International Journal of Thermophysics,* vol. 16, pp. 267-175, 1995.

[33] "Matbase," Matbase, [Online]. Available: www.matbase.com. [Accessed 05 2015].

[34] R. Siegel and J. Howell, Thermal Radiation Heat Transfer, New York: Taylor & Francis, 2002.